



UNIVERSIDAD DE CHILE  
FACULTAD DE CIENCIAS FÍSICAS Y MATEMÁTICAS  
DEPARTAMENTO DE INGENIERÍA MECÁNICA

DESIGN AND ASSESSMENT OF A SOLAR DOMESTIC HOT WATER SYSTEM, FOR  
PAY-AS-YOU-GO BUSINESS MODEL

MEMORIA PARA OPTAR AL TÍTULO DE  
INGENIERO CIVIL MECÁNICO

ALFREDO MORENO ROVETTO

PROFESOR GUÍA:  
JOSÉ MIGUEL CARDEMIL IGLESIAS

MIEMBROS DE LA COMISIÓN:  
WILLIAMS CALDERÓN MUÑOZ  
CRISTIÁN O'RYAN SUAZO

Este trabajo ha sido parcialmente financiado por Endurance Electric SpA.

SANTIAGO DE CHILE  
2020

RESUMEN DE LA MEMORIA PARA OPTAR  
AL TÍTULO DE INGENIERO CIVIL MECÁNICO  
POR: ALFREDO MORENO ROVETTO  
FECHA: 2020  
PROF. GUÍA: JOSÉ MIGUEL CARDEMIL IGLESIAS

DESIGN AND ASSESSMENT OF A SOLAR DOMESTIC HOT WATER SYSTEM, FOR  
PAY-AS-YOU-GO BUSINESS MODEL

Domestic Hot Water (DHW) systems are a nationwide household commodity in Chile, powered mostly by fossil fuels. Approximately 12% of Chile's population does not have a functional DHW system for showering and other purposes installed in their household. A new thermoelectric accumulator powered by a Photovoltaic (PV) system and a Thermoelectric Heat Pump (THP), capable of producing DHW for its users, is being introduced to the national market by Endurance Electric, under a Pay-as-you-Go business model. To reduce uncertainties regarding the device performance and DHW yield, a numerical model is programmed in parallel to the design and construction of a test rig for the device. Experimental results are successfully obtained and utilized to optimize the numerical model using a genetic algorithm procedure and Partial Curve Mapping (PCM) similarity measure to adjust the parameters of the model. Performance measurements for shower comfort, energy and DHW yield are proposed and utilized to validate the numerical model. Once validated, the device is simulated for several locations using Typical Meteorological Year (TMY) data, a specified draw profile and PV system. Correlations between location's yearly average or daily solar radiation and its performance measurements are found for the specified conditions. The device performance is highly affected by ambient temperatures and has better performance at higher ambient temperatures, as well as null DHW yields for low enough ambient temperatures and solar radiation levels. The utilization of the obtained yearly correlations are recommended for an upper and lower limit estimation of the DHW yield of the device and expected shower comfort for the specified simulation conditions. A direct simulation is recommended for obtaining the amount of energy accumulated and for any other DHW draw profile. This Thesis work concludes that the device is capable of producing non-negligible amounts of DHW during the year, reducing the users fossil fuel consumption and enabling the use of this device as auxiliary source of DHW.



RESUMEN DE LA MEMORIA PARA OPTAR  
AL TÍTULO DE INGENIERO CIVIL MECÁNICO  
POR: ALFREDO MORENO ROVETTO  
FECHA: 2020  
PROF. GUÍA: JOSÉ MIGUEL CARDEMIL IGLESIAS

## DISEÑO Y EVALUACIÓN DE SISTEMA DE AGUA CALIENTE SANITARIA SOLAR, PARA MODELO DE NEGOCIOS PAY-AS-YOU-GO

Los sistemas de agua caliente sanitaria (ACS) en Chile son una comodidad de uso común, alimentados principalmente por combustibles fósiles. Aproximadamente el 12% de la población chilena no tiene un sistema de ACS funcional para ducharse, u otros fines, instalados en su hogar. Endurance Electric está introduciendo en el mercado nacional, bajo un modelo de negocios Pay-as-you-Go, un nuevo acumulador termoeléctrico alimentado por un sistema fotovoltaico (PV) y una bomba de calor termoeléctrica (THP), capaz de producir ACS para sus usuarios. Para reducir las incertidumbres sobre el desempeño del dispositivo y la cantidad de ACS que puede generar, se programa un modelo numérico en paralelo al diseño y construcción de un banco de pruebas para el dispositivo. Los resultados experimentales obtenidos se utilizan para optimizar el modelo numérico con la ayuda de un procedimiento de algoritmo genético y una medida de similitud entre curvas, Partial Curve Mapping (PCM), para ajustar los parámetros que definen el modelo. Se proponen medidas de desempeño para la comodidad de una ducha, la energía acumulada y la cantidad de ACS producida, las cuales son utilizadas para validar el modelo numérico. Una vez validado, el dispositivo se simula para varias ubicaciones utilizando datos de un año meteorológico típico (TMY), un perfil de demanda especificado y un sistema PV en particular. Se encuentran correlaciones entre la radiación solar promedio anual o diaria de una ubicación y las medidas de desempeño para las condiciones especificadas. El desempeño del dispositivo se ve muy afectado por la temperatura ambiente y tiene un mejor desempeño a temperaturas ambiente más altas. Por otro lado, entrega cantidades nulas de ACS a temperaturas ambiente y niveles de radiación solar lo suficientemente bajos. Se recomienda la utilización de las correlaciones obtenidas para estimar el límite superior e inferior de la cantidad de ACS a entregar por el dispositivo y la comodidad esperada de las duchas, bajo las condiciones de simulación especificadas. Se recomienda una simulación directa para obtener la cantidad de energía acumulada por el dispositivo y para cualquier otro perfil de extracción de ACS. Este trabajo de tesis concluye que el dispositivo es capaz de producir cantidades no despreciables de ACS durante el año, lo que reduce el consumo de combustible fósil de los usuarios y permite el uso de este dispositivo como fuente auxiliar de ACS.



*A mis padres, por su constante apoyo, soporte y cariño*



# Acknowledgements

During the realization of this Thesis work, I would have had the progress of this investigation constantly staggered if it not were for a lot of people who selflessly helped me into achieving my goals throughout this everlasting process.

I want to thank all of the people that had supported me in the realization of this Thesis work. To all the technical personnel of the mechanical workshop, for their great collaboration in the construction of the test rig structure, their constant hard work, helping hands and great conversations. To all of those who helped me in the installation of the test rig, buying materials, running errands, providing insight and assembling the rig at the rooftop of our faculty. Particularly I want to thank Ian Wolde, who spent lots of time helping me with the design and manufacturing of the test rig, and Eduardo Rodriguez, who provided me periodically with utterly needed solar irradiance data. To all the faculty security personnel, who periodically granted me access to the faculty's rooftop for monitoring, cleaning and extracting data from the test rig. To all the members of the Solar Energy community, for their keen interest in each other's projects, constant support and valuable insight.

I want to thank those who gave the opportunity to investigate in such an interesting matter. To my tutor, José Miguel Cardemil, who constantly bombarded me with questions that I had not even thought about and kept me motivated to work using all the resources I could have never asked for. To my internship boss and tutor, Cristián O'Ryan, who saw great potential in a solution that concerns us all, an idea that could improve many people's life quality, and took the decision to finance this investigation.

Lastly, I want to thank all of my family and friends, for their constant support, advice and care, and all the joy they have brought me during this process. For all the shenanigans we have lived through together. For all the moments of joy and sorrow we have had and shared. For every gesture of affection we had given to one another, I thank you all.





# Contents

<b>1</b>	<b>Introduction</b>	<b>1</b>
1.1	Basic Background . . . . .	1
1.2	Incentive . . . . .	1
1.2.1	Pay-as-you-Go business model . . . . .	2
1.3	Objectives . . . . .	5
1.3.1	Main Objective . . . . .	5
1.3.2	Specific Objectives . . . . .	5
1.4	Scope . . . . .	5
<b>2</b>	<b>Background</b>	<b>6</b>
2.1	Domestic Hot Water . . . . .	6
2.2	Solar Irradiance, Airmass and Angle of Incidence . . . . .	6
2.2.1	Solar Position . . . . .	7
2.2.2	Extraterrestrial Irradiance . . . . .	8
2.2.3	Air Mass . . . . .	8
2.2.4	Plane of Array Irradiance . . . . .	11
2.3	Photovoltaic Array Performance Models . . . . .	13
2.3.1	Sandia’s photovoltaic array performance model ( <b>sapm</b> ) . . . . .	14
2.3.2	NREL’s PVWATTS PV Performance Model . . . . .	20
2.4	Thermoelectric Heat Pump . . . . .	21
2.5	Nexol Water Boiler . . . . .	25
2.6	Similarity Measures . . . . .	26
2.7	Conclusions . . . . .	28
<b>3</b>	<b>Methodology</b>	<b>29</b>
3.1	Data Acquisition . . . . .	29
3.1.1	Experimental Setup . . . . .	29
3.1.2	Meteorological data . . . . .	31
3.1.3	Tests schedule . . . . .	33
3.2	Numerical simulation . . . . .	33
3.2.1	Photovoltaic array electricity generation . . . . .	34
3.2.2	Stratified Tank numerical model . . . . .	34
3.2.3	Model’s accuracy optimization . . . . .	38
3.3	Performance Measurements . . . . .	42
3.3.1	Comfort measurement . . . . .	42
3.3.2	Energy saving measurements . . . . .	42

3.4	Simulation of the validated model in different locations . . . . .	43
3.4.1	Data sources . . . . .	44
3.4.2	Performance Evaluation . . . . .	45
3.4.3	Data analysis . . . . .	46
3.5	Conclusions . . . . .	46
<b>4</b>	<b>Results</b>	<b>48</b>
4.1	Experimental Results . . . . .	48
4.2	Simulated Photovoltaic Array . . . . .	50
4.3	Numerical model improvement and validation . . . . .	52
4.4	Simulated locations . . . . .	58
4.4.1	Maximum Daily Temperature . . . . .	58
4.4.2	Performance Measurements . . . . .	60
4.4.3	Overall assessments . . . . .	70
<b>5</b>	<b>Conclusions</b>	<b>72</b>
	<b>Bibliography</b>	<b>74</b>

# List of Tables

2.1	Empirically determined coefficients used to predict module back surface temperature as a function of irradiance, ambient temperature, and wind speed. . . . .	20
3.1	Coordinates of experimental setup . . . . .	31
3.2	PV module's orientation . . . . .	31
3.3	Test Schedule . . . . .	34
3.4	Constants of exponential approximation for the COP of a THP . . . . .	38
3.5	Upper and lower bound values for attributes to be optimized by GA . . . . .	39
3.6	Genetic Algorithm parameters . . . . .	41
3.7	Upper and lower temperature thresholds for comfort shower temperature range . . . . .	42
3.8	Locations simulated using the validated numerical model and associated geodesic data, ordered from the southernmost to the northernmost considered location. . . . .	45
3.9	Seasonal fixed ambient temperatures considered for an enclosed area, used for the simulations of the device. . . . .	46
3.10	Data input and output of every data-related process of this Thesis work . . . . .	47
4.1	Minimizing parameters for each obtained numerical model candidate for validation . . . . .	52
4.2	Performance values and associated relative error for each candidate, compared to experimentally obtained values. . . . .	53
4.3	Linear Regression parameters for fixed and variable ambient temperature for daily solar radiation vs. maximum daily temperature. . . . .	58
4.4	Scalding Hazard Table. Source: American Burn Association . . . . .	60
4.5	Linear Regression parameters for comfort scatter plots. . . . .	60
4.6	Linear Regression parameters for accumulated energy scatter plot. . . . .	64
4.7	Linear Regression parameters for accumulated DHW yield scatter plot. . . . .	70

# List of Figures

1.1	Nexol's Water Heater simplified schematics . . . . .	2
1.2	Lumos' product and pricing in Nigeria throughout its trial . . . . .	4
1.3	Lumos' sales progression throughout the study . . . . .	4
2.1	Error in zenith angle from ASCE, Spencer, and SOLPOS models relative to SPA for equinoxes and solstices at Albuquerque, NM . . . . .	9
2.2	Extraterrestrial radiation for ACSE, Spencer and SOLPOS model for each day in 2010. . . . .	10
2.3	Graph of AM models at high zenith angles . . . . .	11
2.4	Procedure for obtaining plane-of-array irradiance . . . . .	12
2.5	Scatter plot of over 3300 performance measurements for a 165-Wp mc-Si module. . . . .	13
2.6	Illustration of a module I-V curve showing the five points on the curve that are provided by the Sandia performance model . . . . .	14
2.7	Over 3300 measurements values for $V_{oc}$ and $V_{mp}$ . Recorded and translated to a common temperature of $50^{\circ}C$ , prior to regression analysis. . . . .	16
2.8	Over 3300 measurements values for module current. Recorded and translated to a common temperature of $50^{\circ}C$ , prior to regression analysis . . . . .	16
2.9	Measured solar spectral irradiance on a clear day at different conditions. The normalized spectral response of a typical silicon solar cell is superimposed for comparison. . . . .	17
2.10	Typical empirical relationship illustrating the influence of solar spectral variation on module short-circuit current, relative to the $AM_a = 1.5$ reference condition. . . . .	18
2.11	Typical empirical relationship illustrating the influence of solar angle-of-incidence in reducing a module's short-circuit-current. . . . .	18
2.12	Experimentally determined relationship for back surface temperature as a function of solar irradiance, ambient temperature and wind speed. A linear regression fit provides the coefficients (a, b) . . . . .	19
2.13	Thermoelectric circuit composed of different Seebeck coefficient's semi-conducting materials, configured as a Thermoelectric Heat Pump. Image by Ken Brazier. . . . .	22
2.14	Coefficient of performance of a thermoelectric heat pump given a temperature difference, with it's hot side fixed at $300K$ . . . . .	22
2.15	Schematic diagram of AS-THP . . . . .	23
2.16	Building annual energy balance as conventional PV system and TEG integrated system. . . . .	23
2.17	Schematic of the integrated thermoelectric systems . . . . .	24

2.18	Nexol’s preview of it’s water heater internal function. Source: Nexol-AG . . .	25
2.19	Hysteresis curve from experimental and numerically simulated data. . . . .	26
2.20	Plot of the objective value as a function of the iteration of the Genetic Algorithm for clean experimental curves . . . . .	27
2.21	Plot of the objective value as a function of the iteration of the Genetic Algorithm for noise-added experimental curves. . . . .	27
3.1	Diagram of the test rig, showing energy and water supply, as well as sensors for data acquisition . . . . .	30
3.2	PV module installed at a 30 degree tilt, in a setup equivalent to an insulated rack mount . . . . .	30
3.3	Sensorized test rig . . . . .	30
3.4	DataLogger(above), programmable electric actuator (middle) and UPS (below). Installed inside a safe box . . . . .	32
3.5	Irradiance data acquired for a mostly sunny day . . . . .	33
3.6	Irradiance data acquired for a mostly cloudy day . . . . .	33
3.7	Simplified representation of TRNSYS Type 154 numerical model for thermal storage tank . . . . .	35
3.8	Simplified representation of adapted simulation model, with forced mixing between nodes . . . . .	35
3.9	Flow diagram for the computation of each time-step . . . . .	37
3.10	The PCM method construct trapezoids between two curves for every possible offset . . . . .	40
3.11	Evolution of comfort metric during a 5 minute shower . . . . .	43
3.12	Evolution of energy gain metric during a 5 minute shower . . . . .	44
4.1	Hot and cold 5 minute water draw for a sunny day, at 18:00 . . . . .	48
4.2	Hot and cold 5 minute water draw for a cloudy day, at 18:00 . . . . .	48
4.3	Hot water draw profiles from September 14 <sup>th</sup> , 2019 to October 21 <sup>st</sup> , 2019 . . . . .	49
4.4	Plane of Array irradiance values for a sunny day. . . . .	50
4.5	Temperatures of the PV module and it’s cells during a sunny day. . . . .	51
4.6	Simulated power generation for a 150W nominal power PV array, tilt and orientation as in Table 3.2 . . . . .	51
4.7	Simulated and experimental temperature profiles for a specific time frame and set of data points. . . . .	52
4.8	Simulated and experimental temperature profiles of a GA improved numerical model . . . . .	53
4.9	Evolution of the PCM value individuals for each generation. . . . .	54
4.10	Experimental and simulated temperature profiles. Simulation performed using first iteration of improved numerical model . . . . .	54
4.11	Experimental and simulated temperature profiles. Simulation performed using first iteration of improved numerical model (1/5) . . . . .	55
4.12	Experimental and simulated temperature profiles. Simulation performed using first iteration of improved numerical model (2/5) . . . . .	55
4.13	Experimental and simulated temperature profiles. Simulation performed using first iteration of improved numerical model (3/5) . . . . .	56

4.14	Experimental and simulated temperature profiles. Simulation performed using first iteration of improved numerical model (4/5)	56
4.15	Experimental and simulated temperature profiles. Simulation performed using first iteration of improved numerical model (5/5)	57
4.16	Maximum daily temperature reached inside the thermal storage tank, among all the locations, for variable and fixed ambient temperature simulations	58
4.17	Scatter plot of yearly average daily solar radiation and maximum daily temperature reached inside the thermal storage tank, among all the locations, for variable and fixed ambient temperature simulations	59
4.18	Density plot for comfort measurements considering variable ambient temperature throughout the year.	61
4.19	Density plot for comfort measurements considering fixed ambient temperatures (A) throughout the year.	61
4.20	Density plot for comfort measurements considering fixed ambient temperatures (B) throughout the year.	62
4.21	Density plot for comfort measurements considering fixed ambient temperatures (C) throughout the year.	62
4.22	Scatter plots for yearly average daily solar radiation and average comfort, with linear regression curves.	63
4.23	Density plot for energy measurements considering variable ambient temperatures throughout the year.	64
4.24	Density plot for energy measurements considering fixed ambient temperatures (A) throughout the year.	65
4.25	Density plot for energy measurements considering fixed ambient temperatures (B) throughout the year.	65
4.26	Density plot for energy measurements considering fixed ambient temperatures (C) throughout the year.	66
4.27	Scatter plots for yearly average daily solar radiation and accumulated energy, with linear regression curves.	66
4.28	Density plot for DHW yield measurements considering variable ambient temperatures throughout the year.	67
4.29	Density plot for DHW yield measurements considering fixed ambient temperatures (A) throughout the year.	68
4.30	Density plot for DHW yield measurements considering fixed ambient temperatures (B) throughout the year.	68
4.31	Density plot for DHW yield measurements considering fixed ambient temperatures (C) throughout the year.	69
4.32	Scatter plots for yearly average daily solar radiation and accumulated DHW yield, with linear regression curves.	69

# Chapter 1

## Introduction

### 1.1 Basic Background

Domestic hot water (DHW) systems are a must when it comes to commodities in households nowadays. From antique wood stoves to modern evacuated tube solar collectors, DHW generation, storage and usage has been a subject of study throughout the history of mankind. Nonetheless this commodity, as valued as it is, can be an environmental and economical concern due to the fact that most of DHW systems in Chile are powered by fossil fuels or electricity. Further studies have shown that 11.6% of households in Chile do not have access to DHW [1]. In addition to this, the population without a standardized DHW system are coping with this situation by using inefficient heating methods such as fire pits or makeshift stoves, among others, exposing themselves to burns, carbon monoxide inhalation and other misdemeanors.

Limited access to energy services, low quality of the service provided or inequity in the expenses regarding household energy consumption is addressed as Energy Poverty (EP). For example, population with lowest income may have less monthly expenses, but have a higher percentage of monthly expenses in energy services than higher income population, hence the inequity of energy services [2].

### 1.2 Incentive

An innovative solution for DHW generation has been designed and prototyped by Nexol-AG, as an alternative to Gas Boilers. A solar powered water heater, shown in Figure 1.1. Using a thermoelectric heat pump (THP), this device is able to transfer heat from ambient air into an insulated water tank due to an electrically induced temperature gradient between two metal plates. Given that the THP works with direct current, the device can be powered directly by a photovoltaic (PV) panel installed near the device. This device, coupled with the use of an internet-linked controller, can enable a company to sell a DHW service using a



Pay-as-you-Go business model.

Endurance Electric, a company whose aim is to provide solar solutions to people affected by EP, has endowed the needed capital for the present investigation to assess the usage of Nexol's prototype coupled with their Pay-as-you-Go business model. It is in their interest to reduce uncertainties regarding the prototype's hot water yield given a location's meteorological conditions and its users' hot water demand.

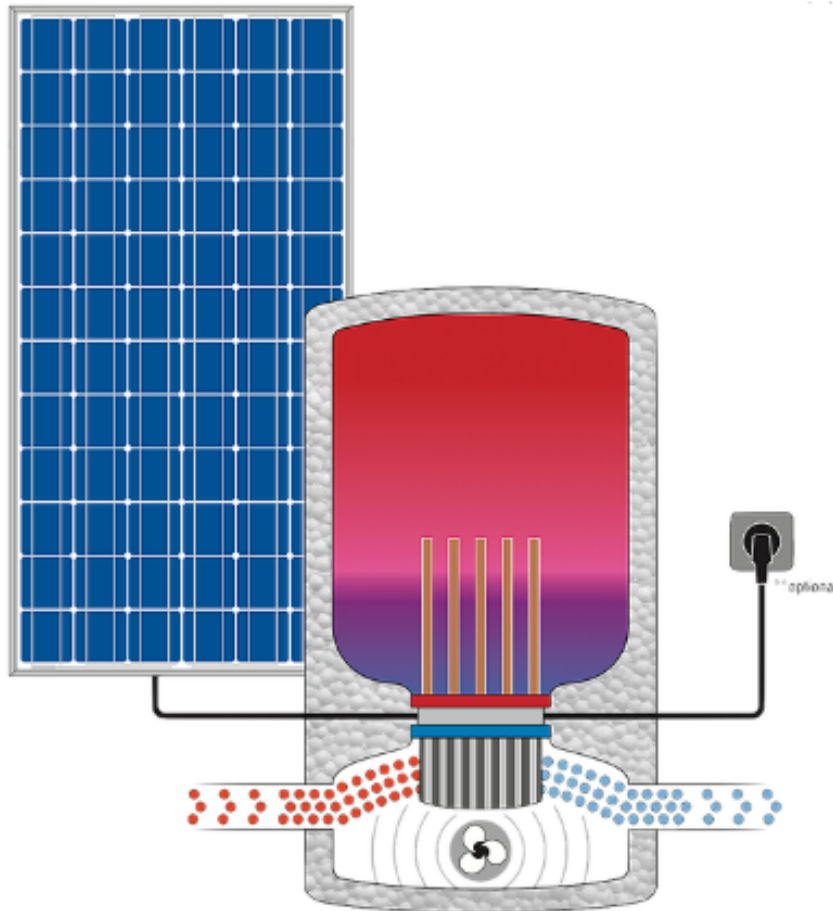


Figure 1.1: Nexol's Water Heater simplified schematics

### 1.2.1 Pay-as-you-Go business model

A Pay-as-you-Go (PAYG) business model is one in which you pay for a service before you use it and cannot use it more than you have paid for. The most common application of this model is in the telecommunication companies, where a client pays in advance for "credits" that enable to use the company's services. Once the credits are expended, the client can no longer make use of the device until it replenishes said credits. An important aspect of this expendable credits is that they can expire and no longer be of use if the period of time they would be available has ended.

In solar applications, there are a non negligible number of companies throughout the

world that are offering PAYG solar systems for Off-grid residential and small businesses applications. These companies have proven the ability scale and replicate their model across East Africa.

### **Case Study: Lumos [3]**

Nigeria, with 96 million people living without access to electricity, is Africa's largest off-grid market[4]. Despite the attractiveness of the market, the entry of private players has been held back by a negative reputation around security challenges and general questions on the ease of doing business.

The key objectives of this study were to trial a prepaid utility service that uses PAYG solar in West African markets with limited access mobile money penetration. This study was possible due to collaboration between Lumos and MTN. This last company is a mobile telecommunications company present in the area that, through partnership with Lumos, was able to provide Mobile Electricity service while contractually making costumers enter into a 5-year lease agreement with Lumos . Through this pilot, Lumos generated insights into the Nigerian market and valuable learning in developing strong partnerships with mobile operators.

Throughout the trial, Lumos and MTN provided customers with an energy utility service at prices shown in Figure 1.2. This figure shows customers first pay a commitment fee to subscribe the service and receive the Solar Home System (SHS) unit, having the choice to purchase 3, 7 or 30 days' worth of service at a time. This payment structure is designed to incentivise customers into purchasing larger bundles. Once the 5-year lease has ended, the SHS is permanently unlocked and the customer owns the system.

Using this methodology, Lumos was able to begin their sales of SHS in June 2014, as part of a pre-commercial pilot, until early 2015 when billing integration with MTN begun and the pilot launched in the mobile company stores. As shown in Figure 1.3, Lumos launched a commercial in multiple MTN stores throughout Nigeria reaching monthly sales growth of over 100%.

As a first mover in the PAYG sector in Nigeria, Lumos' experience highlights the opportunity that exists in the market and the ways that business models can be adapted to the local context, making this an important insight for any company that is interested in the PAYG sector.

## Lumos' product and pricing in Nigeria<sup>17</sup>

System Components	Commitment Fee	3-day Usage Fee	7-day Usage Fee	30-day Usage Fee
80W panel 2 LED Lights 1 Phone Charger 2 Cigarette ports, 4 DC jack ports, 2 USB ports	NGN 15,000 (USD 75)	NGN 400 (USD 2)	NGN 850 (USD 4.25)	NGN 3300 (USD 16.5)

17. Prices converted based on a rate of 0.005 NGN/USD based on the average rate between early 2015 and mid 2016.

Figure 1.2: Lumos' product and pricing in Nigeria throughout its trial

## Sales Progression by Month

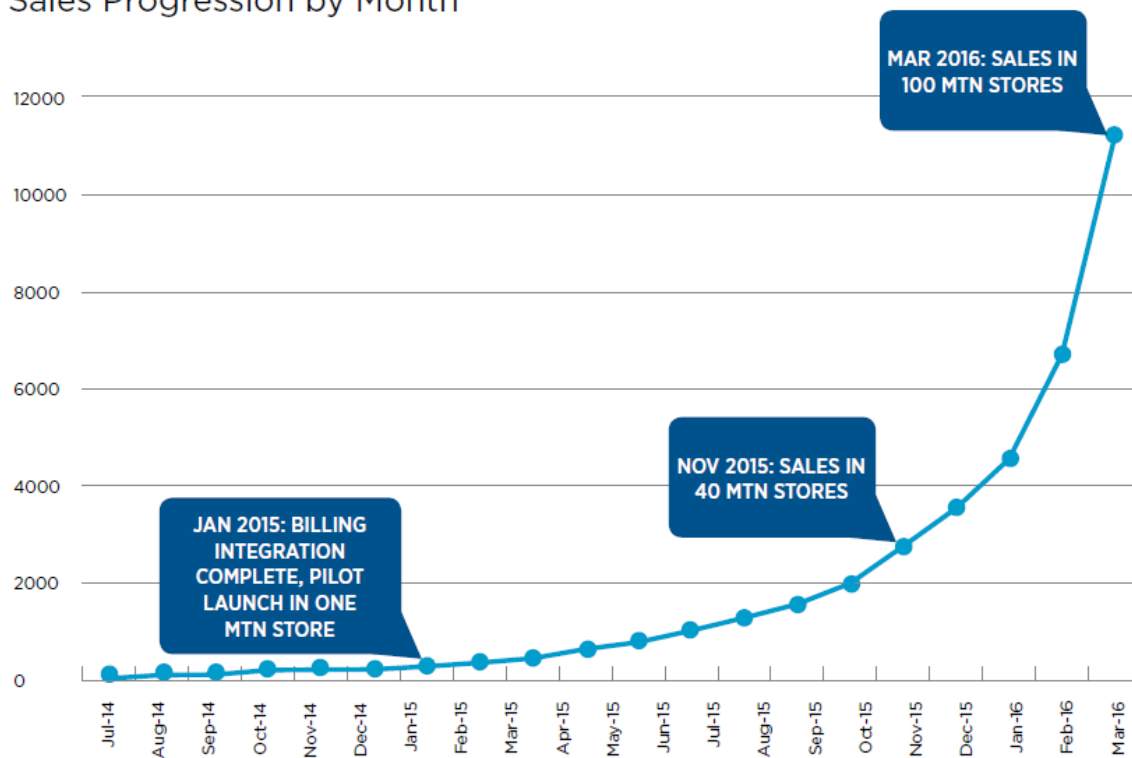


Figure 1.3: Lumos' sales progression throughout the study

## 1.3 Objectives

### 1.3.1 Main Objective

The main objective of this Thesis work is to determine the yield of a Solar Domestic Hot Water Generator and assess the potential benefits for it's use.

### 1.3.2 Specific Objectives

In order to accomplish the main objective the following specific objectives must be taken care of:

- Verify possible correlations between the studied prototype's yield and local meteorological data.
- Determine prototype's yield given a location and hot water draw profile.
- Confirm studied prototype's potential energy savings.
- Assess prototype's usage safeness.

## 1.4 Scope

The present engineering Thesis will be focused on:

- Design and construction of a test rig.
- Experimental setup for data collection.
- Simulation of photovoltaic energy generation given meteorological data.
- Simplified simulation of prototype's yield.
- Numerical model improvement using genetic algorithm.
- Validation of numerical model using experimental data.
- Yearly simulations under pre-defined conditions.
- Overall assessment of prototype's behaviour under Pay-as-you-Go conditions
- CFD simulation is up to discussion due to time constraints of the Thesis.

# Chapter 2

## Background

### 2.1 Domestic Hot Water

Defined as water used, in any type of building, for domestic purposes, principally drinking, food preparation, sanitation and personal hygiene. Domestic Hot Water (DHW) is a important commodity every household aims to have. This resource is mainly produced, in Chile, by gas boilers and other systems such as thermoelectrical water storage systems that raise the water temperature to a comfortable temperate for shower usage. Is not uncommon that reached water temperatures are over the user's comfort and have to be lowered mixing it directly with tap water in order to be used as such. On the other hand, thermal storage based domestic hot water systems have to heat DHW over a minimum of  $60\text{ }^{\circ}\text{C}$  to prevent *legionella* growth [5] and legionellosis infections. Having this scalding temperatures present in the system, thermostatic mixer valves have to be installed near the outlets of the hot water system to prevent injuries.

### 2.2 Solar Irradiance, Airmass and Angle of Incidence

The terrestrial solar irradiance on a clear day has been highly studied and is a function of the solar elevation angle, site altitude, aerosol concentration, water vapor, and various other atmospheric conditions [6, 7]. As irradiance is a measure of the power of sunlight ( $\text{W}/\text{m}^2$ ), this information can be used to model the general maximum output of a solar photovoltaic system for any given day and location.

Even on a clear day, all the extraterrestrial irradiance (Section 2.2.2) does not reach the ground. Generally at noon on a clear day, about 25% of the extraterrestrial radiation from the sun is scattered and absorbed as it passes through the atmosphere. In the morning and the evening, the attenuation from the atmosphere increases due to the longer path through the atmosphere (Section 2.2.3) The radiation coming directly from the sun is called direct irradiance or beam irradiance. The measure of this direct normal irradiance (DNI) is the

flux of the beam radiation through a plane perpendicular to the direction of the sun. The sunlight that is scattered in the atmosphere is scattered in all directions, so part of this radiation is redirected towards earth and is called diffuse irradiance. This is why the sky is light during the day, and why there is still light in the shade. During overcast days, the solar power comes almost completely from the diffuse irradiation. Diffuse irradiance also includes reflections from the ground, which depends on the surface albedo, and which can increase significantly when there is snow. The total solar radiation on a horizontal surface is called global horizontal irradiance (GHI). GHI is the sum of the diffuse radiation incident on a horizontal surface plus the direct normal irradiance projected onto the horizontal surface (i.e.,  $GHI = \text{Diffuse} + DNI \times \cos(z)$ , where  $z$  is the solar zenith angle). GHI is typically measured with a pyranometer. Diffuse irradiance can be measured with a pyranometer that is shaded from the beam irradiance. DNI is typically measured with a pyrhelimeter or inferred from the difference between GHI and measured diffuse.

## 2.2.1 Solar Position

The intensity of the sun is highly dependent on the position of the sun in the sky relative to the observer on the Earth's surface. At higher zenith angles, the light goes through more atmosphere than when the sun is directly overhead. Thus all clear sky models require geometric inputs describing the solar zenith angle throughout the year.

At solar noon (i.e when the sun crosses the meridian) on either the spring or fall equinox, the zenith angle ( $z$ ) is equal to the latitude of the site ( $\phi$ ):

$$z = \phi. \quad (2.1)$$

During any other Day Of the Year (DOY), the zenith angle at a solar noon is calculated by subtracting the declination angle ( $\delta$ ) to the latitude of the site ( $\phi$ ):

$$z = \phi - \delta. \quad (2.2)$$

There is more than one representation for the declination angle ( $\delta$ )[8, 9]. Most commonly shown in the simple representation given in ASCE [8]:

$$\text{where } \delta = 23.45 \times \sin(x) \quad (2.3)$$

$$\text{with } x = \frac{360^\circ}{365}(\text{DOY} - 81) \quad (2.4)$$

To account for times other than solar noon, solar time is calculated based on the difference between a site's longitude and the meridian of it's time zone, and the yearly perturbations on the earth's rotation around the sun [8]:

$$\text{SolarTime} = \text{LocalTime} + (\text{Standard Meridian} - \text{Local Meridian}) \times 4' + EoT \quad (2.5)$$

where  $EoT[\text{min}] = 9.87 \sin(2x) - 7.53 \cos(x) - 1.5 \sin(x)$  and  $x$  is given in Equation (2.4)

The hour angle ( $\omega$ ) is the angle between the line pointing directly to the sun and the line pointing directly to the sun at solar noon. Note that the hour angle is just an angular representation of time, and fifteen degrees represent one hour:

$$\omega[^{\circ}] = (\text{SolarTime[h]} - 12) \times 15 \quad (2.6)$$

Then, the true zenith angle for any date, time and location can be calculated using the declination angle, solar time and site latitude:

$$\cos(z) = \cos \phi \cos \delta \cos \omega + \sin \phi \sin \delta \quad (2.7)$$

More complex solar position equations also account for variations in earth's orbit, as well as other physical influences on the apparent solar position (e.g., refraction). The National Renewable Energy Laboratory (NREL) has made available several algorithms for the solar position in recent years. In 2000, NREL developed SOLPOS 2.0, providing references, C code, and an online user interface [10, 11]. The most recent Solar Position Algorithm (SPA) developed by NREL in 2004 calculates the solar position with very low uncertainty based on location, date, and time inputs for the years -2000–6000[12]. This algorithm has been shown to be highly accurate with uncertainties of +/- 0.0003 degrees[13]

Figure 2.1 shows a comparison of these different methods for calculating the zenith angle of for a given location throughout the year. Each model is compared to the NREL's SPA as it has been shown to be the most accurate. Note that the maximum error is generally within 0.2% from SPA.

## 2.2.2 Extraterrestrial Irradiance

The extraterrestrial radiation, or the radiation that reaches the outer part of earth's atmosphere, varies slightly throughout the year. To account for the eccentricity of the Earth's orbit around the sun, the extraterrestrial radiation is calculated with a yearly varying term [8]:

$$I_0 = 1367.7 \times \left\{ 1 + 0.033 \times \cos \left( \frac{2\pi}{365} \times \text{DOY} \right) \right\}. \quad (2.8)$$

There are also more detailed models created by Spencer through Fourier series [9] and NREL's SOLPOS algorithm [10]. All these models are plotted in Figure 2.2. The three models vary slightly from each other, but have the same general shape for calculating extraterrestrial solar radiation.

## 2.2.3 Air Mass

Air mass refers to the optical path length through the atmosphere where light is scattered and absorbed. This is why objects in the horizon, with larger zenith angles appear less bright

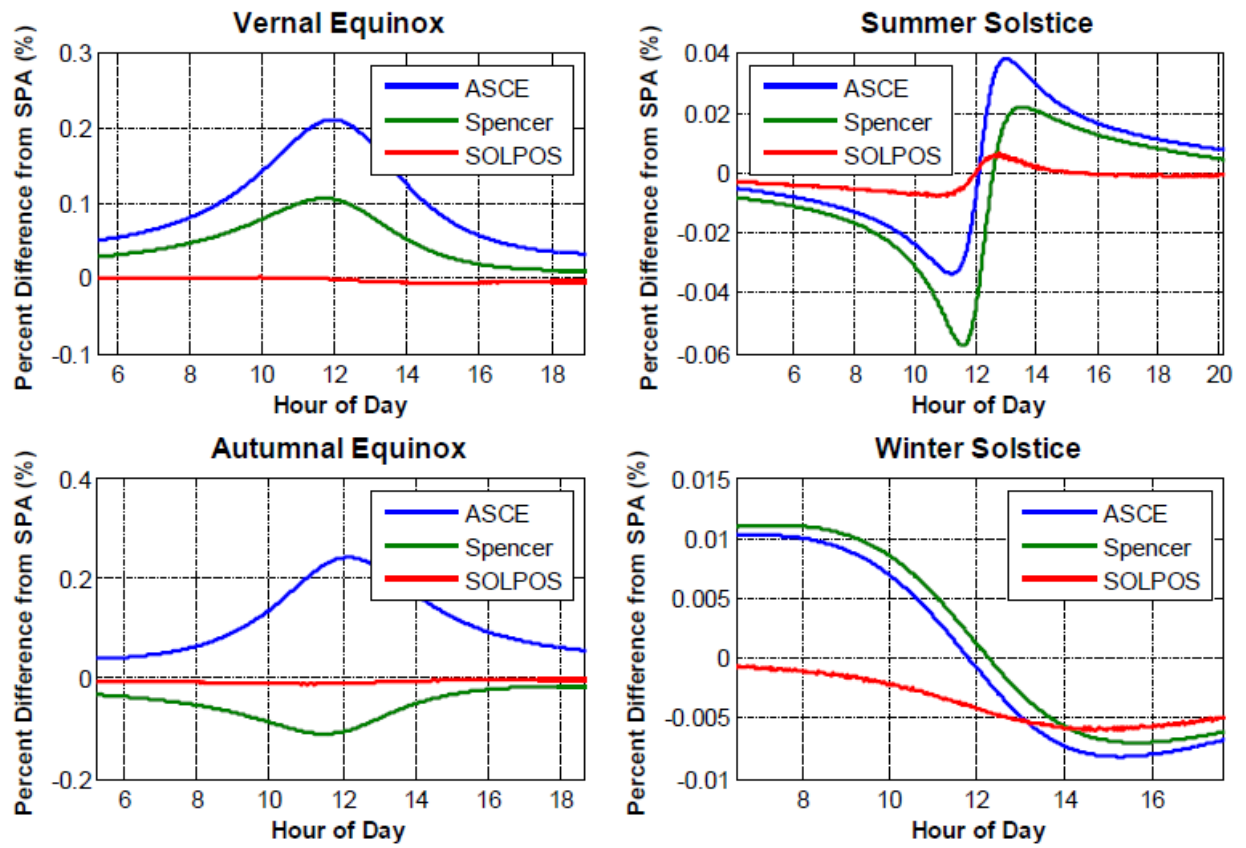


Figure 2.1: Error in zenith angle from ASCE, Spencer, and SOLPOS models relative to SPA for equinoxes and solstices at Albuquerque, NM



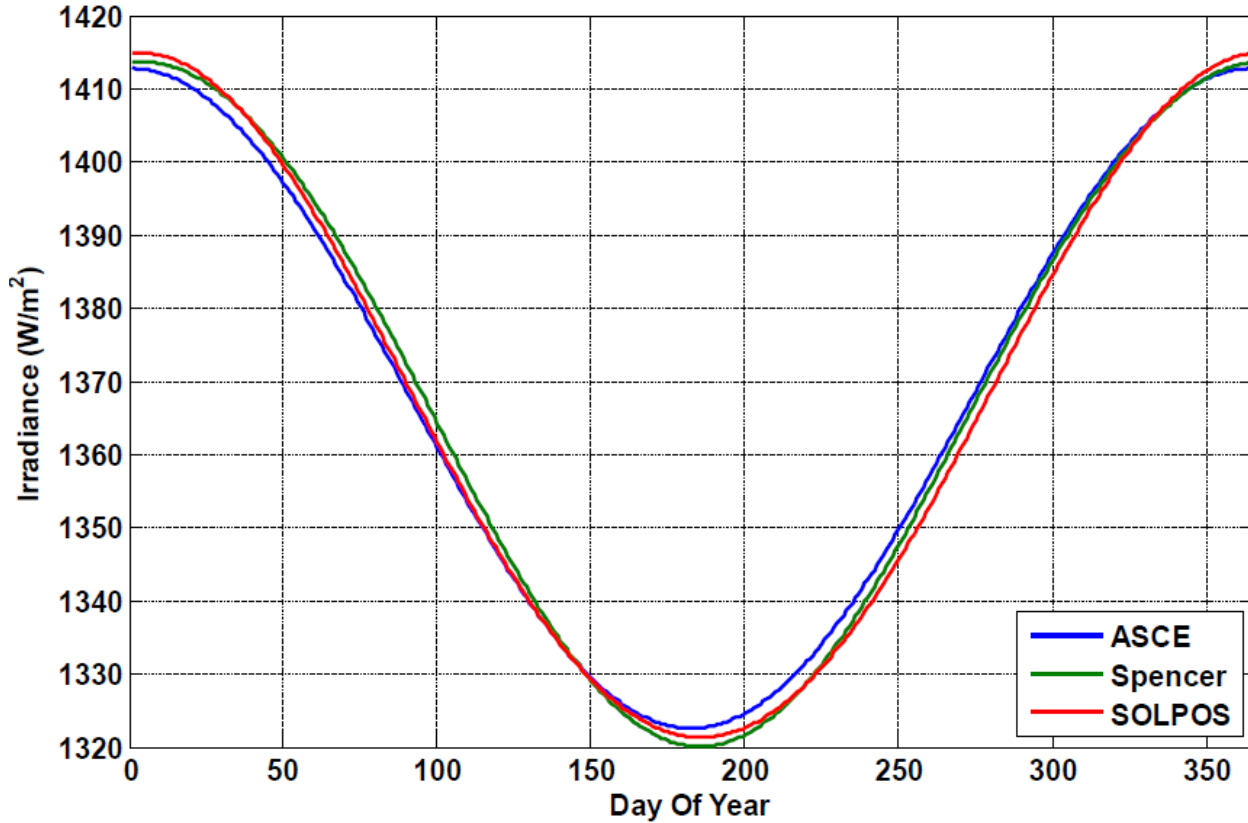


Figure 2.2: Extraterrestrial radiation for ACSE, Spencer and SOLPOS model for each day in 2010.

than when they are directly overhead. In solar energy, air mass actually refers to relative air mass that is measured relative to the path length at the zenith. When the sun is directly overhead, air mass has a value of one,  $AM=1$ . Irradiance at  $AM=0$  is the extraterrestrial irradiance (without any atmosphere). Irradiance at  $AM=2$  occurs when the solar energy is traveling a distance twice as much atmosphere, with zenith angle approximately equal to  $60^\circ$ . Atmospheric attenuation of solar radiation is not the same for all wavelengths, so the solar spectrum also changes with air mass, as further explained in section 2.3.1.

There are several numerical models for calculating the solar airmass, taking into account the solar zenith angle ( $z$ ). The most simple one ignores the Earth's curvature and considers a constant atmospheric density

$$AM = \frac{1}{\cos(z)} \quad (2.9)$$

As shown in Figure 2.3, this simple approach is adequate for zenith angles as large as  $80^\circ$ , but at larger angles and especially near the horizon, the accuracy degrades rapidly because airmass goes to infinity at  $90^\circ$ . The other models shown in Figure 2.3 have been developed to fit measured data as a function of zenith angle.

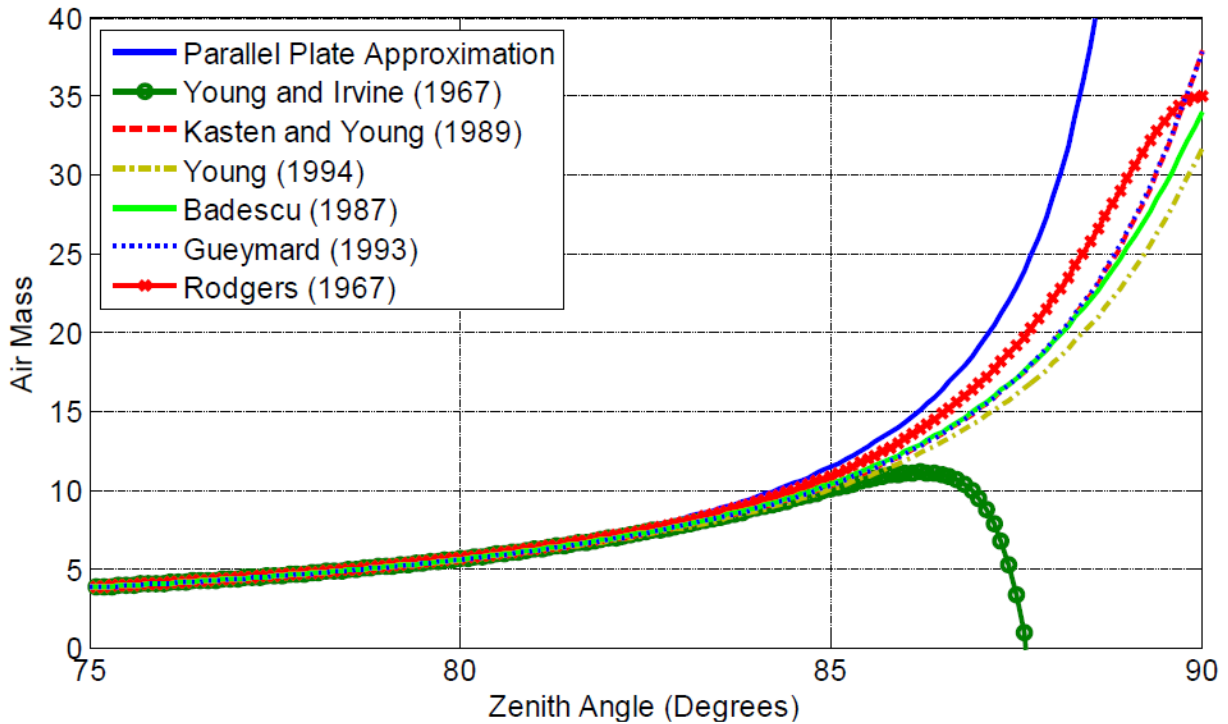


Figure 2.3: Graph of AM models at high zenith angles

## 2.2.4 Plane of Array Irradiance

The plane-of-array irradiance is the solar irradiance that a Photovoltaic Array, with a certain orientation and location is receiving. To determine this value, the array's location, tilt and orientation is needed. Also, solar irradiation data such as global horizontal irradiance, diffuse irradiance and direct normal irradiance.

The solar angle of incidence as well as the air mass needs to be calculated, using the models described beforehand. Also, a value for the extraterrestrial irradiance has to be calculated. With this values, as well as diffuse horizontal irradiance and direct normal irradiance data, the diffuse irradiance component that the array is receiving can be calculated using the Perez model [14].

The ground reflected component for diffuse irradiation depends on the global horizontal irradiance and the surrounding surface's albedo, which is the proportion of solar irradiance that is reflected by a surface and scattered into the atmosphere [15]. The ground diffuse irradiance is added to the diffuse irradiation component that incides a photovoltaic array.

As is represented in Figure 2.4, the calculation of the plane-of-array irradiance can be made for any time of the day if there's data available. Therefore, the instant power that a photovoltaic array is delivering can be obtained, using the performance models described in Section 2.3

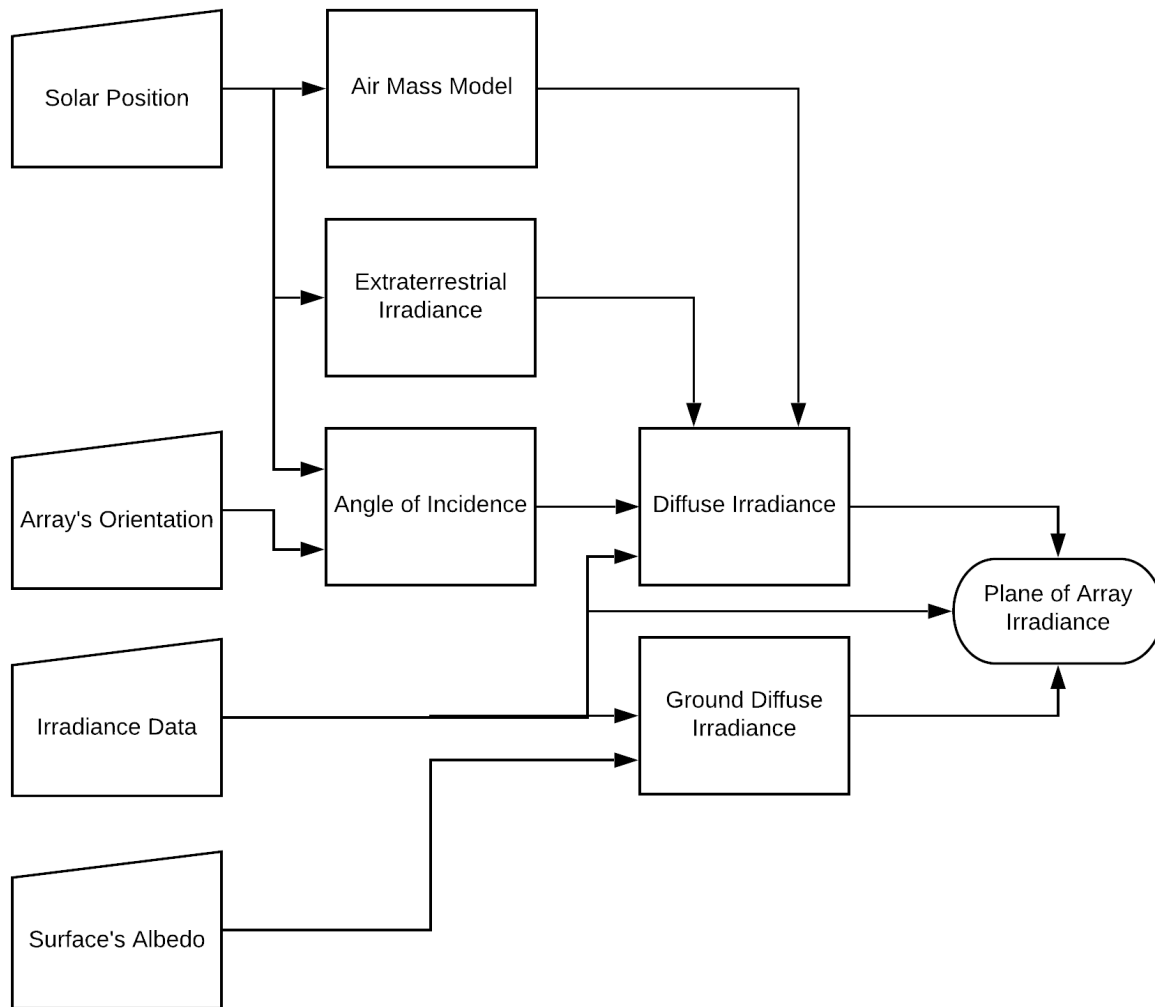


Figure 2.4: Procedure for obtaining plane-of-array irradiance

## 2.3 Photovoltaic Array Performance Models

To predict a Photovoltaic (PV) array’s performance, a numerical model, able to separate and quantify the influence of all significant factors that affect its performance, is required. The wasp-shaped scatter plot in Figure 2.5 illustrates the complexity of the modeling challenge, using data recorded during both clear sky and cloudy/overcast conditions. The vertical spread in  $P_{mp}$  values is primarily caused by variations in the solar irradiance levels and the horizontal spread in  $V_{mp}$  values is primarily related to module temperature.

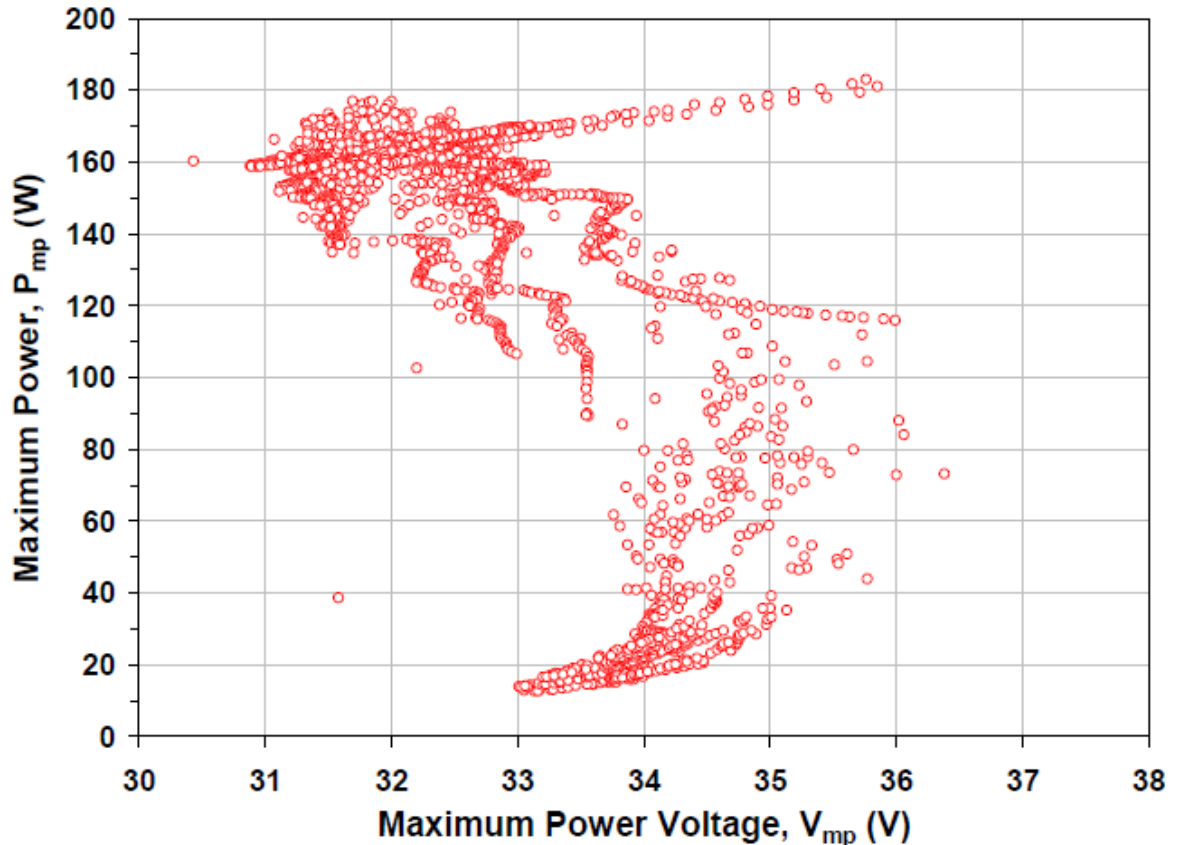


Figure 2.5: Scatter plot of over 3300 performance measurements for a 165-Wp mc-Si module.

There are standard reporting conditions that the industry used to “rate” or “specify” the performance of a PV module. This rating is provided at a single standardized (reference) operating condition [16, 17]. To rate the performance of PV modules the standardized conditions are:

$T_o$ : Reference cell temperature for rating performance, typically  $25^\circ C$

$E_o$ : Reference irradiance, typically  $1000 W/m^2$

$I_{sco} = I_{sc}(E = E_o, AM_a = 1.5, T_c = T_o, AOI = 0^\circ)$ . Short-circuit current at standardized conditions.

The following performance models have been implemented in an unified **Python** library known as `pvl` [18], which has been used extensively in this Engineering Thesis.

### 2.3.1 Sandia's photovoltaic array performance model (sapm)

This model is defined by 10 different equations that are used for calculating the expected power and energy produced by a module. Assuming that predetermined module performance coefficients information is available, a curve which represents a photovoltaic module performance can be plotted. As seen in Figure 2.6 there are three points normally found in a PV module's data sheet.

$I_{sc}$ : Short-circuit current (A)

$I_{mp}$ : Current at maximum-power point (A)

$V_{mp}$ : Voltage at maximum-power point (V)

$V_{oc}$ : Open-circuit Voltage (V)

Additionally, there are two points determined by the model that better define the shape of a module's I-V curve.

$I_x$ : Current at module  $V = 0.5V_{oc}$  (A)

$I_{xx}$ : Current at module  $V = 0.5(V_{oc} + V_{mp})$  (A)

This model generates an I-V curve for the actual solar irradiance and weather conditions and determines the **maximum power output** of the PV module.

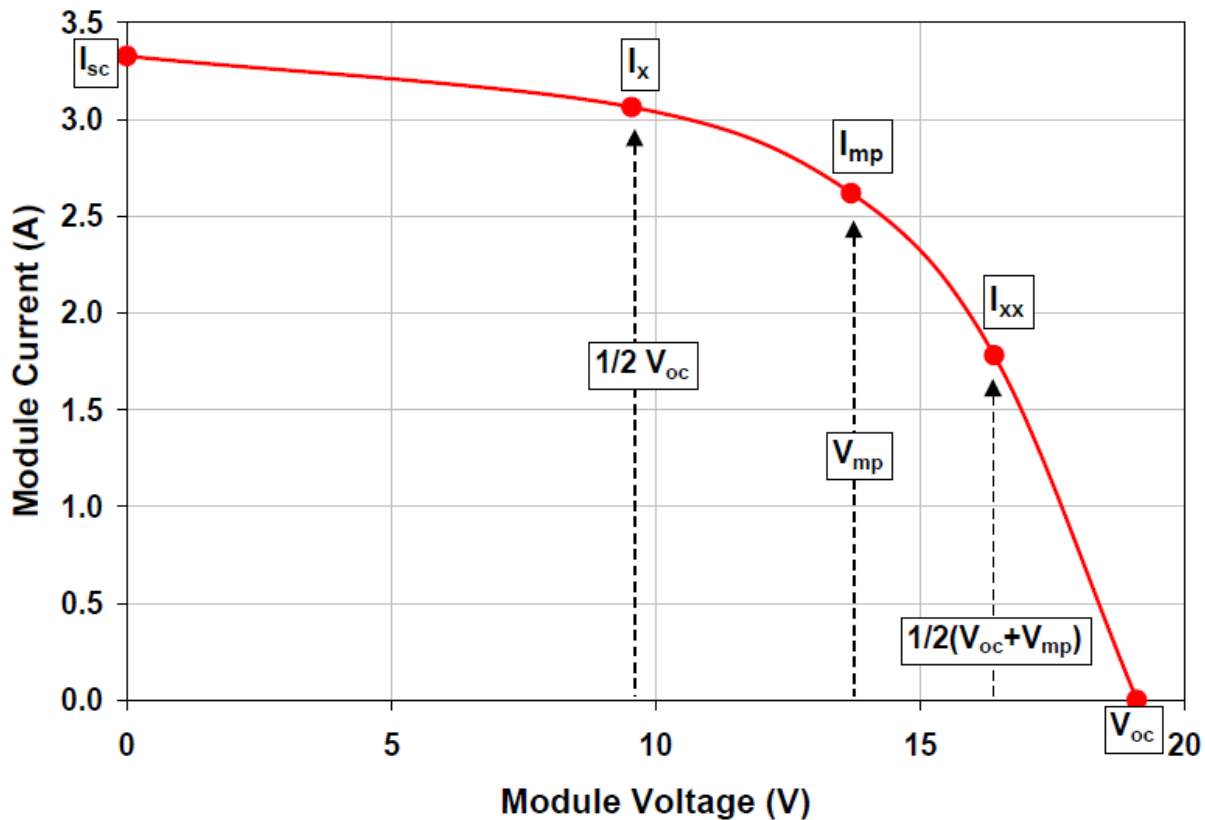


Figure 2.6: Illustration of a module I-V curve showing the five points on the curve that are provided by the Sandia performance model

There are several additional parameters that are obtained throughout numerical regressions analyses based on the model's equations. These are irradiance, solar resource and temperature dependent parameters. To illustrate them, it is necessary to define the Effective Irradiance that a PV module is exposed to:

$$E_e = I_{sc} / [I_{sc0} \cdot \{1 + \alpha_{I_{sc}}(T_c - T_o)\}] \quad (2.10)$$

where  $\alpha_{I_{sc}}$  is the normalized temperature coefficient for  $I_{sc}$ ,  $I_{sc0}$  is the short-circuit current at standardized conditions,  $T_c$  is the cell temperature and  $T_o$  is the reference cell temperature, typically  $25^\circ C$ . The  $E_e$  value describes the fraction of the total solar irradiance incident to the module to which the cells actually respond. Equation (2.10) is utilized directly with tabulated solar resource data for module performance predictions. Alternative procedures have to be utilized with direct measurements of solar resource data, for determining the effective irradiance and thus predict the module performance.

## Irradiance Dependent Parameters

Figure 2.7 illustrates the variation of measured values for module  $V_{mp}$  and  $V_{oc}$  as a function of effective irradiance. Previous values shown in Figure 2.5 were first translated to common temperature ( $50^\circ C$ ), in order to remove temperature dependence. In this case, the previously mentioned voltages increase with irradiance values. Figure 2.8 illustrates the variation of measured values for module current ( $I_{sc}$ ,  $I_{mp}$ ,  $I_x$ ,  $I_{xx}$ ) as a function of the effective irradiance, similar to the previous analysis, temperatures were translated to a common temperature to remove dependence. The previously mentioned current values increase with irradiance levels.

## Parameters Related to Solar Resource

Solar irradiance data can be manipulated using different methods and models in order to calculate the expected hourly-average solar irradiance incident on the surface of a PV module positioned in a certain orientation. In long-term performance monitoring, the solar irradiance in the plane of the module is often a measured value and should be used directly in the performance model.

This model utilizes empirical functions,  $f_1(AM_a)$  and  $f_2(AOI)$ , that quantify the influence on the module short-circuit current ( $I_{sc}$ ) of variation in the solar spectrum and the optical losses due to solar angle-of-incidence. These functions are determined by a module testing laboratory using explicit outdoor procedures [20, 21]. For example, Figure 2.9 illustrates how the solar spectrum varies throughout the day and from morning toward noon, influencing on the normalized short-circuit current of a typical Si cell. For this kind of cells, the normalized short-circuit current response is higher at high solar air mass conditions than it is at solar noon. Random atmospheric conditions such as intermittent clouds, smoke, dust, and other meteorological occurrences can be considered slight influences that average out on a weekly basis, monthly or annual basis. Figures 2.10 and 2.11 illustrates typical examples for empirically determined functions.

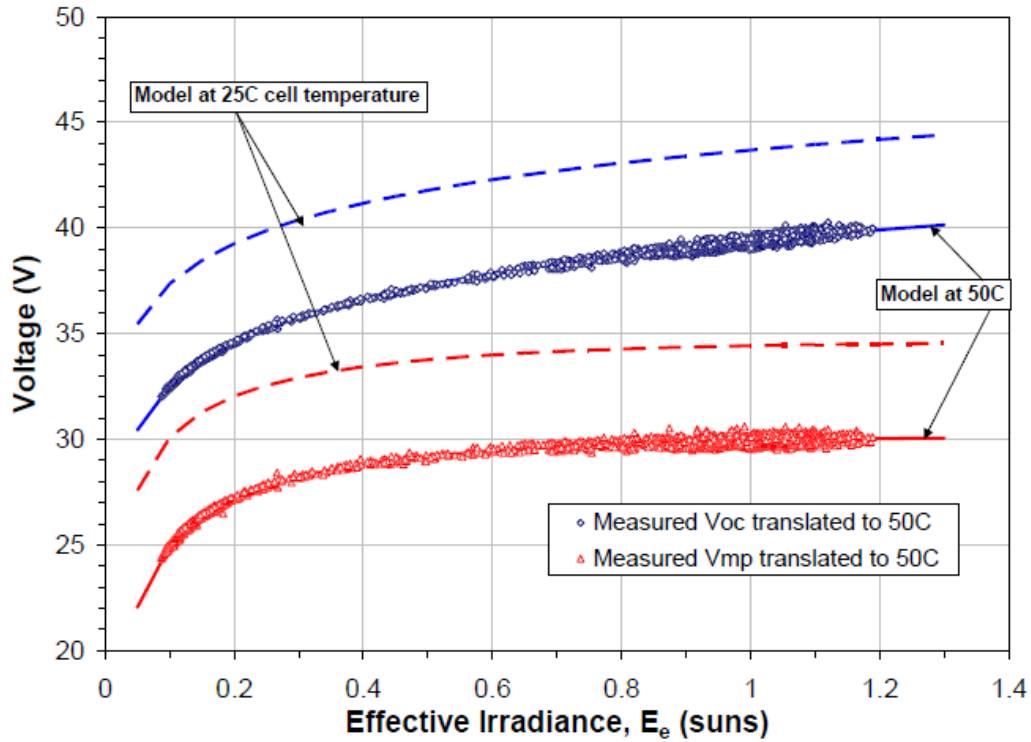


Figure 2.7: Over 3300 measurements values for  $V_{oc}$  and  $V_{mp}$ . Recorded and translated to a common temperature of  $50^{\circ}C$ , prior to regression analysis.

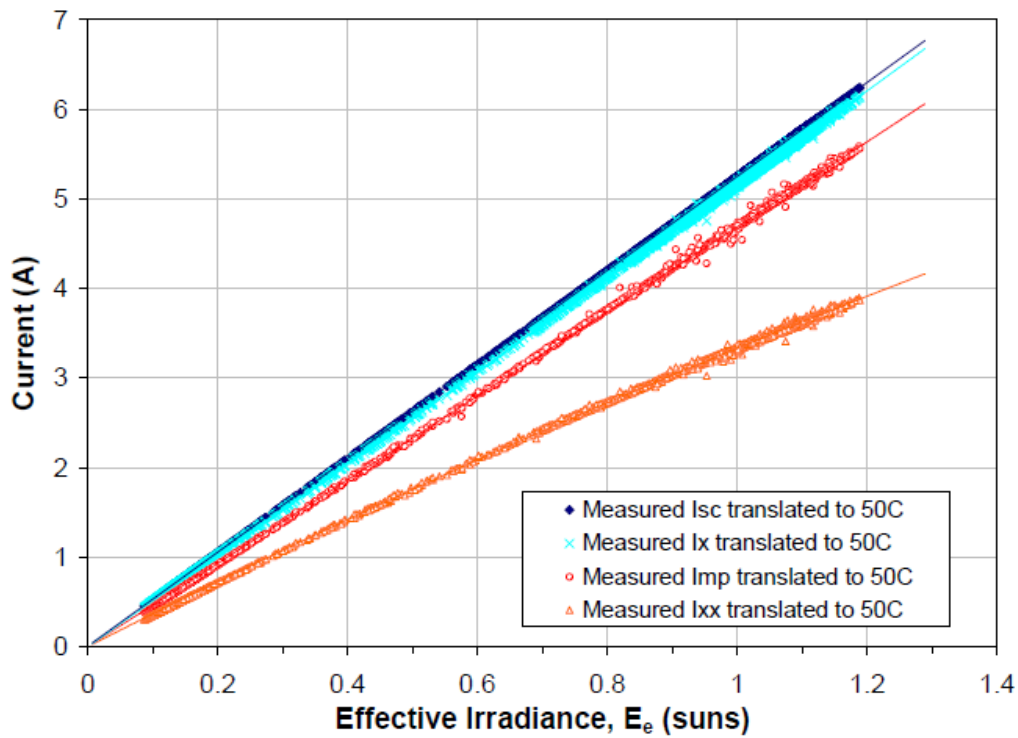


Figure 2.8: Over 3300 measurements values for module current. Recorded and translated to a common temperature of  $50^{\circ}C$ , prior to regression analysis

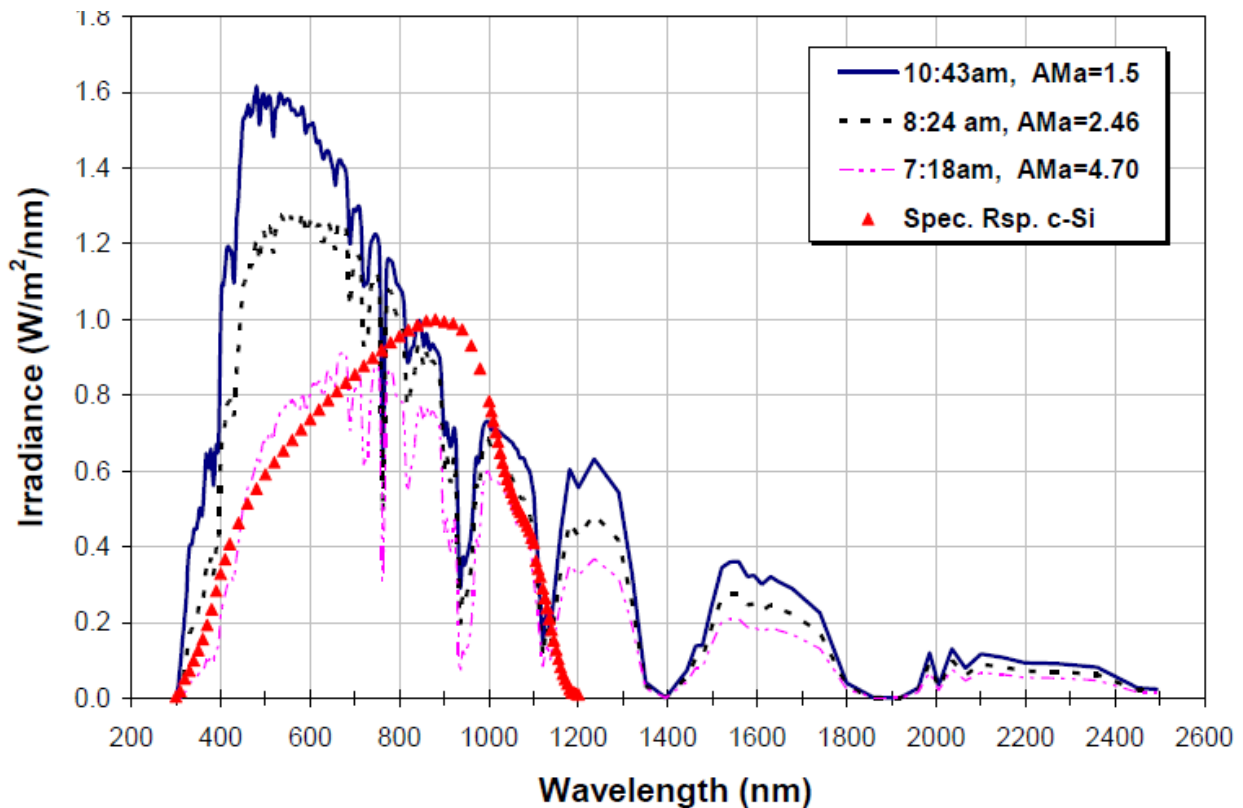


Figure 2.9: Measured solar spectral irradiance on a clear day at different conditions. The normalized spectral response of a typical silicon solar cell is superimposed for comparison.

It should be noted that, according to Figure 2.10, the influence of the changing solar spectrum is relatively small for air mass values between 1 and 2. It should be also recognized that over 90% of the solar energy available over an entire year occurs at air mass values lower than 3. The cumulative effect of the solar spectral influence on annual energy production is less than 3% [22]. On the other hand, the influence of optical losses for flat-plane modules is typically negligible for solar angle-of-incidence lower than 55 degrees, as shown in Figure 2.11. This loss is in addition to the loss associated to having the module surface not oriented perpendicular to the path of sunlight. In the case of vertically oriented flat-plate module in the south wall of a building (for the northern hemisphere), the annual energy loss due to optical loss is approximately 5% [22].

## Temperature Dependent Parameters

There are four temperature coefficients that are considered for the model, this coefficients affect the performance of a module according to it's operating temperature and/or as a function of effective irradiance that the module is receiving. Typically, this coefficients are provided by the module's manufacturer, although the coefficients for short-circuit current or closed circuit voltage are erroneously applied for maximum power current and voltage, respectively [16].



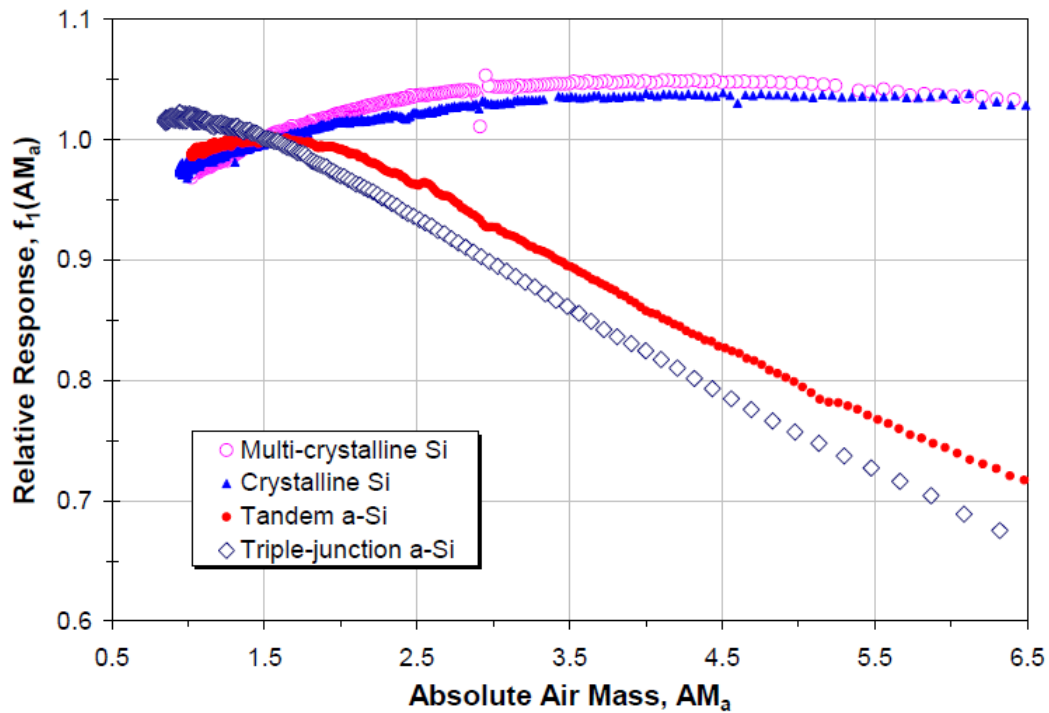


Figure 2.10: Typical empirical relationship illustrating the influence of solar spectral variation on module short-circuit current, relative to the  $AM_a = 1.5$  reference condition.

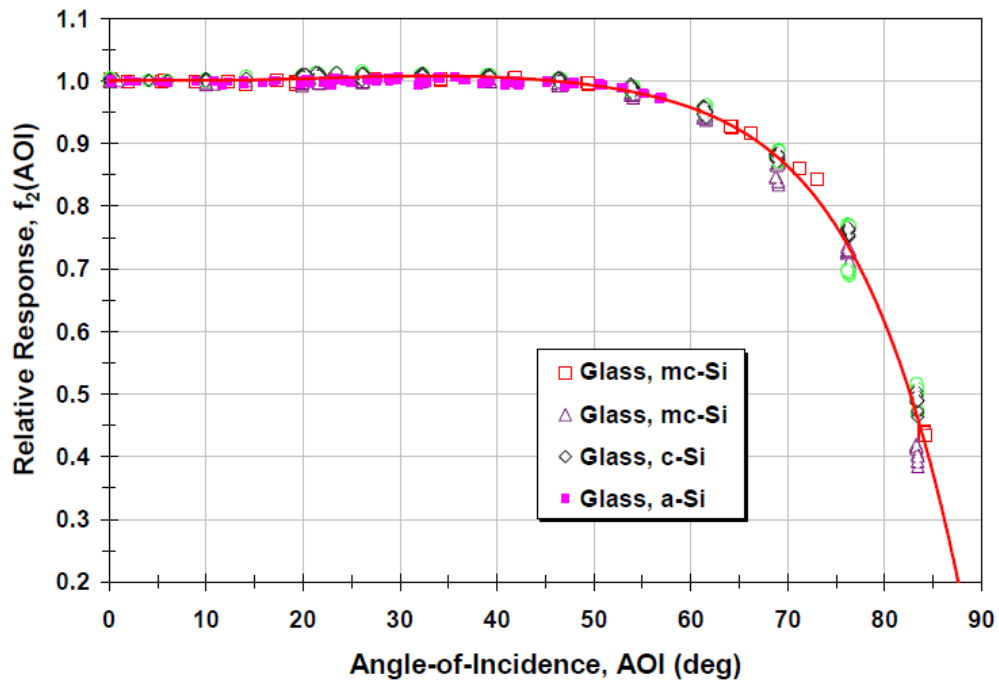


Figure 2.11: Typical empirical relationship illustrating the influence of solar angle-of-incidence in reducing a module's short-circuit-current.

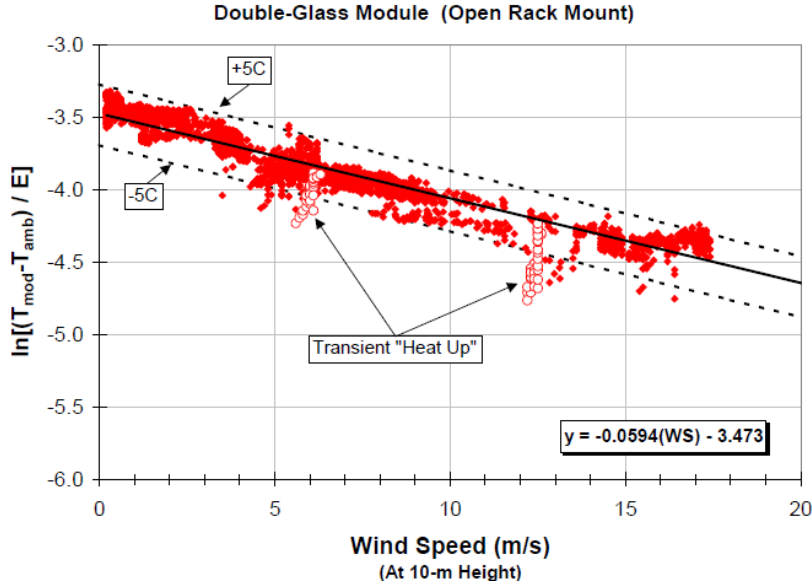


Figure 2.12: Experimentally determined relationship for back surface temperature as a function of solar irradiance, ambient temperature and wind speed. A linear regression fit provides the coefficients (a, b)

### Module Operating Temperature (Thermal Model)

A thermal model is required to estimate module operating temperature based on local environmental conditions such as solar irradiance, ambient temperature and wind speed. An empirically-based thermal model was recently developed by Sandia. This model has been applied successfully for flat-plate modules mounted in an open rack and for flat-plate modules with insulated back surfaces simulating building integrated situations, among others. This model has proven to be very adaptable and has an accuracy of about  $\pm 5^{\circ}\text{C}$ , which translated into less than a 3% effect on the power output from the module. This thermal model is as follows:

$$T_m = E \cdot (e^{a+b \cdot WS}) + T_a \quad (2.11)$$

where  $T_m$  is the back-surface module temperature,  $T_a$  is the ambient air temperature,  $E$  is the solar irradiance incident on module surface,  $WS$  is the wind speed measured at standard 10[m] height above ground,  $a$  is the empirically-determined coefficient establishing the upper limit for module temperature at low wind speeds and high solar irradiance and  $b$  is the empirically-determined coefficient establishing the rate at which module temperature drops as wind speed increases.

Figure 2.12 illustrates typical measured data recorded on six different days with nominally clear conditions and a wide range of irradiance, wind speed, and wind direction. The module in this case was a large-area 300-W model with tempered-glass front and back surfaces. The effect of non-equilibrium ‘heat up’ periods ( $\sim 30$ -min duration) is illustrated for two mornings when the sun first illuminated the module. A linear fit to the measured data provided the intercept and slope (a, b) coefficients required in the model. After the coefficients have been determined for a specific module then it is also possible to calculate the nominal operating cell temperature (NOCT) specified by ASTM [16].

Cell temperature and back-surface module temperature can be distinctly different, particularly for concentrator modules. The temperature of cells inside the module can be related to the module back surface temperature through a simple relationship. This relationship is based in an assumption of one-dimensional thermal heat conduction through the module materials behind the cell. The cell temperature inside the module is then calculated using a measured back-surface temperature and a predetermined temperature difference between the back surface and the cell and is as follows:

$$T_c = T_m + \frac{E}{E_o} \cdot \Delta T \quad (2.12)$$

where  $T_c$  is the cell temperature inside the module,  $T_m$  is the measured back-surface module temperature,  $E$  is the measured solar irradiance on module,  $E_o$  is the reference solar irradiance on module and  $\Delta T$  is the temperature difference between the cell and the module back surface at an irradiance level of  $1000[W/m^2]$ . This temperature varies, depending on the module mounting type.

Table 2.1 provides empirically-determined coefficients found to be representative of different module types and mounting configurations. The cases in the table can be considered generic for typical flat-plate photovoltaic modules from different manufacturers.

Table 2.1: Empirically determined coefficients used to predict module back surface temperature as a function of irradiance, ambient temperature, and wind speed.

Module Type	Mount	$a$	$b$	$\Delta T(^{\circ}C)$
Glass/cell/glass	Open rack	-3.47	-.0594	3
Glass/cell/glass	Closed roof mount	-2.98	-.0471	1
Glass/cell/polymer sheet	Open rack	-3.56	-.0750	3
Glass/cell/polymer sheet	Insulated rack	-2.81	-.0455	0
Polymer/thin-film/steel	Open rack	-3.58	-.1130	3

### 2.3.2 NREL's PVWATTS PV Performance Model

A much more simple model has been developed by the National Renewable Energy Laboratory (NREL). This model calculates the maximum power output that the module is delivering at a certain time, taking into account PV module parameters that are informed by it's manufacturer and other variables that can be calculated using previously reported methods. The model is as follows

$$P_{mp} = \frac{E}{1000} \cdot P_{mpo} \cdot [1 + \gamma(T_m - T_o)] \quad (2.13)$$

where  $P_{mp}$  is the maximum power to be generated,  $P_{mpo}$  is the nominal maximum power of the module,  $E$  is the plane of array (PoA) irradiation,  $\gamma$  is the power correction factor for module temperature,  $T_m$  is the PV module temperature and  $T_o$  is the reference temperature.

The PV module temperature can be calculated using the thermal model described in section 2.3.1, as well as the plane-of-array irradiance that is calculated using the procedure described in section 2.2.4

This model has an overall accuracy of 88% to 90%, compared to long-term studies performance models [19].

## 2.4 Thermoelectric Heat Pump

A Thermoelectric Heat Pump (THP) is a device based in the advantageous use of the Thomson's thermoelectric effect, which describes the heating or cooling of a current-carrying conductor [23]. This heat exchanger uses two different semi-conducting materials and their different Seebeck coefficients [24], to generate a continuous version of the Peltier effect [25]. This device has a basic configuration shown in Figure 2.13

This device is capable of transferring heat from it's cold side to it's hot side (against the temperature gradient) with a coefficient of performance (COP) higher than 1, this means that for every unit of electrical energy that flows through the conducting material, more than 1 unit of thermal energy delivered from the cold side the the hot side. On the other hand, this kind of devices have several constraints as for maximum operating temperatures, maximum power input and maximum allowable temperature difference, being this last factor the most influencing factor in the device's COP. As shown in Figure 2.14, a device with a hot side fixed at  $300K$  can reach COP's of less than 1 if the temperature difference is high enough.

Thermoelectric heat pumps are a contemporary solution to temperature control needs, from maintaining computer hardware chilled to heating small enclosures, this devices are used broadly in thermal applications.

A novel water heater, integrating a thermoelectric heat pump with a separating thermosiphon has been developed in 2005 [27]. This device reached a Coefficient of Performance (COP) greater than 1.6 for suitable operating conditions, although it still has a moderately high power consumption during operation, up to 3[kW].

Combining different applications onto the utilization of thermoelectric technology has led the development of an air source (AS) THP for simultaneous cold air delivery and hot water supply [28]. As shown in Figure 2.15, this device uses heat sinks and TEMs to simultaneously chill ambient temperature air and heat a water supply, using only electricity. In this device, there's heat being transferred from the air into the water flow, as well as heat flow coming directly from the TEMs into the water supply. This system, the study concludes, has more potential to be applied in domestic heating water due to the advantages of its small size, high feasibility and flexibility.

TEM can be used as electrical generators, given the Seebeck Effect [24]. When the two sides of a TEM maintain a temperature difference, a voltage is generated between the two sides. An application of this effect has been developed for a net zero energy building (NZEB) [29]. Coupling this thermoelectric generators (TEG) to the back of solar photovoltaic panels and solar thermal collectors increases the overall energy input into the system. A combination of TEG and THP used in the energy generation systems, water heating systems and air

handling units present in a NZEB (Fig 2.17) has improved the building's energy balance, as shown in Figure 2.16.

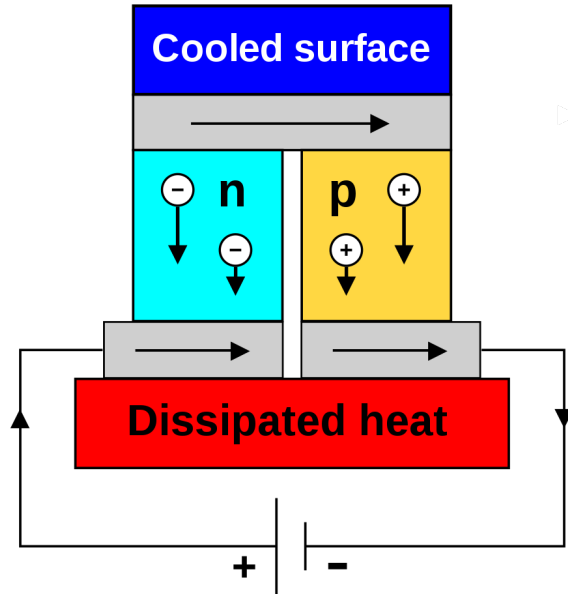


Figure 2.13: Thermoelectric circuit composed of different Seebeck coefficient's semi-conducting materials, configured as a Thermoelectric Heat Pump. Image by Ken Brazier.

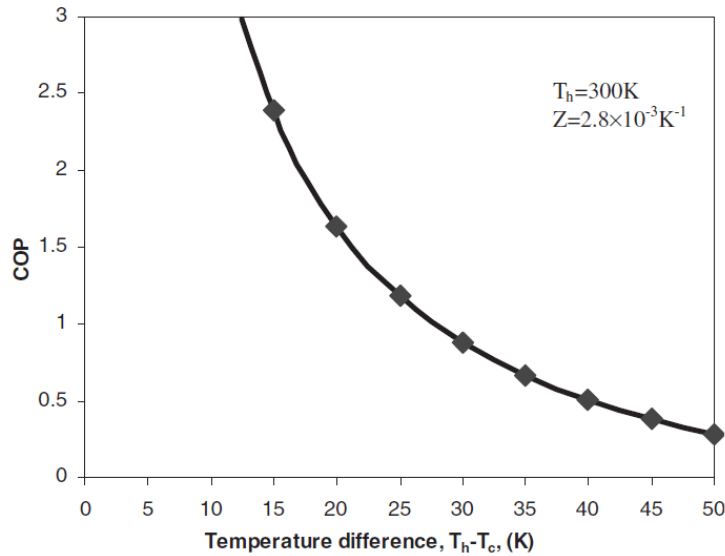


Figure 2.14: Coefficient of performance of a thermoelectric heat pump given a temperature difference, with it's hot side fixed at 300K.

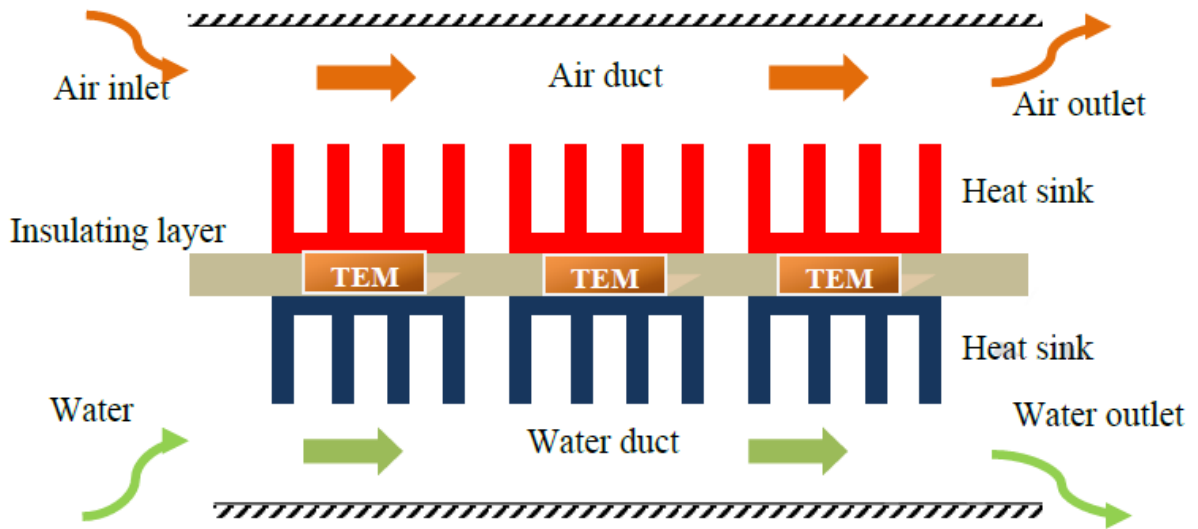


Figure 2.15: Schematic diagram of AS-THP

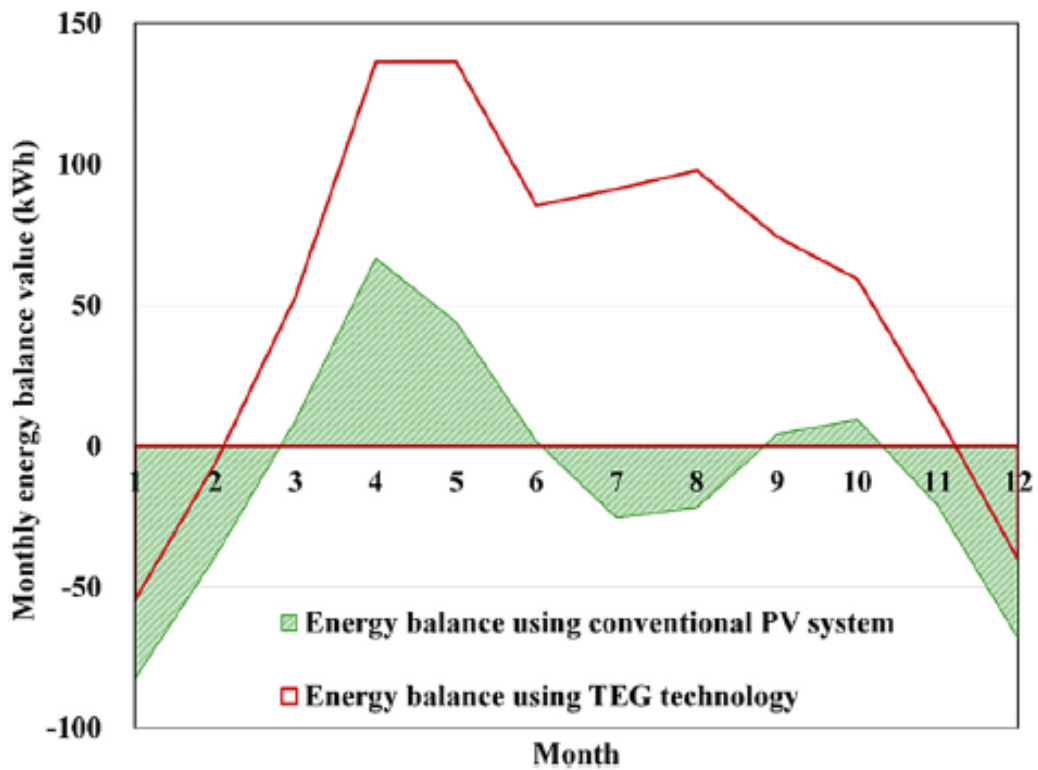


Figure 2.16: Building annual energy balance as conventional PV system and TEG integrated system.

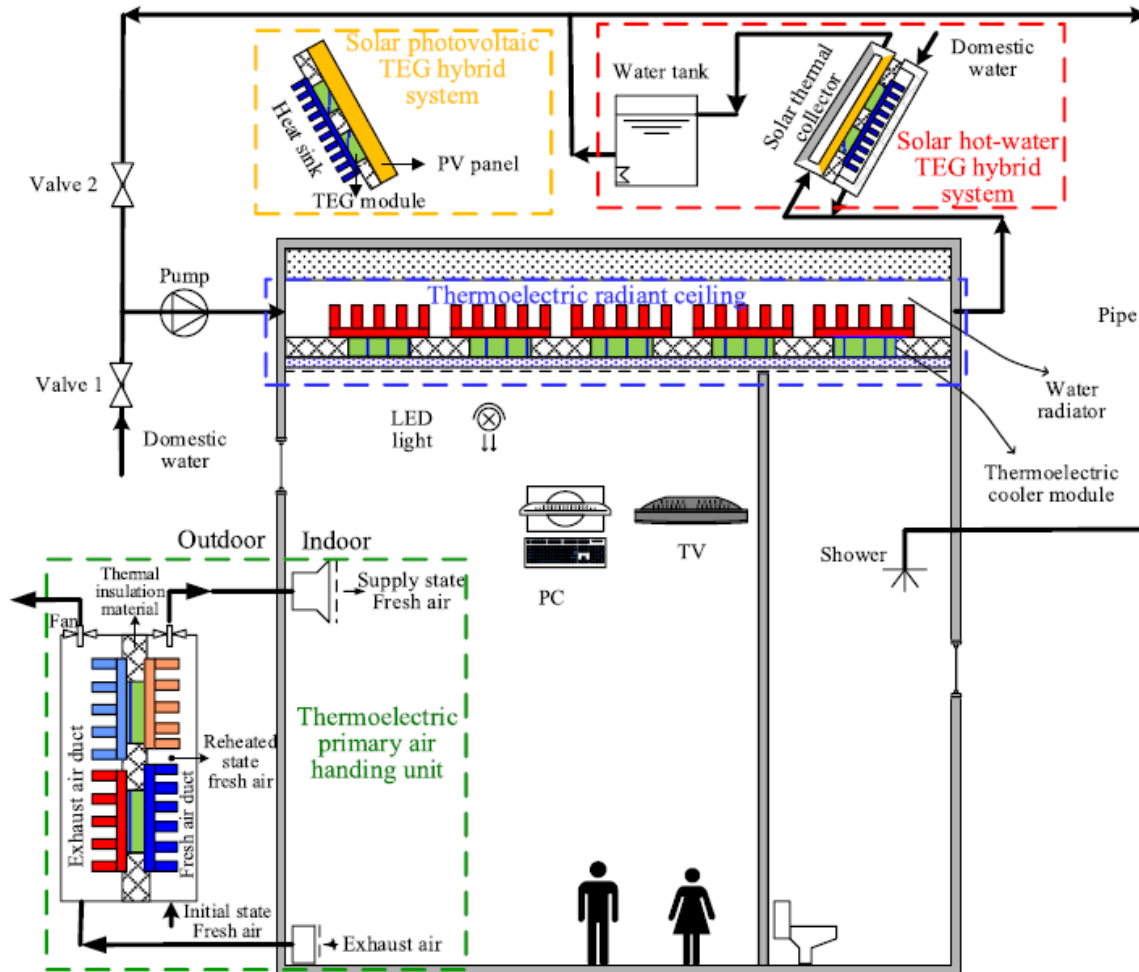


Figure 2.17: Schematic of the integrated thermoelectric systems

## 2.5 Nexol Water Boiler

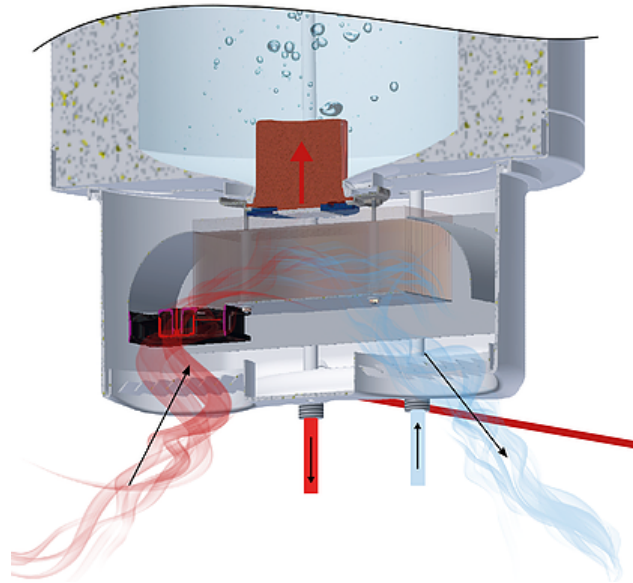


Figure 2.18: Nexol's preview of its water heater internal function. Source: Nexol-AG

The Nexol Water Boiler that will be investigated consists in an insulated, 40 liter, water tank with a THP installed in its bottom. This THP drives heat from a forced flow of ambient air into the water tank, increasing the water's temperature and decreasing ambient air flow's temperature (Fig 2.18), using energy provided by a PV panel installed nearby. The forced flow is achieved by having a low power fan installed at one end of an air duct, driving air through a heat sink attached to the cold side of the THP. It is estimated that the cold side of the THP reaches temperatures  $10K$  below ambient air temperature and the hot side of the THP reaches temperatures  $2K$  above the adjacent water, given the flow regime of the fluids.

The tank will have an internal natural convection phenomena, given the location of the heating element, as well as non-negligible heat loss through its walls. The natural convection will not be intense, thus generating a stratification of the fluid inside the tank.

Due to having a THP as a power source, this water heater behaviour is largely dependent on the ambient temperature and internal water temperature. As explained in section 2.4, the amount of heat transferred from the ambient air into the tank's water will greatly decrease with a larger temperature difference between these two fluids. Therefore, if the ambient temperature is too low, the temperature that the internal water can reach will be greatly impaired. Furthermore, lower ambient temperature could impair an internal temperature rise due to heat loss through the tank surface.



## 2.6 Similarity Measures

Sum-of-square based error may be difficult to implement on an inverse analysis study. In the case of materials studies, curves representing multiple tension-compression hysteresis loop are the main resource to identify the studied material parameters. Five alternative measures of similarity between curves have been investigated for this application [26].

Generally, after some experiment is conducted on a material, a numerical model is created to replicate the physical conditions of the test (Fig. 2.19), an inverse analysis determines the parameters of the numerical model by minimizing the difference between experimental data and the response of the numerical model. Optimization is used to find the parameters by minimizing an objective function which describes the quality-of-fit from the collection of parameters. Using a genetic algorithm methodology having Partial Curve Mapping (PCM), Area between curves, discrete Fréchet distance, Dynamic Time Warping (DTW), or Curve Length as an objective function to be minimised. Progression of the objective value for these five functions using the GA methodology can be seen in Figures 2.20 and 2.21 for clean and noise added experimental curves, respectively. The PCM based objective function has the lowest value for both cases.

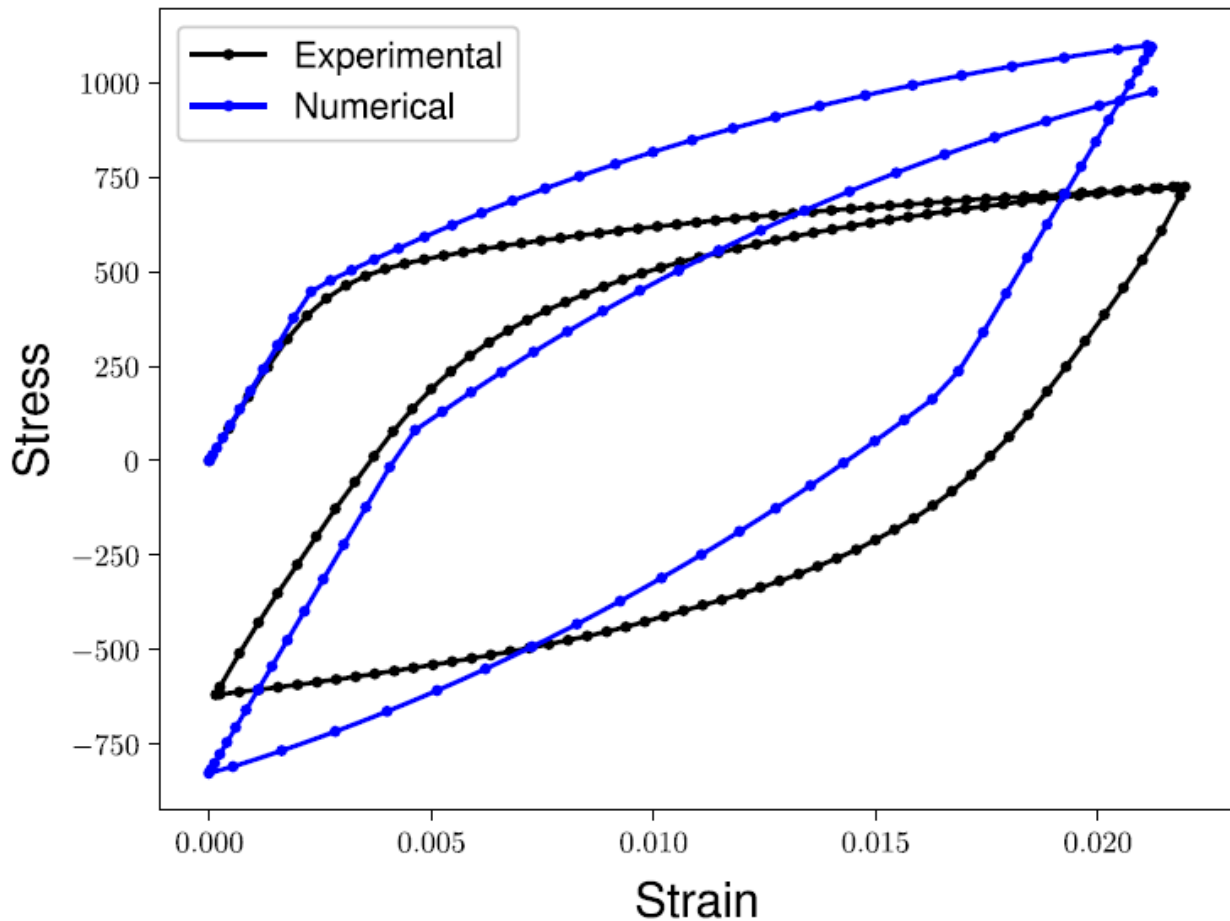


Figure 2.19: Hysteresis curve from experimental and numerically simulated data.

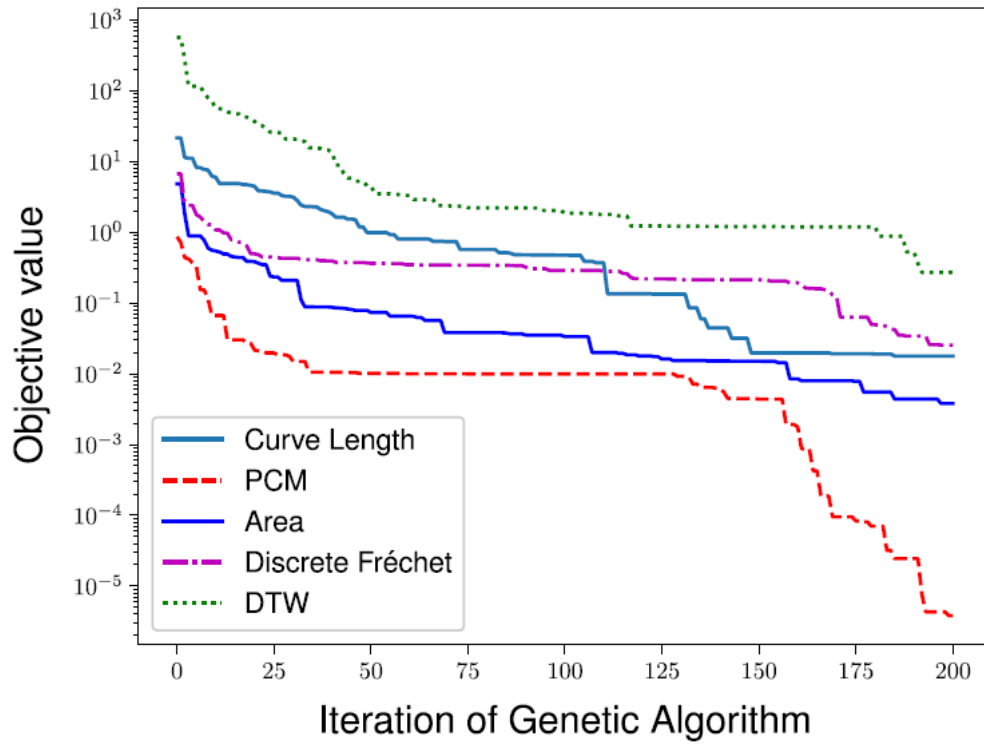


Figure 2.20: Plot of the objective value as a function of the iteration of the Genetic Algorithm for clean experimental curves

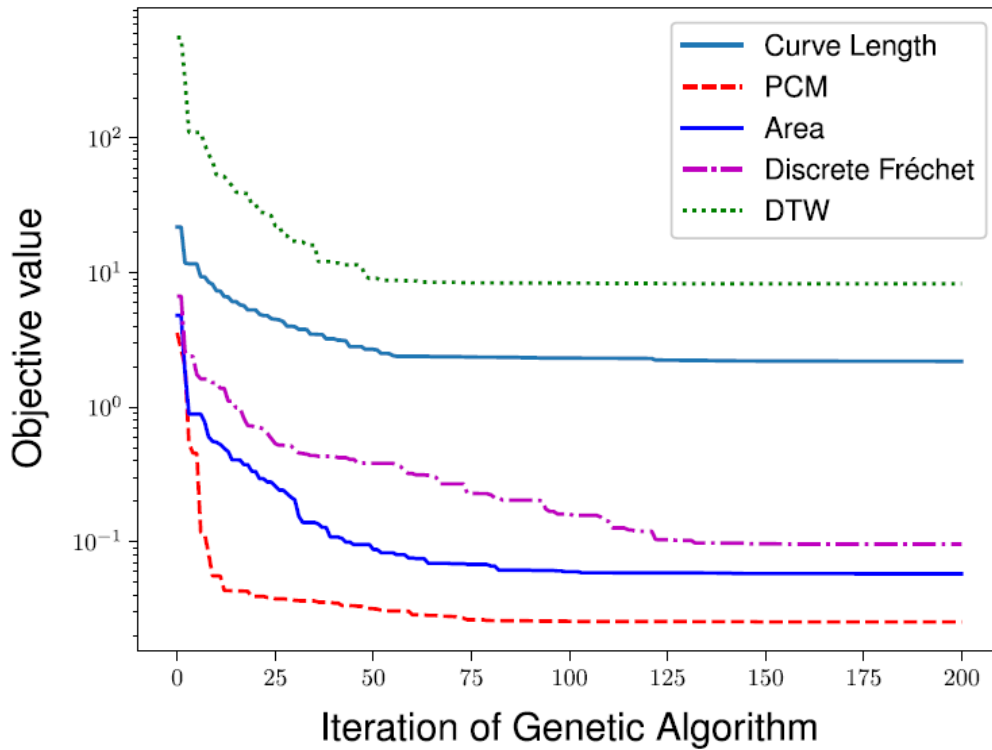


Figure 2.21: Plot of the objective value as a function of the iteration of the Genetic Algorithm for noise-added experimental curves.

## 2.7 Conclusions

There are several variables that need to be provided to a solar photovoltaic (PV) numerical model for modeling the maximum power output a particular PV system can generate. These variables can be calculated using measured solar irradiance data and weather data of the system location or Typical Meteorological Year (TMY) data of the area where the system is going to be installed, and technical data of the PV system such as the materials and orientation of the PV module, among others. Simulated photovoltaic array power output data is necessary to enable the simulation of any solar powered device, including the device that is going to be studied in this Thesis work, the Nexol Boiler.

Thermoelectric Modules (TEMs) have a broad range of potential uses, depending on the configuration of their components, THPs being one of them. Having a complex behaviour, several simplifications have to be done in order to properly simulate the heat source of the studied device.

Experimentally obtained data needs to be compared to the output data of the simulated numerical model that has been developed for the studied device. For this purpose, similarity measures can be utilized to numerically determine the differences between these data sets and, with the aid of a genetically based algorithm, improve the numerical model's accuracy by modifying its parameters and minimizing a function that describes the quality-of-fit of the model's output data.

The presented background enables the creation of a methodology for this investigation, focused in data acquisition, development, optimization and utilization of numerical models, development of performance measurements and performance evaluations of the simulated device in determined locations.

# Chapter 3

## Methodology

This chapter will explain the methodology used for data acquisition, as well as showing the experimental setup used, give an overview to the numerical simulation used to determine the energy generated by the used PV modules and explain the stratified tank numerical model considered for this thesis with it's improvement methodology. For yield determination purposes, this chapter will also inform about performance measurements methods as well as extrapolation of an improved numerical model applied in other locations.

### 3.1 Data Acquisition

The data that needs to be acquired is going to be used to determine the energy generated by the PV system during it's operation, as well as obtaining temperature draw profiles for optimization and validation of the stratified thermal storage tank numerical model. To successfully obtain this data, an experimental setup capable of sustaining a series of tests in a controlled environment is required.

#### 3.1.1 Experimental Setup

The experimental setup is divided into two parts: wet and dry components. The main wet components are the studied device, three thermocouples, two flow meters, a thermostatic mix valve, a solenoid valve and heat resistant PPR piping. The dry components are a PV module, a DataLogger, a programmable electric actuator and an Uninterruptible Power Supply (UPS). These components and their interactions are represented in Figure 3.1

A structure to place all these components was designed using Computer Assisted Design (CAD) tools, which allowed to generate the needed blueprints for later manufacturing.

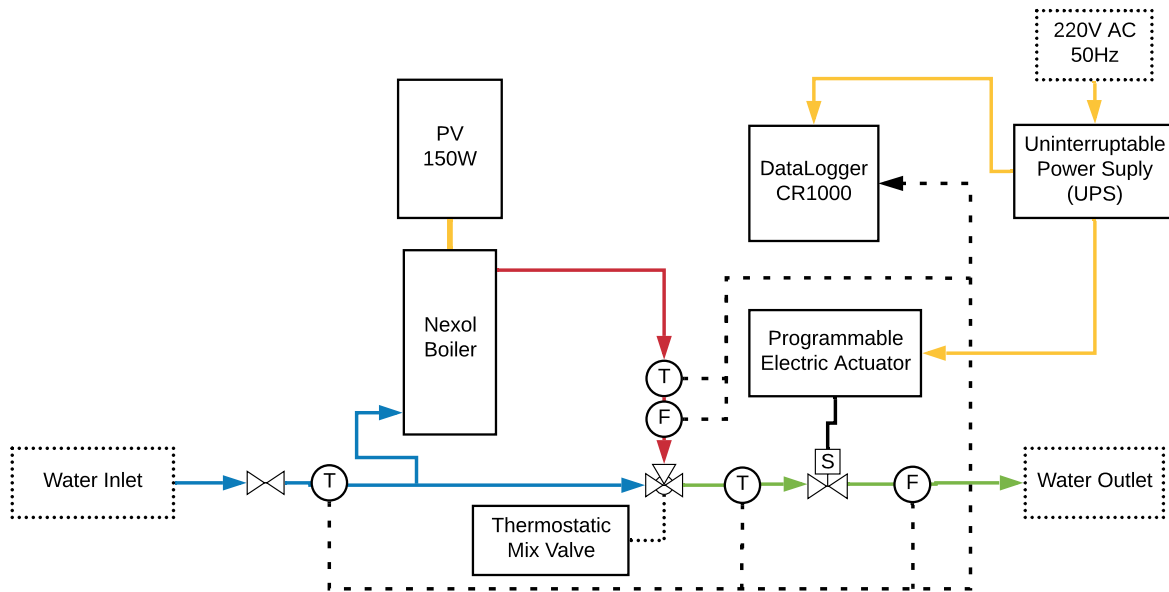


Figure 3.1: Diagram of the test rig, showing energy and water supply, as well as sensors for data acquisition



Figure 3.2: PV module installed at a 30 degree tilt, in a setup equivalent to an insulated rack mount



Figure 3.3: Sensorized test rig

## PV module

The geographical location of the experimental setup, thus the PV module, is tabulated in Table 3.1. This is the location of one of the Engineering faculty’s rooftops

Table 3.1: Coordinates of experimental setup

Latitude	Longitude	Height
-33.457317 [deg]	-70.664332 [deg]	577 [m]

The orientation of the PV module for the experiment is tabulated in Table 3.2. Where the tilt is the inclination relative the ground of the panel and the azimuth is the orientation relative to geographical north. In this case, the PV module is oriented directly northbound. Also, as shown in Figure 3.2, the PV module is a Glass/cell/polymer sheet type, mounted in an Insulated Rack equivalent.

Table 3.2: PV module’s orientation

Tilt	Azimuth
30 [deg]	0 [deg]

## Temperature and flow sensors

Amongst the wet components there are 5 sensor modules to acquire temperature and flow data, as shown in Figure 3.3. In this figure a thermostatic mixing valve can be identified by it’s red cap, it’s two vertical inlets (hot from below, cold from above) and it’s mixed water outlet.

## DataLogger

The DataLogger used for this setup is the model CR1000, manufactured by PC400. This device is able to collect, process and store data up to a frequency of 100[Hz]. For this experiment, the DataLogger has been programmed to acquire data at a rate of 2[Hz] and store temperature and flow averages every 5 seconds during the water draws imposed to the studied device, as scheduled. In Figure 3.4, this device is installed above the programmable electric actuator and its powered by the UPS, which is the black device located at the foreground of the picture.

### 3.1.2 Meteorological data

The main meteorological data needed for this study is comprehended by global, direct and diffuse irradiances averages in periods of one minute, which are measured using the Mechan-



Figure 3.4: DataLogger(above), programmable electric actuator (middle) and UPS (below). Installed inside a safe box

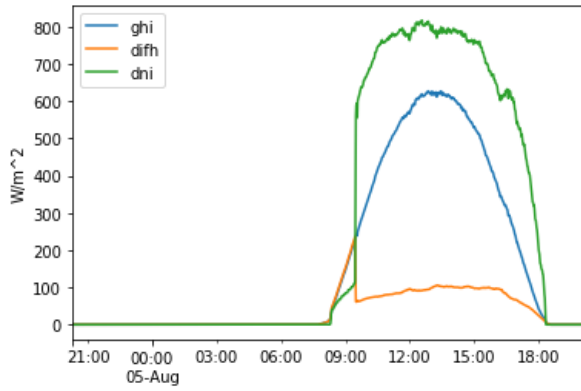


Figure 3.5: Irradiance data acquired for a mostly sunny day

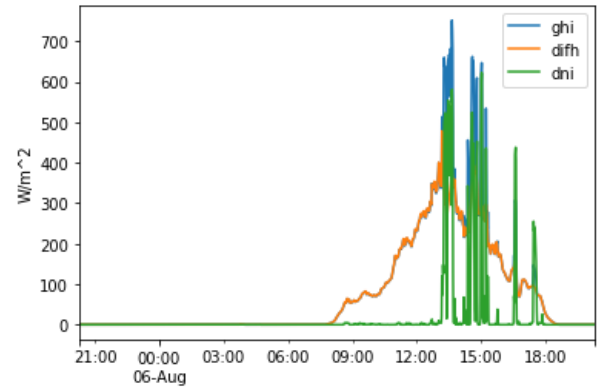


Figure 3.6: Irradiance data acquired for a mostly cloudy day

ical Department meteorological station’s pyranometer and pyrliometer. Supplementary meteorological data such as average ambient temperature and wind speed is required, also in periods of one minute, which are measured using the Geophysics Department measuring anemometer and thermometer. In Figures 3.5 and 3.6, a decomposition of irradiation curves are shown for a sunny and cloudy day. This decomposition consist in the direct normal irradiance (dni), the diffuse irradiance for an horizontal plane (difh) and the global irradiance for an horizontal plane (ghi).

### 3.1.3 Tests schedule

The test schedule is presented in Table 3.3. These tests, carried out during the investigation, consists in different draws of hot water from the system. These demand profiles are intended to provide different scenarios in which the tank may perform, as hot water can be drawn for dish-washing as well as showers, among other uses.

It is necessary to note that the first part of the tests were carried out using a 100[W] PV Module as power source, and a second batch of tests were performed using a 150[W] PV Module as said power source. Once this schedule has been completed, the tests for the 150[W] PV panel were replicated until the device was withdrawn by it’s provider, Endurance Electric.

## 3.2 Numerical simulation

Two different numerical simulations are needed to model the studied tank’s yield. One model for PV generation and another for the stratified tank’s thermal behaviour.



Table 3.3: Test Schedule

Start/End date	Time of Day	Draw Duration [min]	Power source [W]
05-08-2019 11-08-2019	18:00	5	
12-08-2019 19-08-2019	7:00	5	100
19-08-2019 26-08-2019	14:00 18:00	1 5	
26-08-2019 28-08-2019	20:00	10	
29-08-2019 05-09-2019	18:00	5	
06-09-2019 12-09-2019	7:00	5	150
14-09-2019 23-09-2019	14:00 18:00	1 5	
24-09-2019 26-09-2019	20:00	10	

### 3.2.1 Photovoltaic array electricity generation

Having the geographical position of the experimental setup, the solar position can be calculated for each time of the day during the experiment. Then, with the information of the experimental setup and available meteorological data, the angle-of-incidence, airmass and plane-of-array irradiance can be calculated. The PV module and cell temperature can be calculated using the thermal model developed by SANDIA Laboratories (Section 2.3.1).

Once all these parameters have been calculated, the average power generation, minute by minute, can be calculated and plotted using Equation (2.13)

### 3.2.2 Stratified Tank numerical model

The numerical model used for the simulation of the stratified tank is based in the TRNSYS Type 154 numerical model, represented in Figure 3.7. This model considers an insulated stratified water tank, heated by an auxiliary source located in it's upper section, thus stratifying the fluid mainly by conduction of heat. The dominant equation for this model is an energy balance over each fluid node (j), as shown in the following Equation:

$$\rho c_p V_j \frac{dT_j}{dt} = \dot{Q}_{massflow,j} - \dot{Q}_{loss,j} + \dot{Q}_{aux,j} + \dot{Q}_{cond,j} \quad (3.1)$$

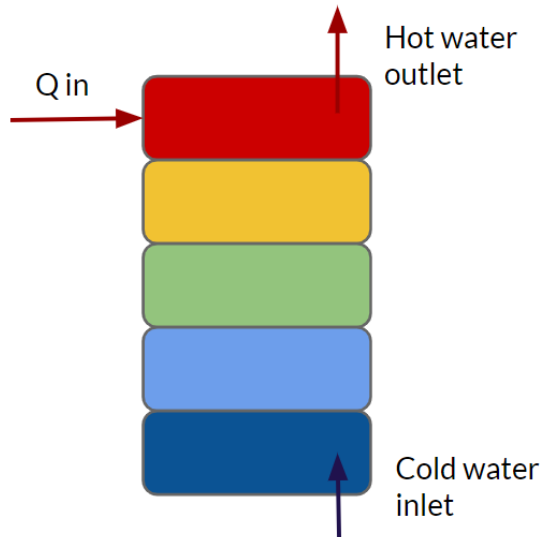


Figure 3.7: Simplified representation of TRNSYS Type 154 numerical model for thermal storage tank

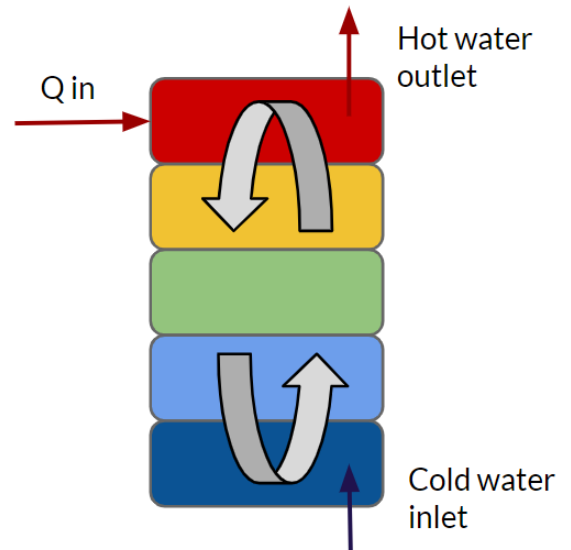


Figure 3.8: Simplified representation of adapted simulation model, with forced mixing between nodes

This equation can be solved analytically if it is written in the form shown as follows

$$\frac{dT_j}{dt} = aT_j + b \quad (3.2)$$

where  $T_j$  is the dependent variable,  $t$  is time,  $a$  is a constant and  $b$  may be a function of time or of the dependent variable, which in this case it's not constant. A reasonable approximation to the analytical solution can be found by assuming that  $b$  is constant over the time-step and equal to it's average value during said time-step.

This base model will be modified to match the behaviour of the studied device, as described below.

## Model definitions and simplifications

This numerical model is compromised of a stratified thermal storage tank, modeled as stacked nodes of fluid, that has a water inlet at it's bottom, a water outlet at it's top as well as an auxiliary water heater in it's upper node. To imitate the studied device configuration, an adjustable mixing factor between nodes is imposed

The stratified thermal storage tank model is compromised of six different parameters that describe the tank's geometry and thermal properties for it's initialization. The initialization parameters are listed below.

1.  $H$ : Tank's height [ $mm$ ]
2.  $V$ : Tank's contained fluid volume [ $m^3$ ]

3. Nodes: Number of subdivisions used for the stratified tank's simulation  $[-]$
4. Maximum Temperature: Tank's temperature threshold for heating activation and deactivation purposes  $[K]$
5. Loss Coefficient: Tank's global heat loss coefficient  $[W/K]$
6. Mix Coefficient: Tank's node mix coefficient  $[-]$

The tank's diameter is automatically calculated and depends on its volume and height. It is important to notice that the number of nodes that the model will be working with throughout the simulation is fixed and non dependent of the tank's volume. Also, the heat loss coefficient is considered independent from the tank's surface area, simplifying the numerical model.

The tank's node mix coefficient, represented with grey arrows in Figure 3.8, is one of the most important initialization variables for this adapted numerical model. This coefficient controls the proportion of mass that will be mixed between nodes for each time-step of the simulation, thus forcing the existence convection of the fluid inside the tank.

The two parameters that will partake the optimization of the model are the heat loss coefficient, and the forced mix coefficient. The heat loss coefficient is considered a critical parameter due to its simplified form and the uncertainty of its approximated value. The forced mix coefficient is considered a critical parameter due to influencing directly in the tank's stratification and, therefore, the hot water temperature draw profile. Furthermore, the number of nodes considered for the tank's simulation and improvement is fixed at six nodes with a height of 100[mm] each.

## Model's basics

This transient numerical model considers four instantaneous inputs for each time-step that is being computed.

1. Ambient temperature  $[K]$
2. Inlet temperature  $[K]$
3. Power input  $[W]$
4. Instantaneous water flow  $[m^3/s]$

These input variables as well as the internal properties of the tank are used to compute a new state for each time-step of the ongoing simulation.

The computation of each time-step follows the procedure shown in Figure 3.9

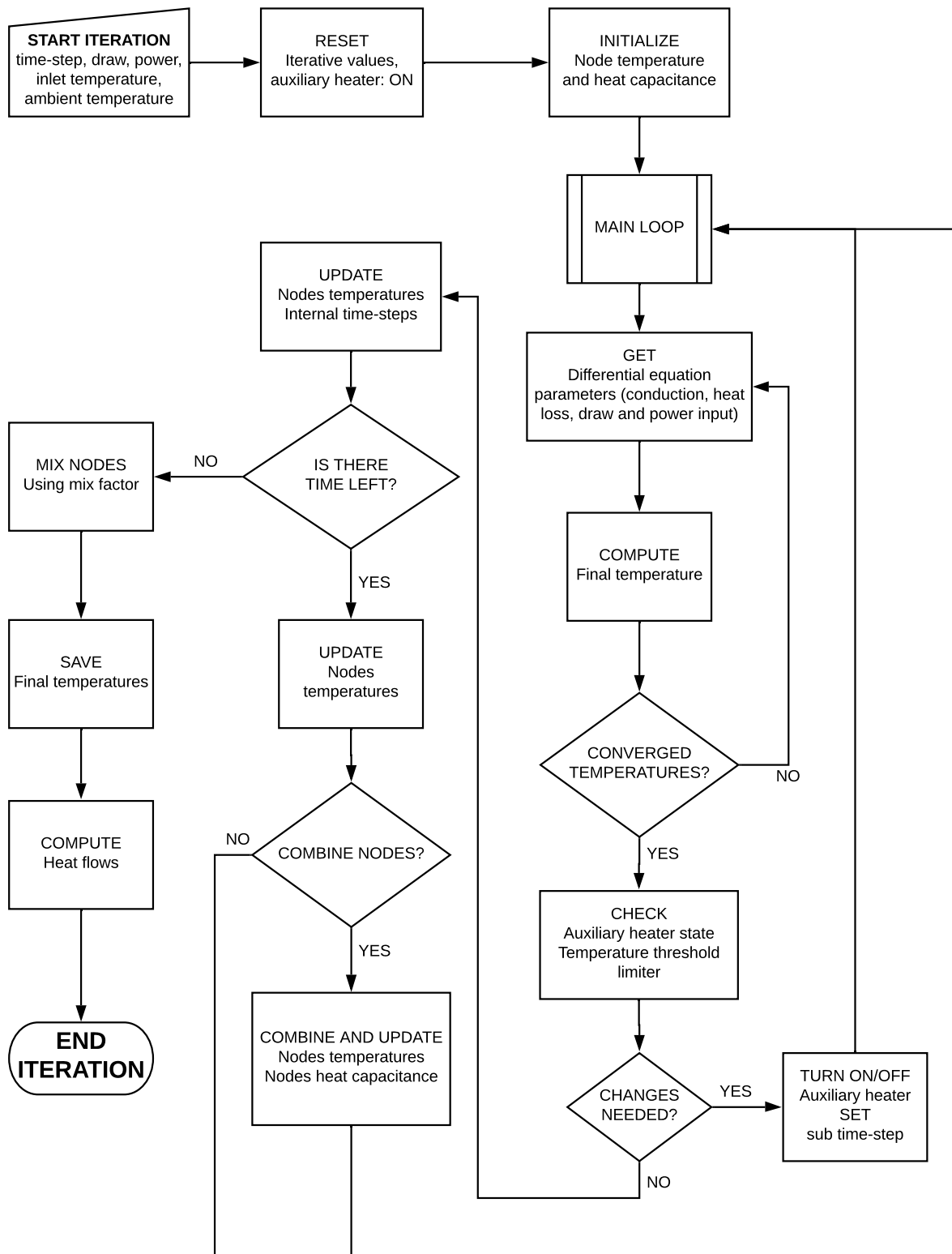


Figure 3.9: Flow diagram for the computation of each time-step

## Heat input simulation

Each THP has an unique set of properties an characteristics inherent to the materials is made from and the configuration of it's components, thus having a set of curves that describes the behaviour of the device. Not knowing the device's model, materials, dimensions and not having it's set of characteristic curves, making the correct assumptions is of utmost priority.

A curve analysis has been done to the Figure 2.14, obtaining an exponential expression for it's shape:

$$\text{COP} = A + B \cdot e^{(C \cdot \Delta T)} \quad (3.3)$$

where  $\Delta T$  is the temperature difference between the hot and the cold side of the Thermo-electric Module, and  $A$ ,  $B$  and  $C$  are constants with values shown in Table 3.4

Table 3.4: Constants of exponential approximation for the COP of a THP

Constant	A	B	C
Value	0.19787147465642063	7.301163252727839	-0.08016612419376098

With this expression, the amount of heat being transferred into the tank is computed for each time-step, given the DC power delivered by the PV system and estimated temperature difference between the hot and cold side of the THP.

### 3.2.3 Model's accuracy optimization

Given that many aspects of the numerical model are subdued to constants that are to be determined, the selected methodology to improve the model's accuracy is based in quality-of-fit optimization. The formulation for optimizing the numerical model of the thermal storage tank is as follows:

$$\begin{aligned} \min \quad & f(S_e, S_m(p_1, p_2, \dots, p_n)) \\ \text{s.t.} \quad & p_i \geq 0 \quad \forall i \in \{1, 2, \dots, n\}, n \in \mathbb{N} \end{aligned} \quad (3.4)$$

where  $f()$  is the objective function to be minimized,  $S_e$  and  $S_m$  are the experimental and numerically obtained curves, respectively, and  $p_1$  to  $p_n$  are the n-parameters that define the numerical model.

Being this optimization based in an inverse analysis, a genetic algorithm (GA) procedure is utilized to pinpoint the values of the numerical model parameters that minimize the objective function. This GA will create a population of a given amount of individuals, each representing a model with different mix and heat loss coefficients. The algorithm evaluates the "fitness" of each individual and using selection, crossover and mutation procedures these individuals evolve throughout generations.

Table 3.5: Upper and lower bound values for attributes to be optimized by GA

Coefficient	Upper Bound	Lower Bound
Heat loss	5 [W/K]	0.2 [W/K]
Forced Mix	0.5 [-]	0.02 [-]

## Individuals

Each individual is an instance of the simulated thermal storage tank that differ only in 2 parameters or attributes: Mix coefficient and heat loss coefficient. The values of these attributes are randomly generated within a lower and upper bound, as shown in Table 3.5. It is important to notice that the mix coefficient cannot be more than 1, because a node cannot mix more than its entire mass with its adjacent nodes.

## Fitness

This is the most important aspect of any Genetic Algorithm, as it represents the performance of a given individual, which is based on the objective function of the optimization procedure. In this Thesis, the Partial Curve Mapping (PCM) comparison method between two curves is used as an objective function to be minimized.

The PCM method uses a combination of arc-length and area to determine the similarity between curves[26]. The algorithm for comparison can be described in few steps:

1. Acquire the curves to be compared
2. The arc-length of the shorter curve is imposed onto a section on the longer curve
3. Trapezoids between the curves are constructed
4. The total sum of the trapezoids areas is computed

This process is repeated for 200 iterations or so, as various offsets of the short arc-length curve are imposed on the curve with the longer arc-length. Trapezoids constructed between two curves can be seen exemplified in Figure 3.10. The final PCM value is the minimum area from all attempted arc-length offsets. As different values are imposed onto the attributes of each individual, different PCM values will be computed, thus obtaining the more accurate individuals and selecting them for the next generation in the algorithm.

## Selection

This step selects the fittest individuals from a generation to be passed onto the next generation. The method of selection used in this Thesis work is the Tournament Selection. This methodology is based in the selection of the fittest candidate from a sub-set of candidates

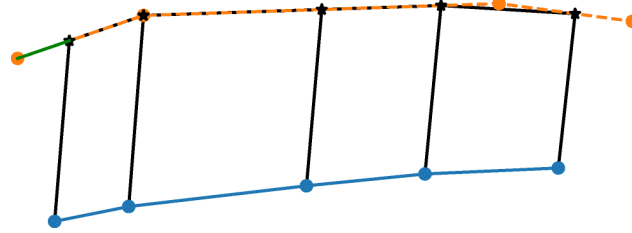
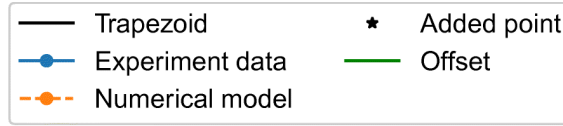


Figure 3.10: The PCM method construct trapezoids between two curves for every possible offset

present in the actual population of individuals. The algorithm for selection can be expressed in three simple steps:

1. Randomly select  $k$  candidates from the population
2. Select the best individual between the  $k$  candidates
3. Repeat 1 and 2 until the desired amount of individuals is selected for the next generation

These selected individuals are cloned to replenish the population original size.

## Crossover

The crossover step takes attributes from two random “parent” individuals and converts them into two new “offspring” individuals to take their place in the population. The method selected is based in a linear combination of the parents individual attributes as shown in the following Equations:

$$A_{i,O_1} = A_{i,P_1} - a \cdot (A_{i,P_1} - A_{i,P_2}) \tag{3.5}$$

$$A_{i,O_2} = A_{i,P_2} + a \cdot (A_{i,P_1} - A_{i,P_2}) \tag{3.6}$$

where  $A_i$  is the  $i$ -attribute of the individual,  $O_1$  and  $O_2$  are the offspring,  $P_1$  and  $P_2$  are the parents and  $a \in [0, 1]$ .

Each crossover consumes two parents and creates two offspring, thus maintaining the population size.

## Mutation

There is a need to increase variety amongst the actual population attributes, therefore a mutation method that randomly alters the attributes of an individual has to be implemented. The selected mutation method is the Gaussian Added Value, which adds to each attribute of the selected individual a normally distributed value with a pre-defined average value and variance, as shown in the following Equation:

$$A_{i_{new}} = A_i + x, \quad x \sim N(\mu, \sigma) \quad (3.7)$$

where  $x$  is the Gaussian Added Value,  $N$  is the Normal probability Distribution,  $\mu$  is the average value of the Normal Distribution and  $\sigma$  is the variance of the Normal Distribution.

## Overall parameters

For this genetic optimization of the model the steps previously described are repeated for a certain amount of generations. The overall parameters for this optimization are shown in Table 3.6

Table 3.6: Genetic Algorithm parameters

Parameter	Value
Population size	7
Generations	50
$k$	3
Selected individuals	3
Crossover chance	0.500
Mutation chance	0.200
$\mu$	0.000
$\sigma$	0.125

The curves to be compared are the experimentally obtained temperature profiles of consecutive water draws from the experimental setup and it's simulated equivalent given the same meteorological conditions, time constraints and instantaneous water flow. The described algorithm was executed for different data sets from the experimentally obtained values to obtain model candidates. These candidates are then utilized to simulate throughout the experiment's time frame, having their results compared to the experimentally obtained temperature draw profiles and it's associated performance.



## 3.3 Performance Measurements

To evaluate the performance of the studied device, performance metrics have to be developed. As the device main function is to provide a hot shower to the users, these showers need to provide hot water to it's users at a temperature between a comfort temperature range, thus enabling the development of a comfort measurement for each shower that is taken. This measurement is tightly related to the amount of DHW that the device can produce, thus allowing to determine this amount using the data from each simulation.

On the other hand, this device is marketed as an alternative to gas boilers, being this a source of DWH. Therefore is imperative to measure the amount of LPG (Liquid Petroleum Gas) that is not being burned due to the utilization of this alternative. This encourages the utilization an additional measurement: average monthly energy savings. This last measurement can be interpreted not only as an energy measurement but also as a money saving measurement and even a CO<sub>2</sub> emissions reductions measurement.

### 3.3.1 Comfort measurement

For each shower, a 100% comfort should be achieved if the hot water is at a temperature inside the comfort temperature range, for the whole length of the shower. Then, the comfort measurement should decrease for every moment that the hot water temperature is not in the defined range. The comfort range considered is shown in Table 3.7. An exemplification of the comfort measurement value progression during a shower is shown in Figure 3.11, with the final comfort value reaching over 20%. This value does not change when the hot water temperature is within the defined upper and lower thresholds, when it's no longer inside said range, the perceived comfort of the shower decays linearly.

Table 3.7: Upper and lower temperature thresholds for comfort shower temperature range

Threshold	Temperature [°C]
Upper	41.5
Lower	35.5

### 3.3.2 Energy saving measurements

Each shower depletes the thermal storage tank from hot water and replenishes it with cold water from the intake. This process can be evaluated in terms of energy gain, as the integration of instantaneous difference of power entering and exiting the thermal storage tank, as formulated in the following Equation:

$$E = \int \dot{m}_{hot} \cdot h_{hot} - \dot{m}_{cold} \cdot h_{cold} \quad (3.8)$$

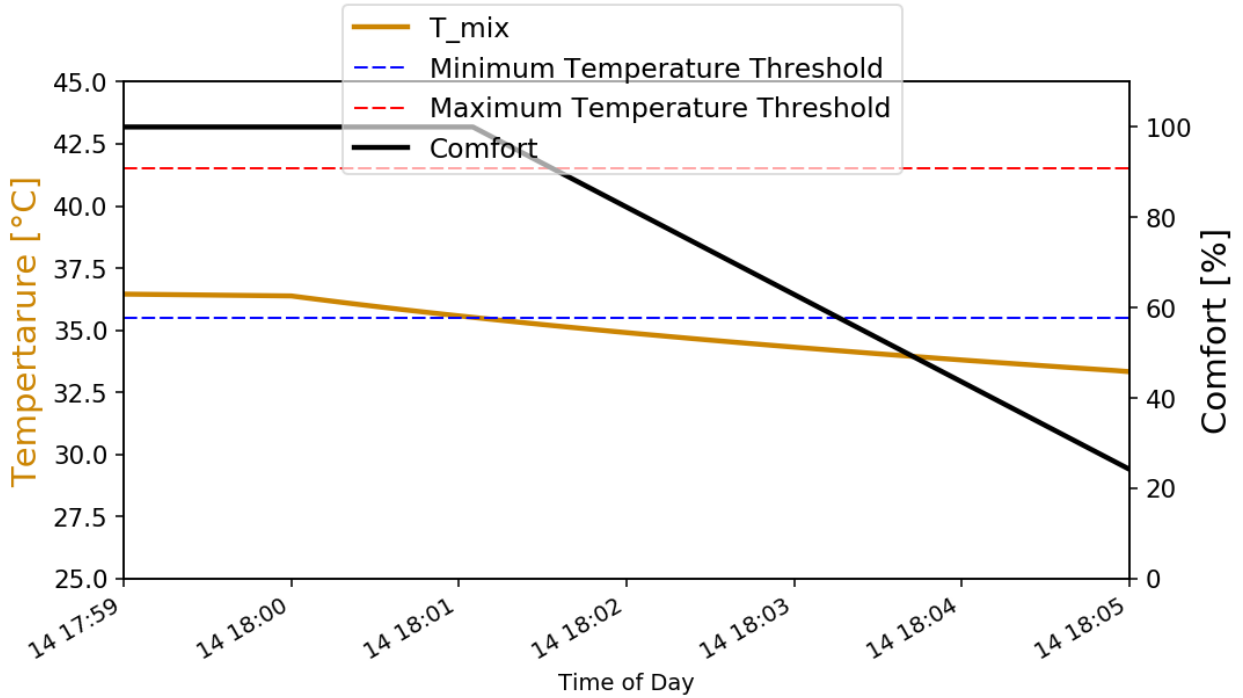


Figure 3.11: Evolution of comfort metric during a 5 minute shower

where  $\dot{m}_{hot}$  and  $\dot{m}_{cold}$  are the hot and cold water instantaneous mass flows, respectively, and  $h_{hot}$  and  $h_{cold}$  are the hot and cold water enthalpy, respectively.

The evolution of the energy gain, given the outlet and inlet temperatures and the instantaneous mass flows, is exemplified in Figure 3.12, where the gain of this shower is over 500[Wh].

### 3.4 Simulation of the validated model in different locations

Once an adequate candidate for the numerical model has been selected, simulations to evaluate the performance of the device in different locations in the continental national territory had been done. The list of locations considered, as well as their township administration name is listed in Table 3.8.

Every simulation is done considering a 150[W] PV system installed at a 30 [deg] tilt and 0 [deg] azimuth angle, nearby to the device's location, with a DHW demand of one 5-minute shower every two days, at a flow rate of 8 [L/min]. These water draws are specified to be done at 18:00 local time and draw a total volume of 40[L] from the system, whether is only hot water from the thermal storage or a mix between a local water source and water from the storage tank (using a thermostatic valve) to achieve comfortable temperatures.

At these conditions there's room for improvement, considering the tilt and azimuth angle

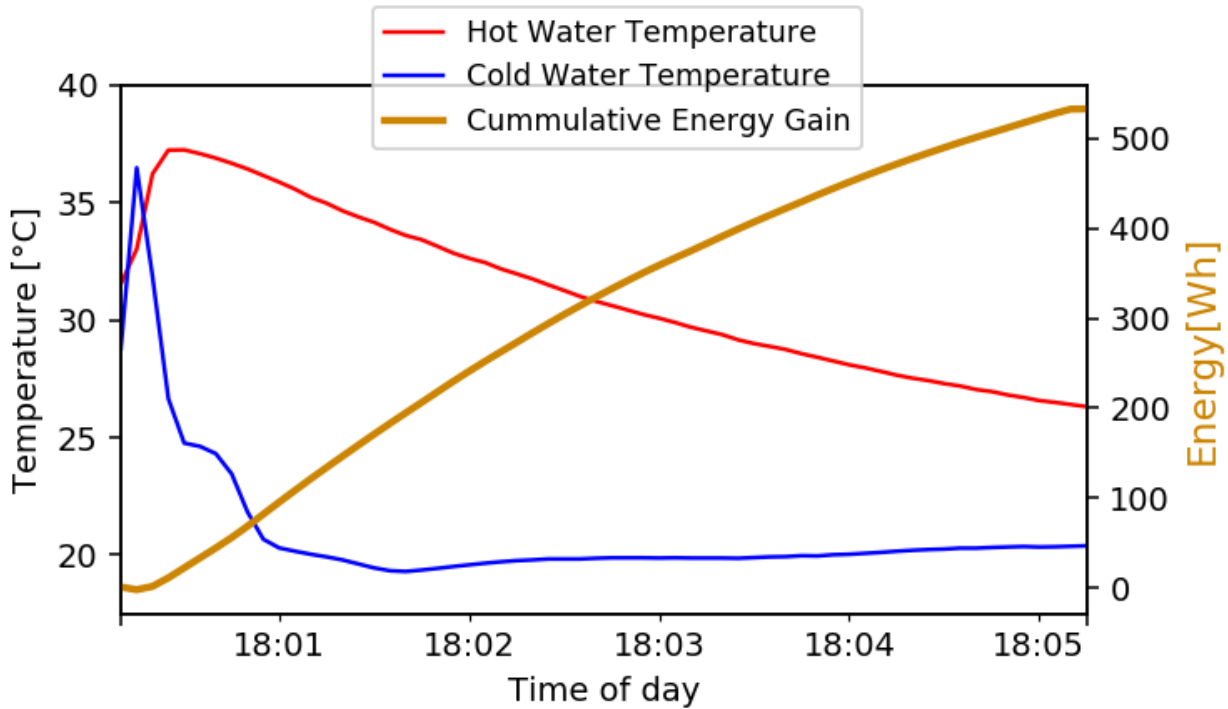


Figure 3.12: Evolution of energy gain metric during a 5 minute shower

of the PV system. Slight changes of these parameters may improve the simulated system performance.

Another assessment that has to be done is having the system simulated with a fixed ambient temperature, given that it would be most probably installed inside an enclosed area. Therefore, the validated model will be also simulated using fixed ambient temperatures for each season, as shown in Table 3.9, and the results will be directly compared to variable ambient temperature simulations.

The fixed temperatures considered for the simulation of the device in enclosed areas are below and above recommended household temperatures [30], and could underestimate or overestimate the system performance during hot and cold seasons, respectively.

### 3.4.1 Data sources

The data utilized to simulate and validate said simulation has been obtained from internal and external sources. Each process that uses or produces data is tabulated in Table 3.10, with it's corresponding input and output data set. The TMY acronym tag refers to data sets that have as a source a Typical Meteorological Year data base. This data is a set of meteorological data values for every hour in a year, for a given geographical location. The data are selected from data in a longer time period (normally 10 years or more). For each month in the year the data have been selected from the year that was considered most "typical" for that month. For instance, January might be from 2007, February from 2012 and so on.

Table 3.8: Locations simulated using the validated numerical model and associated geodesic data, ordered from the southernmost to the northernmost considered location.

Location	Township Administration	Latitude	Longitude	Altitude
Temuco	Temuco	-38.7359	-72.5904	120
Alto Bio Bío	Alto Bio Bío	-37.8807	-71.6394	517
Los Angeles	Los Angeles	-37.4629	-72.3612	139
Concepción	Concepción	-36.8201	-73.0444	24
Chillan	Chillan	-36.6063	-72.1023	130
Linares	Linares	-35.8464	-71.5996	163
Talca	Talca	-35.4232	-71.6485	108
Curico	Curico	-34.9780	-71.2529	205
Rancagua	Rancagua	-34.1701	-70.7406	511
Pirque	Pirque	-33.6875	-70.5884	671
Beauchef	Santiago	-33.4574	-70.6645	546
Lampa	Lampa	-33.2827	-70.8793	500
Colina	Colina	-33.2045	-70.6760	598
Polpaico	Tiltil	-33.1723	-70.8878	535
Los Andes	Los Andes	-32.8338	-70.5972	834
Los Molles	La Ligua	-32.2366	-71.5148	36
Illapel	Illapel	-31.6308	-71.1653	320
Ovalle	Ovalle	-30.6043	-71.1970	220
La Serena	La Serena	-29.9027	-71.2519	30
Vallenar	Vallenar	-28.5758	-70.7571	388
Copiapó	Copiapó	-27.3666	-70.3322	394
Antofagasta	Antofagasta	-23.6509	-70.3975	18
Calama	Calama	-22.4544	-68.9294	2265

Given that the experimental data and simulation data have a frequency of 1 minute, the TMY data has been processed and interpolated to be able to simulate the validated numerical model in a minute-by-minute basis. Also, the model requires an inlet water temperature, which is reported as a monthly average and is considered constant throughout the simulation of each month. Finally, the pre-defined water draw profiles are such that they simulate the hot water usage in different pre-set conditions.

The experimental data utilized to characterize, assess the performance of the device and validate the numerical simulations of the device are obtained from the test rig and a meteorological station placed at the same location of the test rig.

### 3.4.2 Performance Evaluation

Each simulated location is evaluated using the methodology explained in Section 3.3, for pre-defined periods of time. Yearly and seasonal performance evaluations are done to measure

Table 3.9: Seasonal fixed ambient temperatures considered for an enclosed area, used for the simulations of the device.

Season	Fixed Ambient Temperature Profile [ $^{\circ}C$ ]		
	A	B	C
Summer	21	22	24
Fall	18	18	21
Winter	15	14	18
Spring	18	18	21

the device’s delivered energy and it’s perceived comfort. Also, daily averages of solar energy for each simulated location are computed, using TMY data, for each season.

### 3.4.3 Data analysis

To obtain correlations between meteorological data and the device performance, seasonal average performance measurements are computed for each location. A scatter plot is generated and the analysed, classifying data points by season and using a standard linear regression methodology to search for a tendency. In these scatter plots the independent variable is the average daily solar radiation and the independent variables are the performance measurements mentioned in Section 3.3 and measurements from the simulated thermal storage tank. Hence, obtaining correlations should be possible. The linear regression shall have the shape shown in Equation 3.9, where  $y$  is the estimated indicator value for a certain location,  $x$  is the daily average solar radiation for the considered time frame,  $m$  is the inclination of the curve and  $n$  is the point of interception of the curve with the vertical axis.

$$y = m \cdot x + n \tag{3.9}$$

The linear regression methodology is applied separately for each season, sub-groups of the seasons and for all of them as a year, scatter plots are compared to the results of the regression analysis in the same plot.

## 3.5 Conclusions

The experimental tests carried during the investigation surpass the time frame contemplated in the Tests schedule (Tab. 3.3). Therefore, meteorological data of the extended time frame is also required to develop an accurate numerical model as well as analyse the behaviour of the device during this period.

The numerical model developed for the device has major simplifications that are purposefully implemented in the simulations of the device. These simplifications hinder the accuracy of the model if not optimized adequately by the methodology described in Section 3.2.3, but

Table 3.10: Data input and output of every data-related process of this Thesis work

<b>Process</b>	<b>Input Data</b>	<b>Output Data</b>
Device Tests	None	Experimental temperature profiles Instantaneous flow profiles
PV System Simulation	Irradiance Ambient Temperature Windspeed Geographical	PV System power output
Thermal Storage Tank Simulation	PV System power output Ambient Temperature Instantaneous flow profiles Experimental temperature profiles	Simulated temperature profiles System energy flows
Numerical Model Improvement and Validation	Experimental temperature profiles Simulated temperature profiles	Partial Curve Mapping values
Validated Model Simulation	Irradiance (TMY) Ambient temperature (TMY) Windspeed (TMY) Monthly average inlet water temperature Pre-defined water draw profiles	Simulated temperature profile Seasonal and annual performance measurements

significantly reduce the computation time of the yearly simulations that are done as well as the computation time for the optimization algorithm.

The developed performance measurements are necessary to assess the potential benefits regarding the device utilization. These measurements are based in experimentally and numerically available data.

The provided methodology enables the development of meaningful results for the present investigation and further analysis of the device performance in different meteorological conditions.

# Chapter 4

## Results

### 4.1 Experimental Results

Each day, data was acquired in the form of temperature profiles and instantaneous water flow profiles. The temperature profiles can be represented as seen in Figures 4.1 and 4.2, where the red line is the tank's outlet water temperature and the blue line is the tank's inlet water temperature. As shown in Table 3.3 there were water draws at different times of the day, with different time intervals; data was recorded for every water draw.

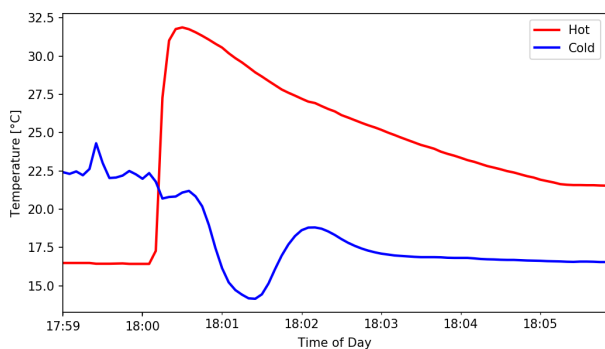


Figure 4.1: Hot and cold 5 minute water draw for a sunny day, at 18:00

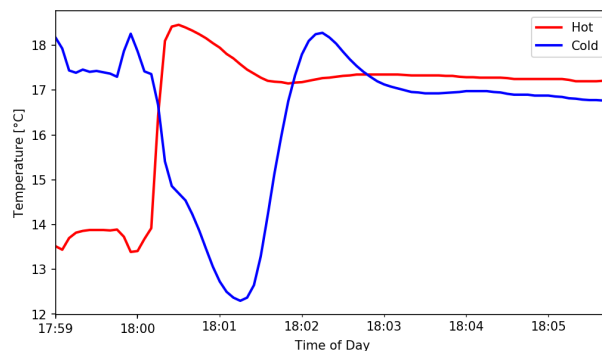


Figure 4.2: Hot and cold 5 minute water draw for a cloudy day, at 18:00

The data was recorded at a time interval that surpassed the time interval of actual the water draw for each day, to acquire every point of the discharge curve. Having the instantaneous water flow profiles, the relevant temperature data can be selected from the intervals in which water is flowing in and out of the thermal storage tank. Figure 4.3 shows the combined temperature profiles of all water discharges in a given time frame, with an instantaneous water flow greater than 0. This combination of temperature profiles and sub-groups of it are the ones used to optimize and validate the numerical model of the thermal storage tank.

Figure 4.1 shows that during a sunny day, the device has a higher maximum outlet water temperature compared to a cloudy day (Fig. 4.2). This suggests the possibility of an identifiable correlation between meteorological conditions and the device's yield.

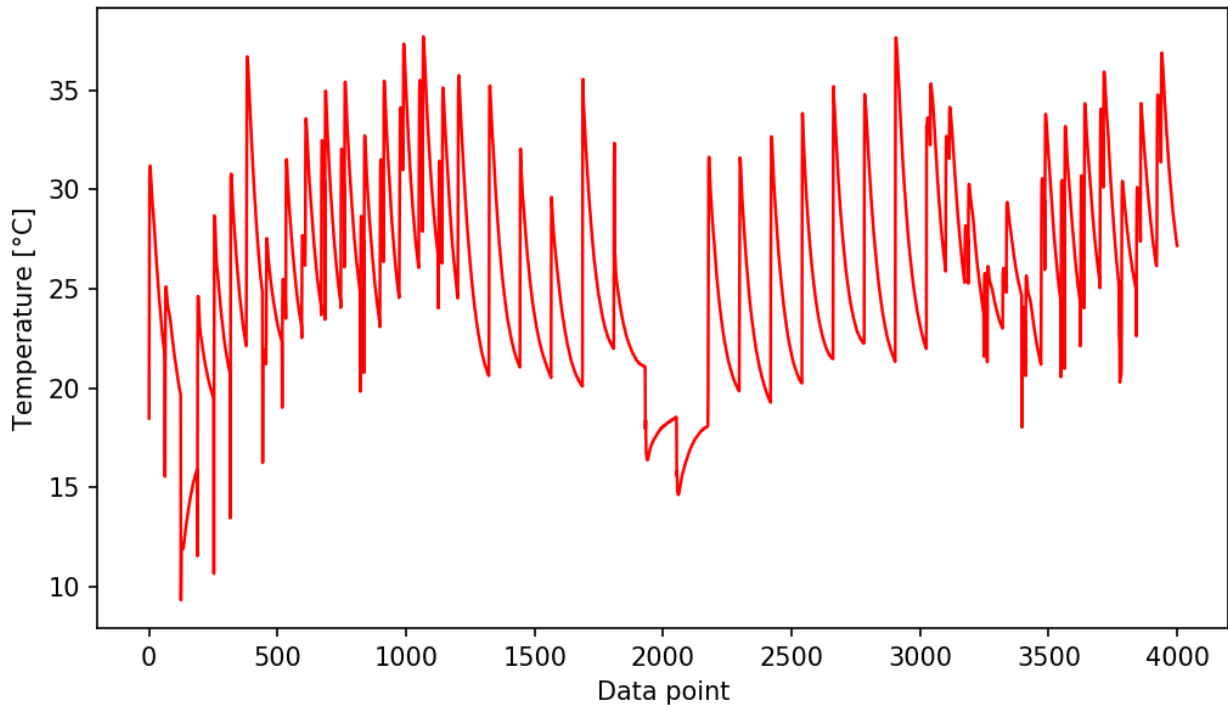


Figure 4.3: Hot water draw profiles from September 14<sup>th</sup>, 2019 to October 21<sup>st</sup>, 2019

Regarding the outlet temperature data (Fig 4.3) it can be seen that, for almost every water discharge of the tank, temperatures decreases up to  $20^{\circ}\text{C}$ . This indicates that the thermal storage tank of the device is most probably stratified during it's operation. The initial temperature for each water draw has been higher than  $35^{\circ}\text{C}$  and lower than  $15^{\circ}\text{C}$ . Having such low initial water temperature, even lower than the rest of the drawn water for a particular water discharge (Data point  $\approx 2000$ ), could mean that the tank cannot stratify accordingly when the working fluid is at low temperatures, compared to the rest of the discharges.

The fact that experimental results have been successfully taken and used for the development of this Thesis work is due to having a working test rig that has been built for that purpose.



## 4.2 Simulated Photovoltaic Array

The data acquired for PV simulation consist in a set of irradiance, ambient temperature and wind-speed curves. The obtained irradiance curves consists on a set of 3 variables that can change severely, depending on the meteorological conditions for the period the data was logged, as shown in Figures 3.5 and 3.6. It can be seen that during a cloudy day, the diffuse irradiance levels are greater than in a sunny day. Knowing the coordinates of the used PV array, the airmass and angle of incidence can be computed for any date of the year, as well as the irradiance curves, which then are used to determine the Plane of Array (PoA) irradiance components that radiates onto the PV array.

The calculated PoA components give as a result a global PoA irradiance, which is the total sum of said components. Figure 4.4 illustrates that there are two main components, direct and diffuse irradiance. The diffuse irradiance can be sub-divided as sky diffuse irradiance and ground diffuse irradiance. An environment with greater reflective properties, such as snowy surroundings, will have higher ground diffuse irradiance values than urban environments given the albedo the surroundings have. Given these values, ambient temperature and wind-speed readings, as well as the mounting type the PV array has, the temperature of the module and it's cells is estimated using Equations (2.11) and (2.12), respectively. It can be seen in Figure 4.5 that the temperature of the cells are slightly greater than the PV module and both can reach temperatures over  $60^{\circ}\text{C}$

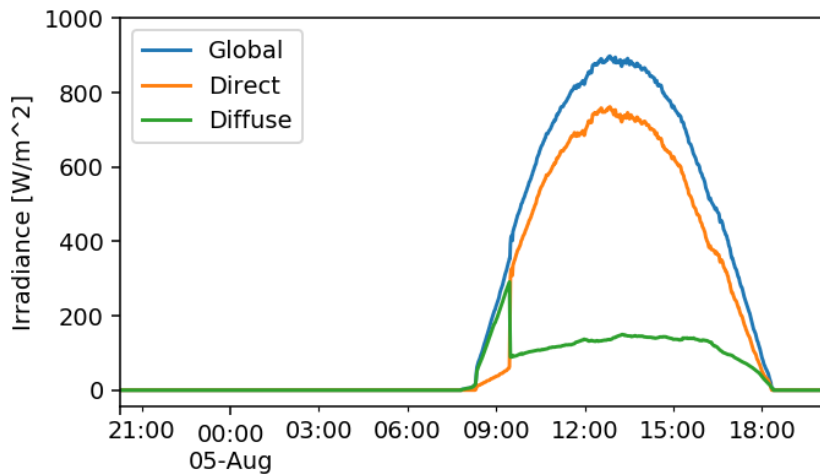


Figure 4.4: Plane of Array irradiance values for a sunny day.

All the values presented beforehand are used to determine the amount of instantaneous power that is being generated by the PV array. For this representative day, a PV panel with a nominal power of  $150[\text{W}]$  and a temperature power loss coefficient of  $0.45[\%/^{\circ}\text{C}]$  generates power according to what is shown in Figure 4.6, using Equation (2.13)

The temperature of the PV module and it's cells (Fig. 2.12) increases with the irradiance that the PV array is being exposed to. This raise in temperature will affect the performance of the power generated by the PV system (Fig. 4.6). This implies that there's a possibility that at higher irradiance levels, a PV system could have limitations related to it's power

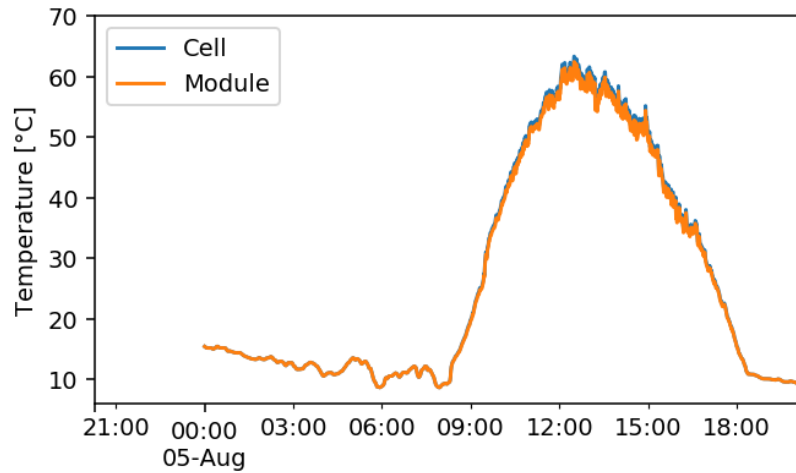


Figure 4.5: Temperatures of the PV module and it's cells during a sunny day.

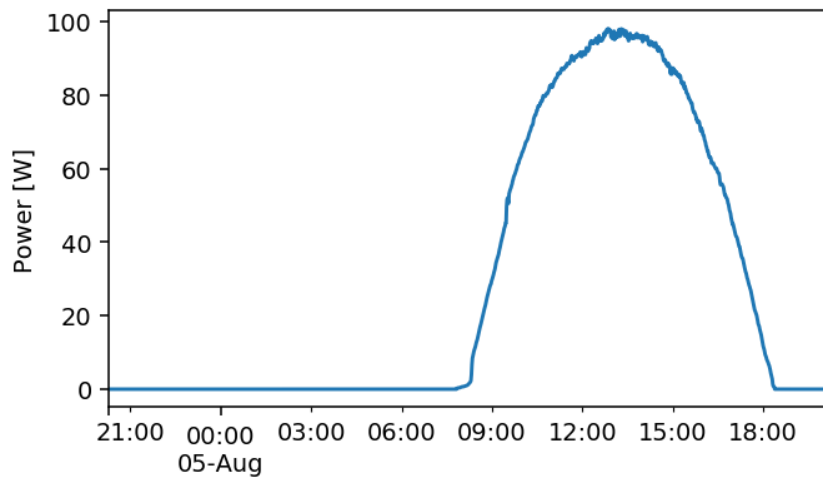


Figure 4.6: Simulated power generation for a 150W nominal power PV array, tilt and orientation as in Table 3.2

output. Having simulated the PV module temperature and it's cells temperature can be advantageous in relation to other PV system power output models numerical.

Given the high temperatures that the PV module and it's cells can reach, is necessary to warn about handling the PV panel during daylight. Touching this device with bare hands can result into severe burns if the temperatures are to high. Safety measures should be taken into account as well as planning any necessary handling to a more adequate time of the day, such as dusk or dawn.

As the amount of power generated depends highly on the PoA irradiance a PV system is receiving, this variable is to be maximized by adjusting the tilt and azimuth angle the PV panel is installed, for each location. Being that said, the simulations made at the configuration described in Table 3.2 are not at the optimal power generation configuration.

### 4.3 Numerical model improvement and validation

The improvement of the numerical model was based in the use of a Genetic Algorithm (GA) to match the experimental hot water draw curves to the simulated hot water draw profile, changing the values of two parameters that partake in the numerical model’s definition; heat loss coefficient and forced mix coefficient. A preliminary run (Figure 4.7) shows that the behaviour of the numerical model is similar to what has been recorded experimentally. Several runs of the algorithm were made, considering different time frames and data sets, making adequate changes into each individual attribute to improve the fitness of said individuals and generating 3 final candidates for all selected time frames. The minimizing parameters of each candidate are shown in Table 4.1.

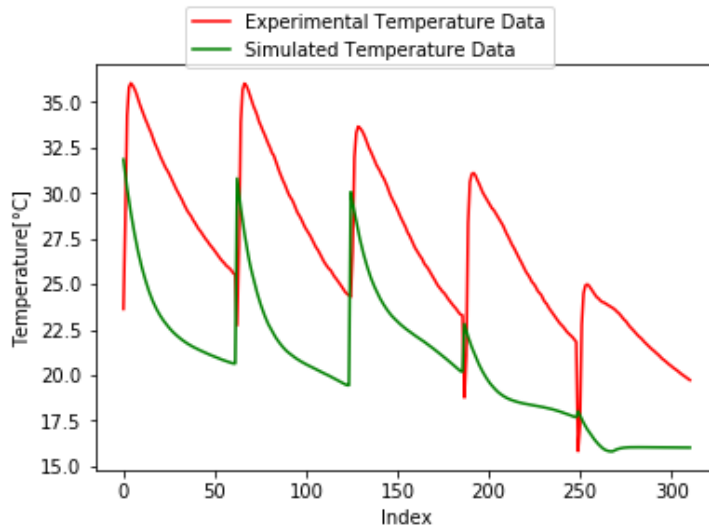


Figure 4.7: Simulated and experimental temperature profiles for a specific time frame and set of data points.

Table 4.1: Minimizing parameters for each obtained numerical model candidate for validation

Coefficient	Candidate	Experimental	1	2	3
	Heat Loss	Unknown	Unknown	0.174023	0.271511
Forced Mix	Unknown	Unknown	0.263843	0.414894	0.524400

For a set of more than 700 data points, the second candidate obtained through the GA optimization has the behaviour, compared to the original data, shown in Figure 4.8. The associated evolution of the fitness value of all the individuals considered for this candidate converges to a value below 60 for the objective function, being this the area between the curves computed using the PCM methodology. (Fig. 4.9).

The simulation of all available data points (Fig. 4.3) using the second candidate for an improved numerical model is shown in comparison to the experimental data in Figure 4.10, with complementary close-ups in Figures 4.11, 4.12, 4.13, 4.14 and 4.15. This simulation, and

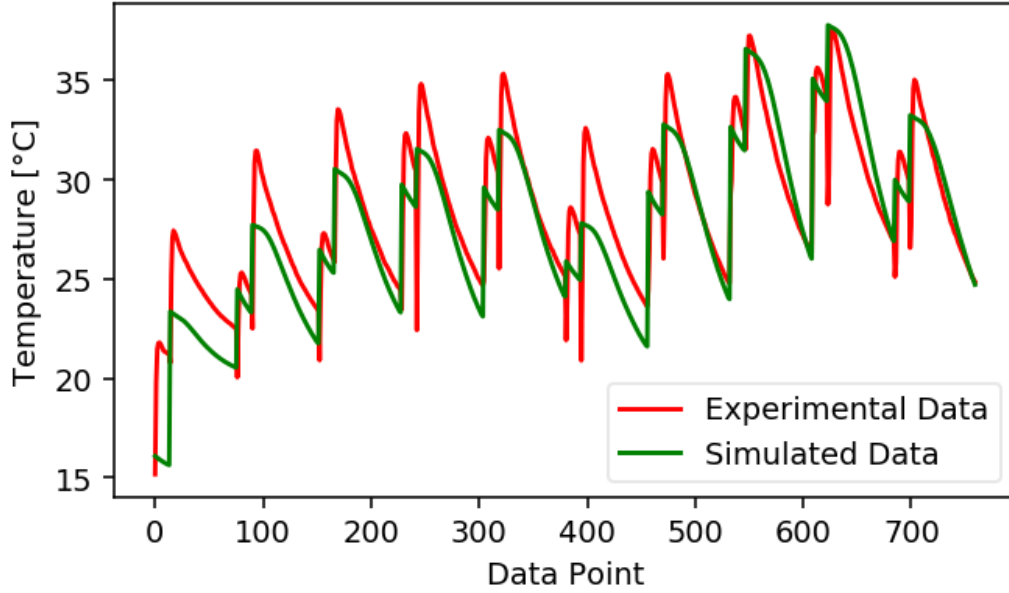


Figure 4.8: Simulated and experimental temperature profiles of a GA improved numerical model

it's equivalent for each candidate, have associated performance values, with relative error, shown in Table 4.2.

Table 4.2: Performance values and associated relative error for each candidate, compared to experimentally obtained values.

Value	Candidate			
	Experimental	1	2	3
Comfort [%]	1.404889	4.917112	3.315538	1.489182
Energy [kWh]	18.329945	19.776096	16.979463	12.680134
DWH Yield [L]	40.233000	138.514167	92.309167	40.179170
Relative Error	Candidate			
	Experimental	1	2	3
Comfort [%]		250	136	5.99997476
Energy [%]		7.889556263	7.367626234	30.82284753
DWH Yield [%]		244.2799857	129.4364493	0.13379564

For the second candidate of the improved numerical model (Fig 4.11 to 4.15 the experimental and simulated temperature profiles show that, although the simulated profile has the fsame general behaviour as the experimentally acquired profiles, there are data points where the numerical model temperature profile is higher (Fig 4.12) and lower (Fig 4.14 and 4.15) than the experimental data, as well as having a higher temperature difference from the beginning to the end of a water draw (Fig 4.12) than its experimental counterpart. The temperature drop for each water draw is sharper than its simulated counterpart, meaning that the numerical thermal storage model has a more pronounced stratification than the

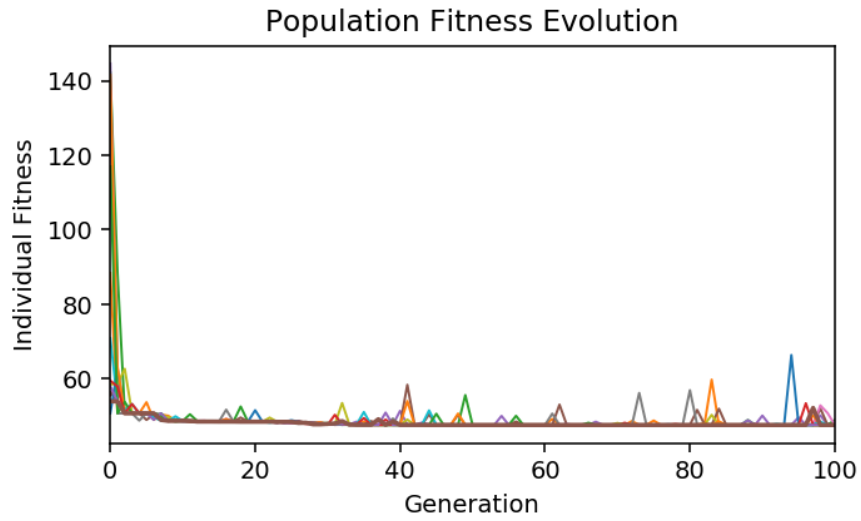


Figure 4.9: Evolution of the PCM value individuals for each generation.

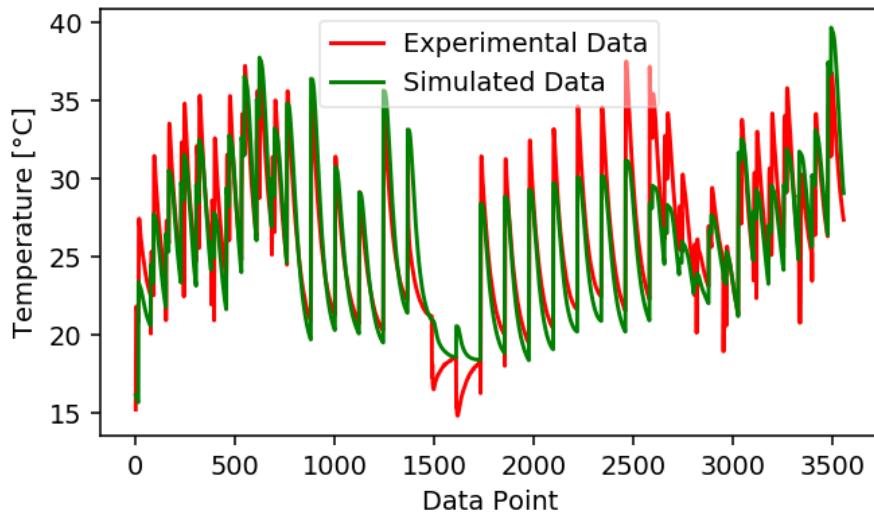


Figure 4.10: Experimental and simulated temperature profiles. Simulation performed using first iteration of improved numerical model

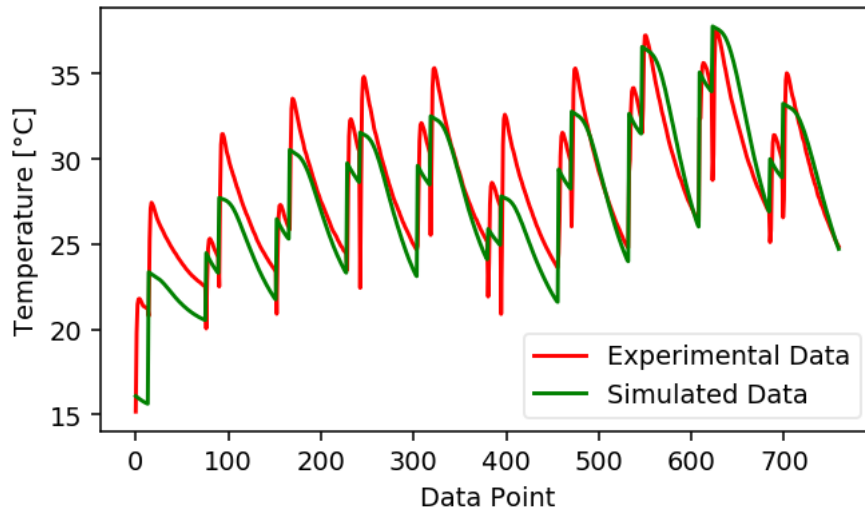


Figure 4.11: Experimental and simulated temperature profiles. Simulation performed using first iteration of improved numerical model (1/5)

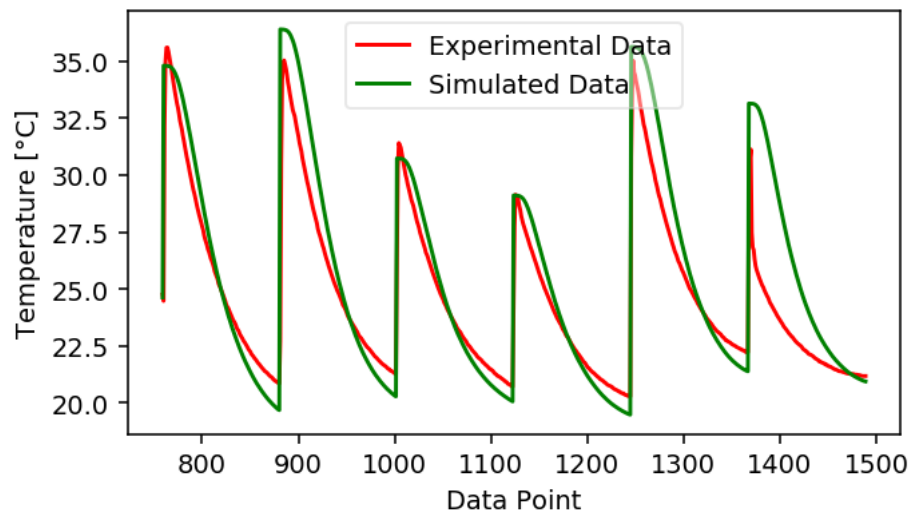


Figure 4.12: Experimental and simulated temperature profiles. Simulation performed using first iteration of improved numerical model (2/5)

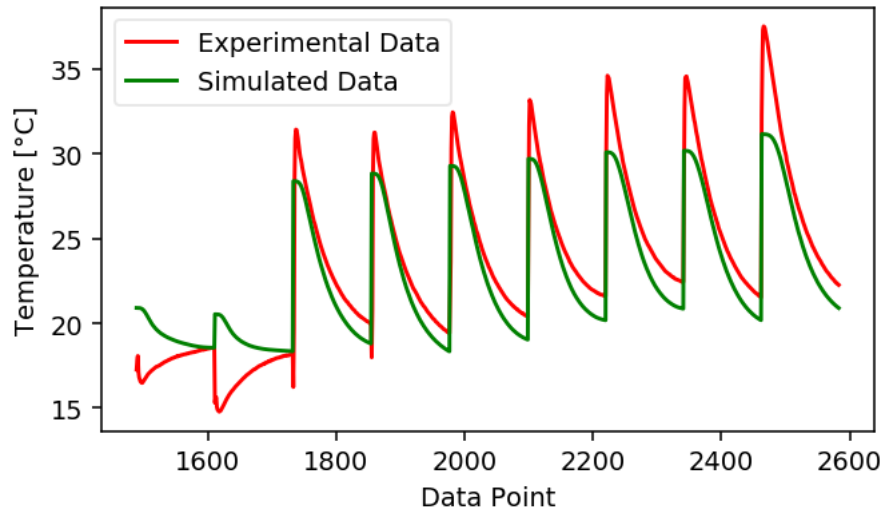


Figure 4.13: Experimental and simulated temperature profiles. Simulation performed using first iteration of improved numerical model (3/5)

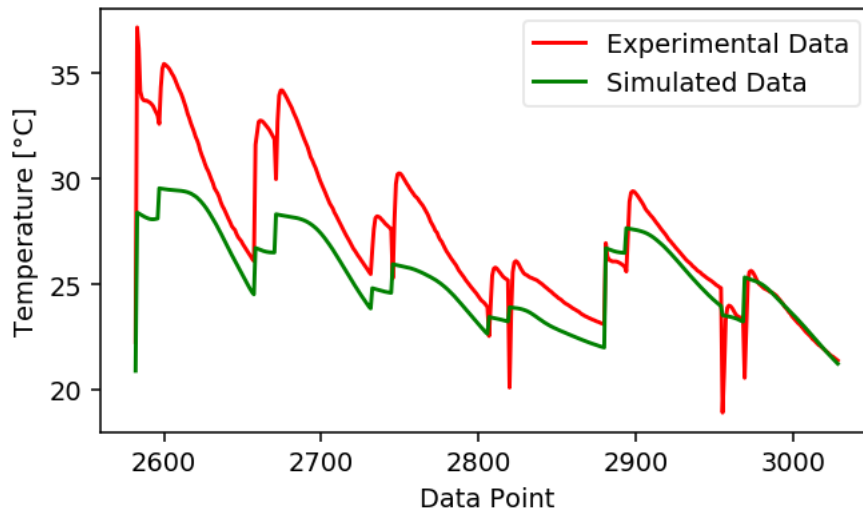


Figure 4.14: Experimental and simulated temperature profiles. Simulation performed using first iteration of improved numerical model (4/5)

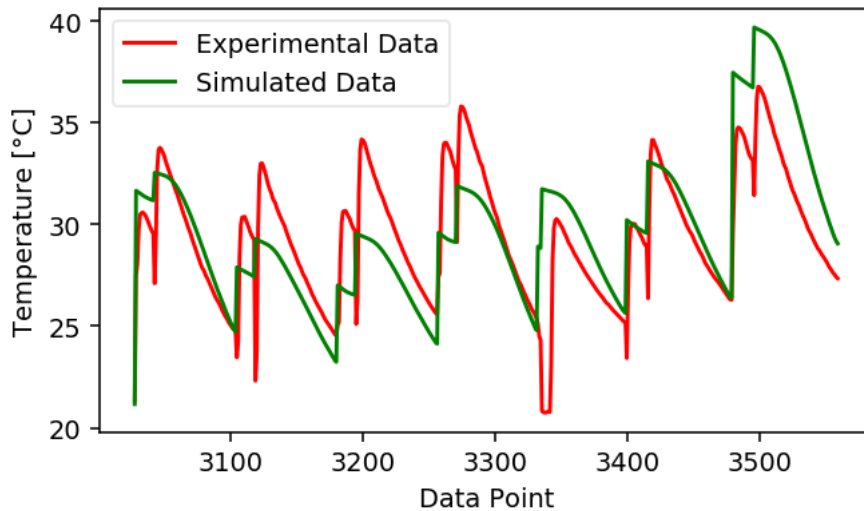


Figure 4.15: Experimental and simulated temperature profiles. Simulation performed using first iteration of improved numerical model (5/5)

actual device in the experiment. Also, the higher experimental temperatures (Fig 4.14 and 4.15) are most probably due to soiling differences between the actual experimental and the simulated PV system, where the PV panel is considered to have a thicker layer of soiling in the simulated model than in the PV panel test rig, given that the last one had been cleaned weekly throughout the experiment.

The performance measurements of both experimental and simulated water draws (Tab.4.2), compared one beside another shows that, for an energy generation difference not greater than 2 kWh ( $\approx 7.4\%$  relative error) in a span of 5 weeks, the measured comfort and DHW yield of the second candidate are more than 2 times greater than its experimental counterpart. Furthermore, the third candidate has the lowest relative error for the measured comfort as well as the DHW yield, but underestimates the energy generation with a relative error of more than 30%.

The results for the third candidate can be explained using Figure 4.13. The relative error in the energy generation is due to having a thermal storage that delivers water at a lower temperature for each draw, but sustaining the initial temperature for a brief period of time before decaying, instead of dropping instantly as the experimentally obtained profile suggests. This difference is enough to record an overall lower energy gain for the numerical model while delivering the same comfort and DWH yield measurements. Although the plotted data is from the second candidate, it can be assumed that the third candidate behaves similarly but at lower temperatures.

The selected parameters for the numerical model those obtained in the third candidate. This decision is due to having the lowest relative error (Tab. 4.2) in the determination of the DHW yield of the system, being consistent with the main objective of this Thesis.



## 4.4 Simulated locations

In this section, results of the simulated storage tank of both variable ambient temperature and fixed ambient temperature, are shown in comparison to each other.

### 4.4.1 Maximum Daily Temperature

Maximum daily temperatures reached inside the thermal storage tank among all the simulated locations are shown in Figure 4.16, for variable and fixed ambient temperatures simulations. Also, scatter plots of yearly average daily solar radiation and yearly average maximum daily temperature reached inside the tank are shown in Figure 4.17, for variable and fixed ambient temperatures simulations, considering all the locations. The Linear Regression (LR) parameters for these scatter plots are listed in Table 4.3.

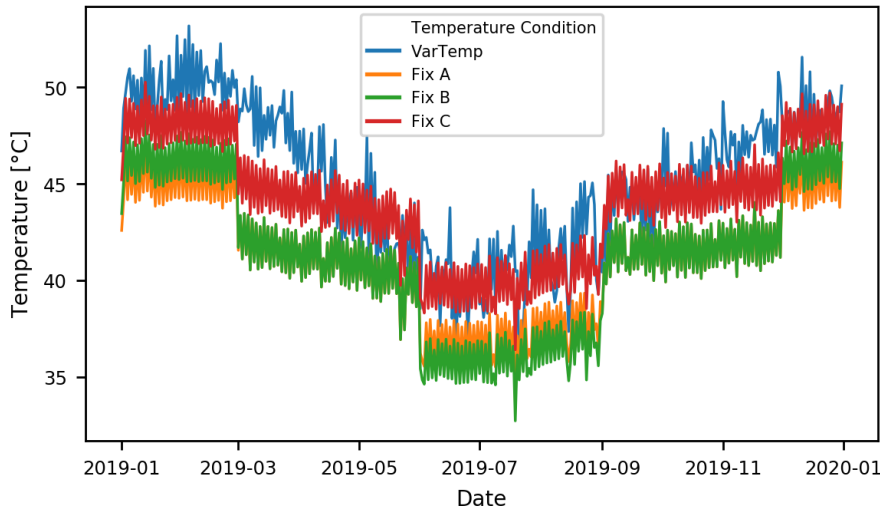


Figure 4.16: Maximum daily temperature reached inside the thermal storage tank, among all the locations, for variable and fixed ambient temperature simulations

Table 4.3: Linear Regression parameters for fixed and variable ambient temperature for daily solar radiation vs. maximum daily temperature.

Temperature Condition	m	n	R <sup>2</sup>
Variable	4.4394	10.683	0.7926
Fixed A	2.3209	22.913	0.9731
Fixed B	2.3196	22.925	0.9731
Fixed C	2.3203	25.687	0.9733

The line plot for the daily maximum temperatures reached by the thermal storage tank numerical model, among all simulated locations and temperature conditions (Fig 4.16), shows that the high temperature peaks for summer season and winter season can differ in more than

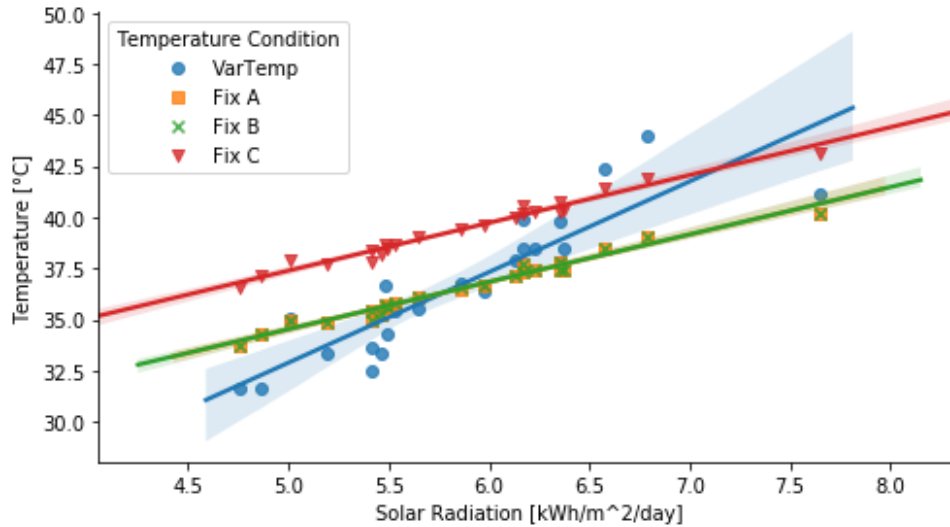


Figure 4.17: Scatter plot of yearly average daily solar radiation and maximum daily temperature reached inside the thermal storage tank, among all the locations, for variable and fixed ambient temperature simulations

10 [°C] for both variable ambient temperature (VAT) and fixed ambient temperature (FAT) simulations. Also, it can be seen in the FAT line plots that abrupt changes in ambient temperatures (Fig. 3.9) incite abrupt changes in maximum daily temperatures achieved. This implies that the maximum temperatures achievable by the thermal storage tank, as well as the overall performance of the device, highly depends in the ambient temperatures where the tank is located.

A high dependability of ambient temperature is expected due to the nature of the THP heat source, having its COP affected by the temperature difference between the hot and cold side. Lower ambient temperatures can increase this temperature difference, thus reducing the COP and having less heat introduced into the thermal storage. This lack of heating power probably lowers the maximum temperature achievable by the device, as suggested in Figure 4.16 for FAT line plot.

Maximum temperatures reached (Fig 4.16) are not greater than 55 [°C] and not lower than 35 [°C] for the VAT conditions. On the other hand, for FAT conditions, reached maximum temperatures are not greater than 50 [°C] and lower than 35 [°C] (except for a single day). According to Table 4.4, water at the highest temperature reached, for VAT conditions, can produce third degree burns if exposed to them for approximately one minute. It can be assumed that, under normal circumstances, the user would be able to avoid contact after a few seconds of exposure.

Regarding average maximum temperatures achieved by the thermal storage tank throughout the year and the average daily solar radiation of the corresponding location (Fig 4.17), it can be noticed that for both VAT and FAT conditions, and solar radiation values between 5 and 6.0 [kWh/m<sup>2</sup>/day], maximum temperatures adjust to all the linear regressions acceptably, whereas the values further from the said range significantly diverge from the estimation in the case of VAT conditions. It is safe to propose that at higher average daily solar radi-

Table 4.4: Scalding Hazard Table. Source: American Burn Association

Water Temperature	Exposure time for a third degree burn
68 °C	1 second
64 °C	2 seconds
60 °C	5 seconds
56 °C	15 seconds
52 °C	1 minute
51 °C	3 minutes
48 °C	5 minutes
37 °C	safe temperature for bathing

ation values, a higher average maximum temperature can be reached, with few exceptions. Also, the inclination difference between VAT and FAT conditions linear regression suggests the possibility of an influence of the ambient temperature onto the device performance.

#### 4.4.2 Performance Measurements

Density plots are developed for each performance measurement under each ambient temperature condition. The dependent variable is local daily solar radiation averages and the dependent variable is the performance measurement of all locations, for each season.

#### Comfort

The density plots for comfort performance measurement are shown in Figures 4.18, 4.19, 4.20 and 4.21 with seasonal labeling for each point. For yearly comfort average values, the scatter plots for each ambient temperature condition and their respective linear regression are shown in Figures 4.22. The LR parameters for all these plots are listed in Table 4.5.

Table 4.5: Linear Regression parameters for comfort scatter plots.

Ambient Temperature Condition	m	n	R <sup>2</sup>
Variable	14.664	-47.429	0.6346
Fixed A	6.8074	-9.8310	0.7656
Fixed B	6.3490	-6.1618	0.7242
Fixed C	9.7428	-13.374	0.8478

Overall results for VAT conditions, plotted in Figure 4.18, show that in Summer the comfort levels accumulate approximately at a value of 80%, within a range of 40% to 90%. On the other hand, for FAT A and B conditions (Figs.4.19 and 4.20), having a fixed ambient temperature of 21 [°C] and 22 [°C] 3.9) allows the system to reach comfort levels accumulated approximately at 70%, within a range of 50% to 80%, smaller range than for VAT conditions.

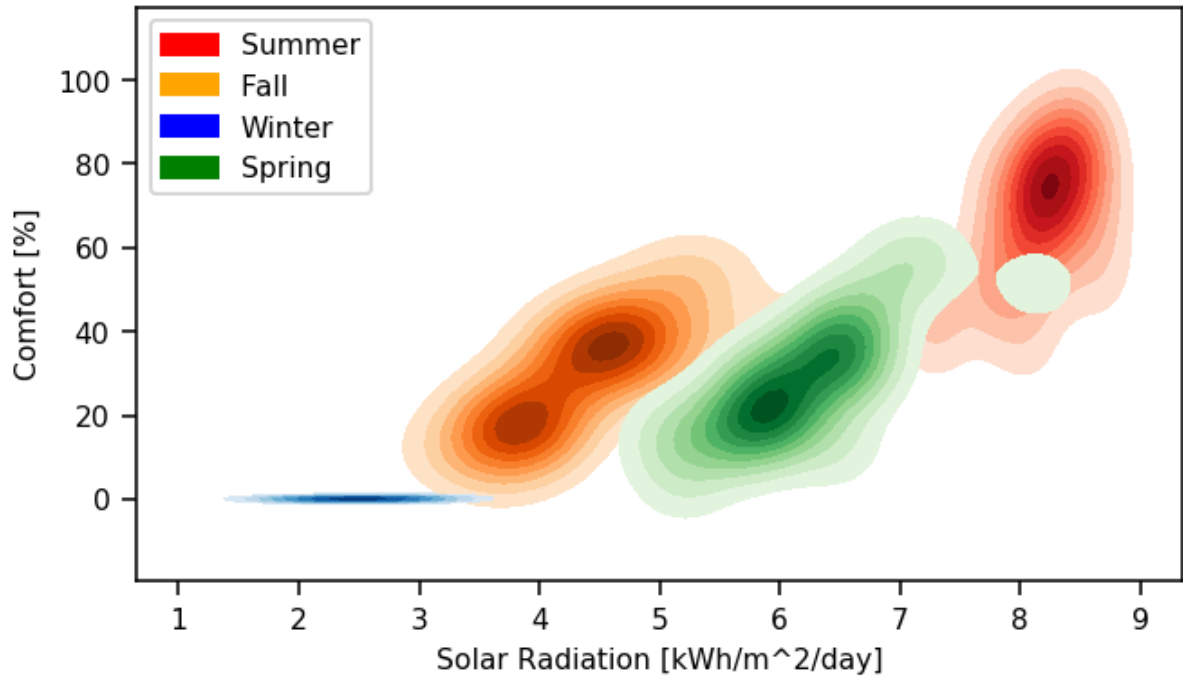


Figure 4.18: Density plot for comfort measurements considering variable ambient temperature throughout the year.

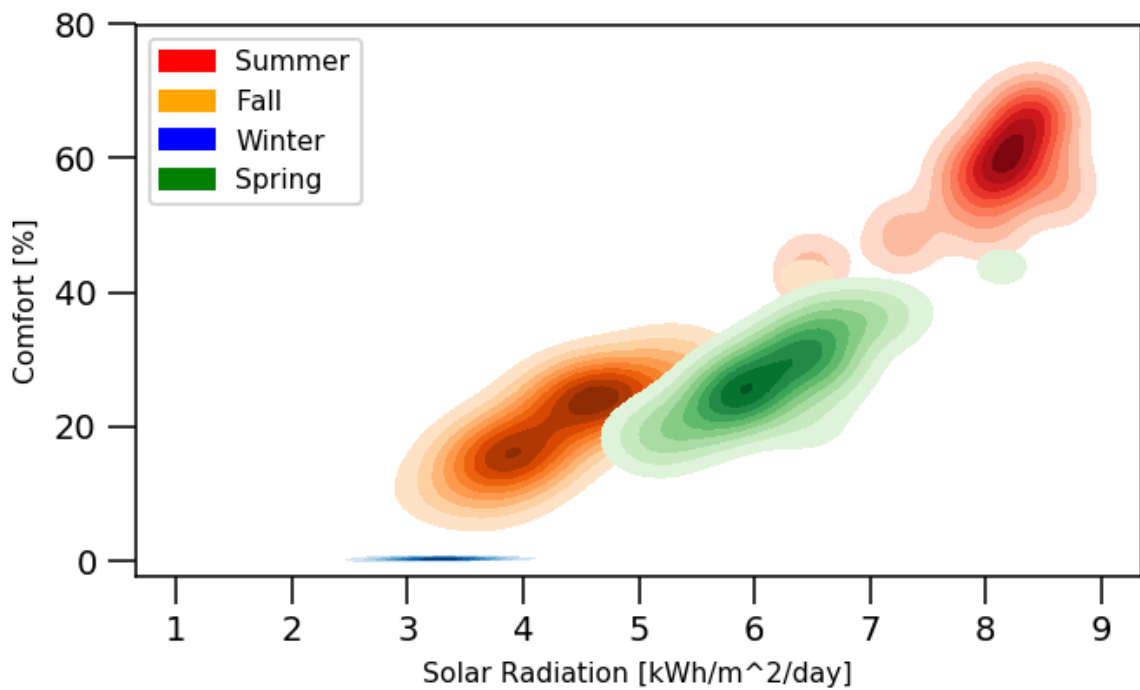


Figure 4.19: Density plot for comfort measurements considering fixed ambient temperatures (A) throughout the year.

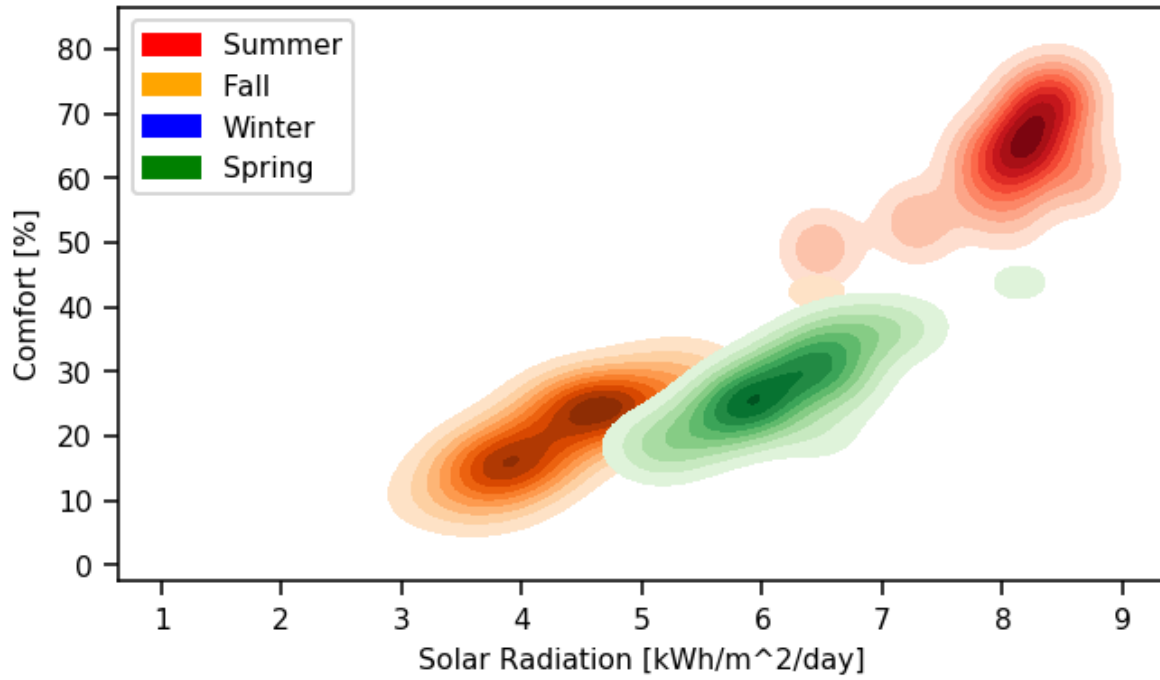


Figure 4.20: Density plot for comfort measurements considering fixed ambient temperatures (B) throughout the year.

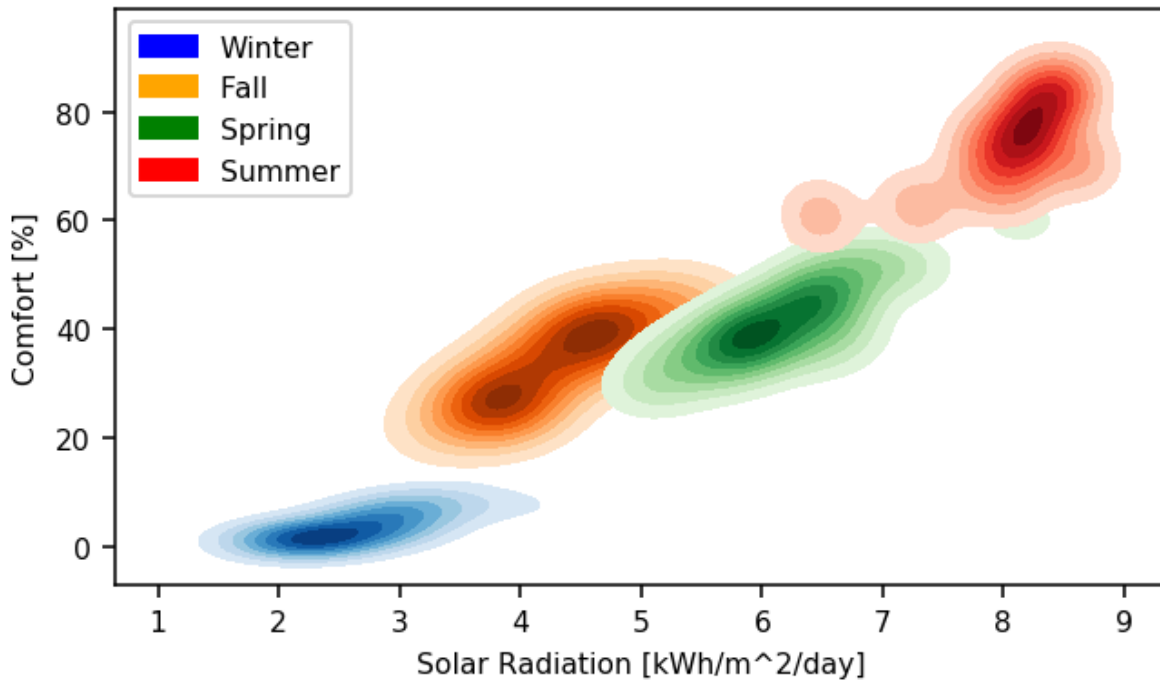


Figure 4.21: Density plot for comfort measurements considering fixed ambient temperatures (C) throughout the year.

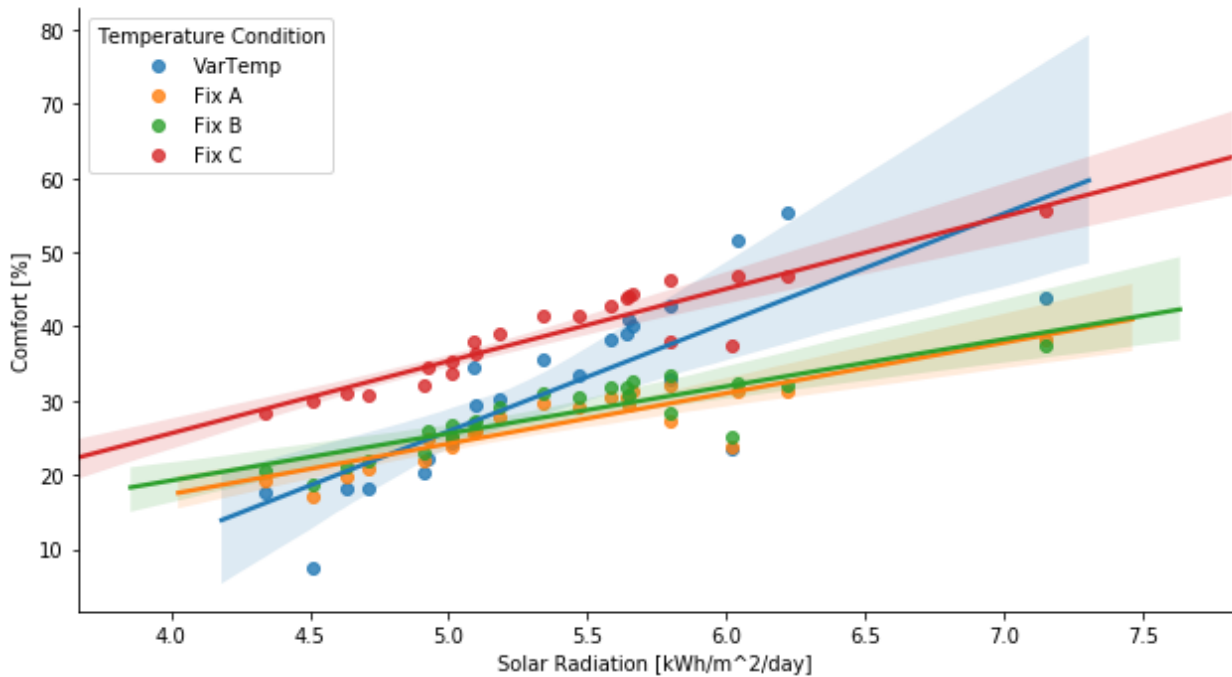


Figure 4.22: Scatter plots for yearly average daily solar radiation and average comfort, with linear regression curves.

Higher ambient temperatures (Fig. 4.21) allow greater comfort levels to be reached for fixed ambient temperature conditions. This suggests that having the device installed in an enclosed area could enable a more precise seasonal performance estimation. For VAT conditions and locations that have solar radiation levels lower than 3 [kWh/m<sup>2</sup>/day], in Winter, the device is unable to provide showers with comfortable temperatures. The same happens for FAT (A and B) conditions and locations with solar radiation levels lower than 4 [kWh/m<sup>2</sup>/day], in Winter. For FAT C conditions, the fixed ambient temperature of 18 [°C] during Winter allows showers with comfort levels marginally above 0%. This phenomena could be due to having low ambient temperatures, both for VAT and FAT conditions, and an already suggested ambient temperature influence onto the device performance. In fact, at the same solar radiation levels, Fall comfort levels are not null for VAT and FAT conditions, reinforcing the possibility of ambient temperature influence onto the device performance. Therefore, additionally to the solar radiation needed to power up the device, this device should be installed in locations with average ambient temperatures above 18 [°C] during Winter, for shower comfort purposes.

Figure 4.22 shows that expected comfort levels are lower for FAT (A and B) conditions in locations with yearly average daily solar radiation levels over  $\approx 5$  [kWh/m<sup>2</sup>/day]. This could be due reducing the average temperature the device is exposed to throughout the day, if it were to be installed outside. Then, the linear correlation of yearly and seasonal (not considering winter) comfort levels, for FAT conditions, could be used as a minimum expected comfort level estimator, in locations with yearly average daily solar radiation levels over 5 [kWh/m<sup>2</sup>/day]. For FAT (C) conditions, the average comfort levels reached in each location is greater than for VAT conditions. Therefore, the linear correlations proposed can be utilized as a lower (A and B) and an upper (C) limit estimation for expected annual comfort levels.

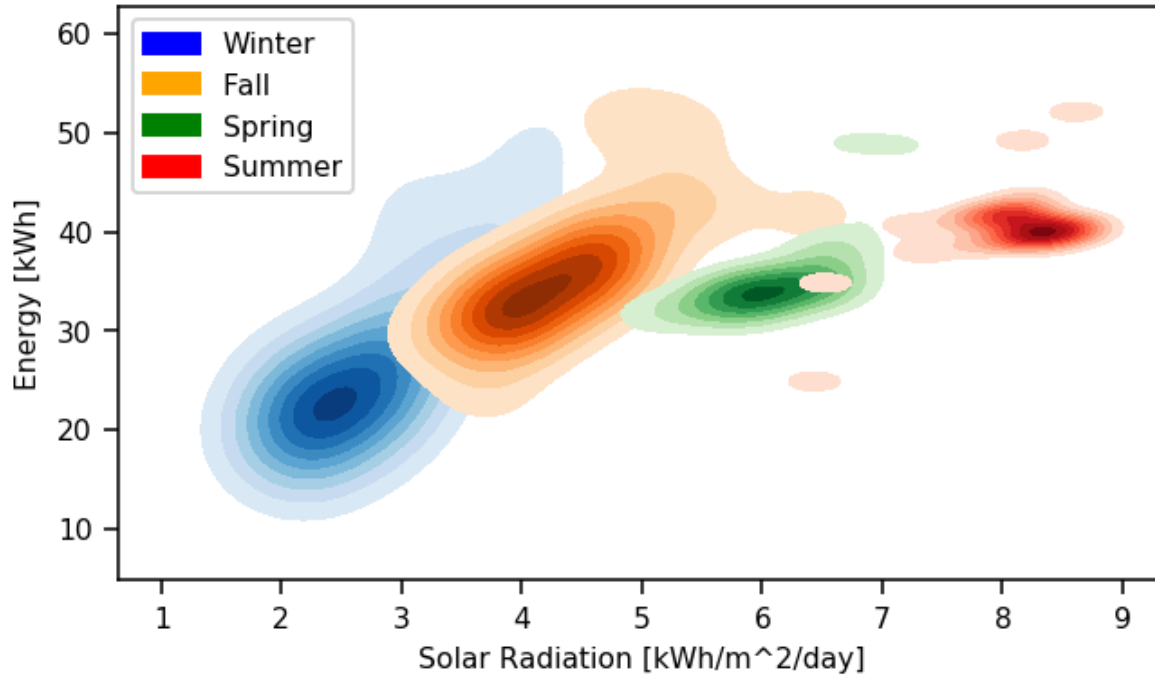


Figure 4.23: Density plot for energy measurements considering variable ambient temperatures throughout the year.

### Accumulated Energy

The density plots for accumulated energy performance measurement are shown in Figures 4.23, 4.24, 4.25 and 4.26, with seasonal labeling for each point. For yearly accumulated energy values, the scatter plots for each ambient temperature condition and their respective linear regression are shown in Figures 4.27. The LR parameters for this plot are listed in Table 4.6.

Table 4.6: Linear Regression parameters for accumulated energy scatter plot.

Ambient Temperature Condition	m	n	R <sup>2</sup>
Variable	28.4470	-13.228	0.5797
Fixed A	16.6965	52.214	0.3931
Fixed B	16.6487	51.812	0.3912
Fixed C	15.8062	72.038	0.3625

All of VAT and FAT conditions seasonal accumulated energy density plots (Figs. 4.23, 4.24, 4.25 and 4.26) show that at higher solar radiation levels, the device is able to accumulate higher amounts of energy throughout the season. For yearly energy accumulation, there is not a clear linear correlation between the solar radiation levels and the amount of energy the device can accumulate. This is most probably due to the different inlet temperatures the device has for each location. Given that the accumulated energy is dependent of the inlet temperature (Eq. (3.8)) and that the inlet temperature is possibly not directly related

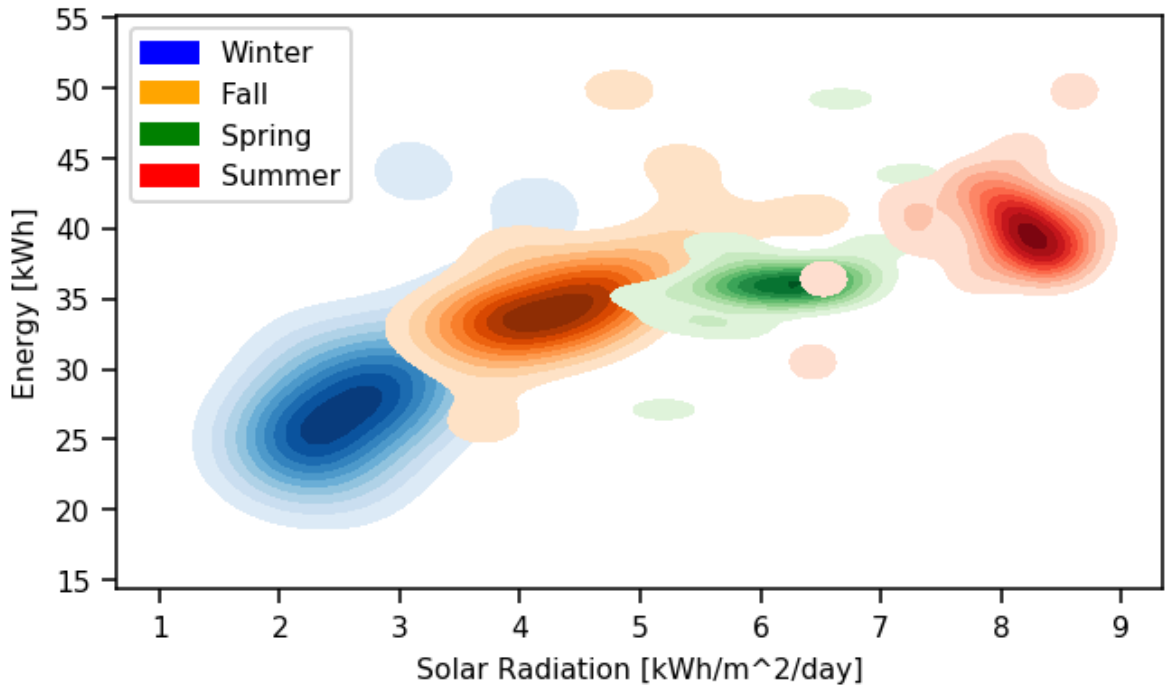


Figure 4.24: Density plot for energy measurements considering fixed ambient temperatures (A) throughout the year.

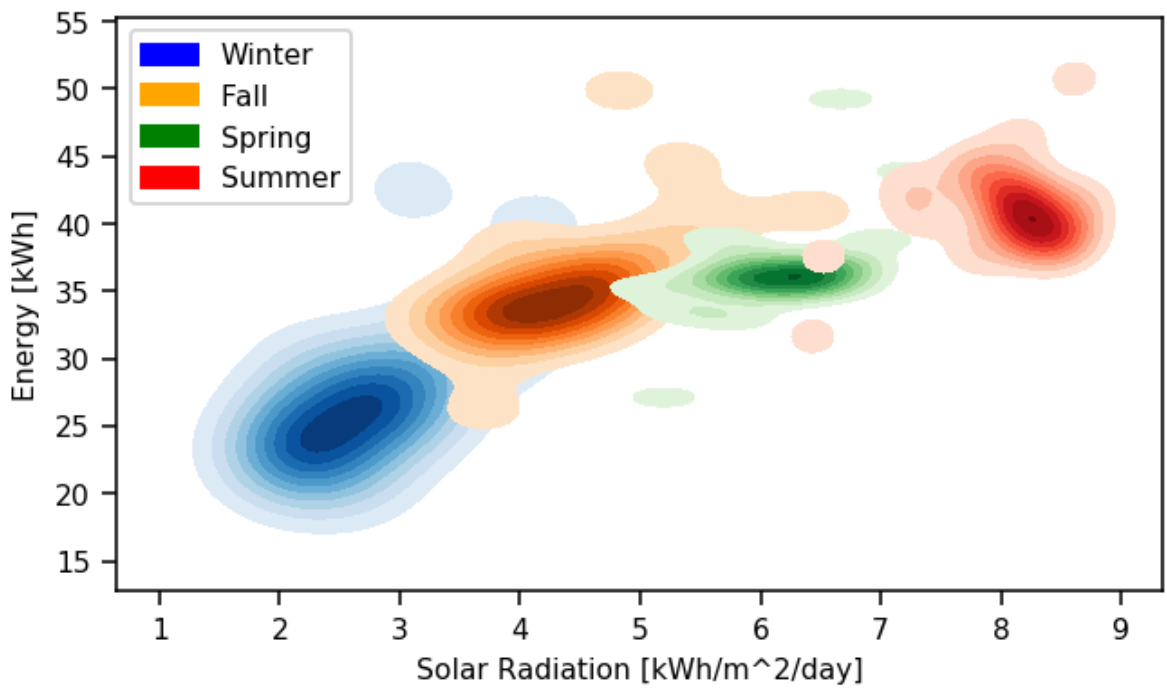


Figure 4.25: Density plot for energy measurements considering fixed ambient temperatures (B) throughout the year.



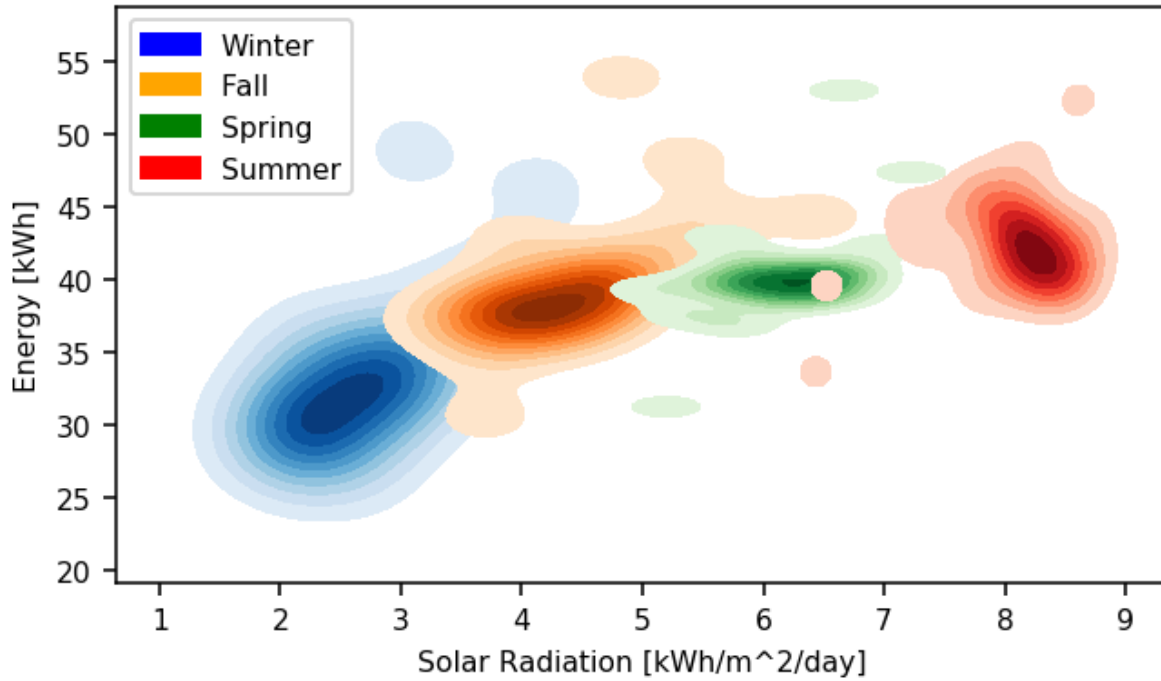


Figure 4.26: Density plot for energy measurements considering fixed ambient temperatures (C) throughout the year.

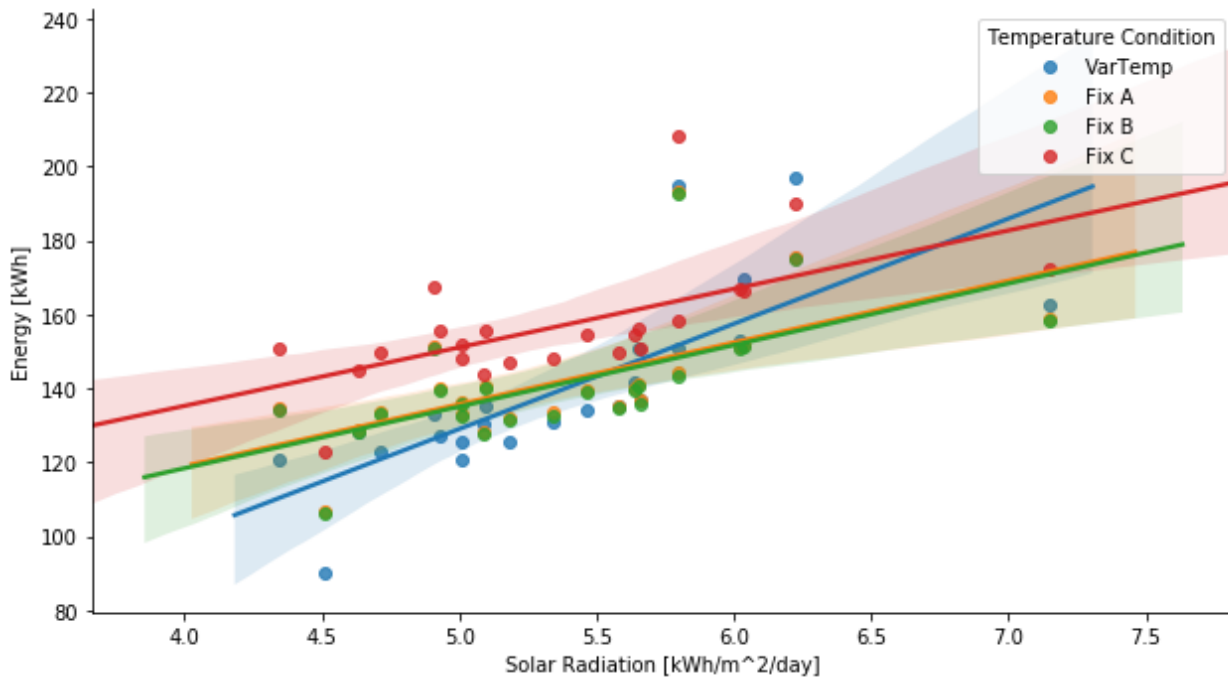


Figure 4.27: Scatter plots for yearly average daily solar radiation and accumulated energy, with linear regression curves.

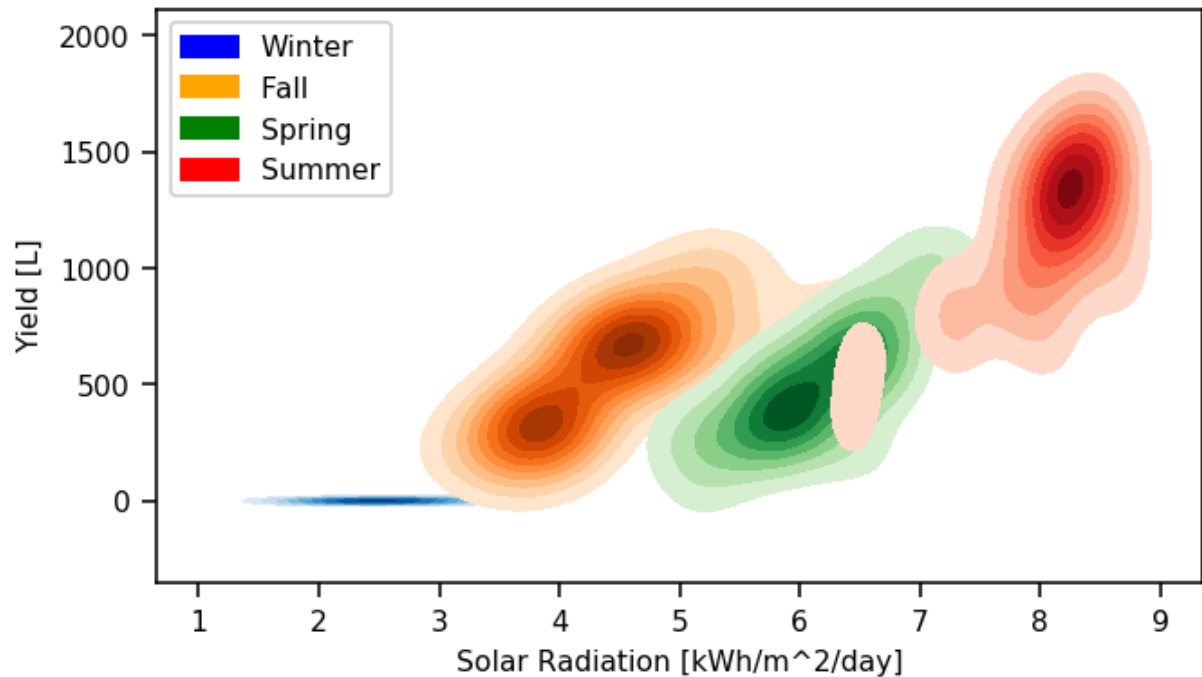


Figure 4.28: Density plot for DHW yield measurements considering variable ambient temperatures throughout the year.

to the amount of solar radiation a location is receiving on a daily basis, this performance measurement can have several values for the same solar radiation levels.

Yearly LR of all FAT and VAT conditions for accumulated energy (Fig 4.27) have an R-squared value lower than 0.6, respectively. Whereas for seasonal LR only the VAT condition LR for cold season could be considered a valid correlation. This leads to mostly disregard the use of this LRs as valid estimators for the amount of energy that the device can accumulate. Therefore, a complete simulation of the system under specific draw conditions is recommendable, to determine the amount of energy device can accumulate, above the use of any correlation.

### Accumulated DHW Yield

The scatter plots for accumulated energy performance measurement are shown in Figures 4.28, 4.29, 4.30 and 4.31, with seasonal labeling for each point. For yearly accumulated energy values, the scatter plots for each ambient temperature condition and their respective linear regression are shown in Figures 4.32. The LR parameters for this plot are listed in Table 4.7.

Overall results for VAT and FAT conditions, plotted in Figure 4.28, 4.29, 4.30 and 4.31, show that at higher solar radiation levels the device will have higher DWH yields. During Summer, the accumulated DHW generated for the simulated locations under VAT conditions are around the 1450[L] value, within a range from 750[L] to 1750[L] of DHW. This can be

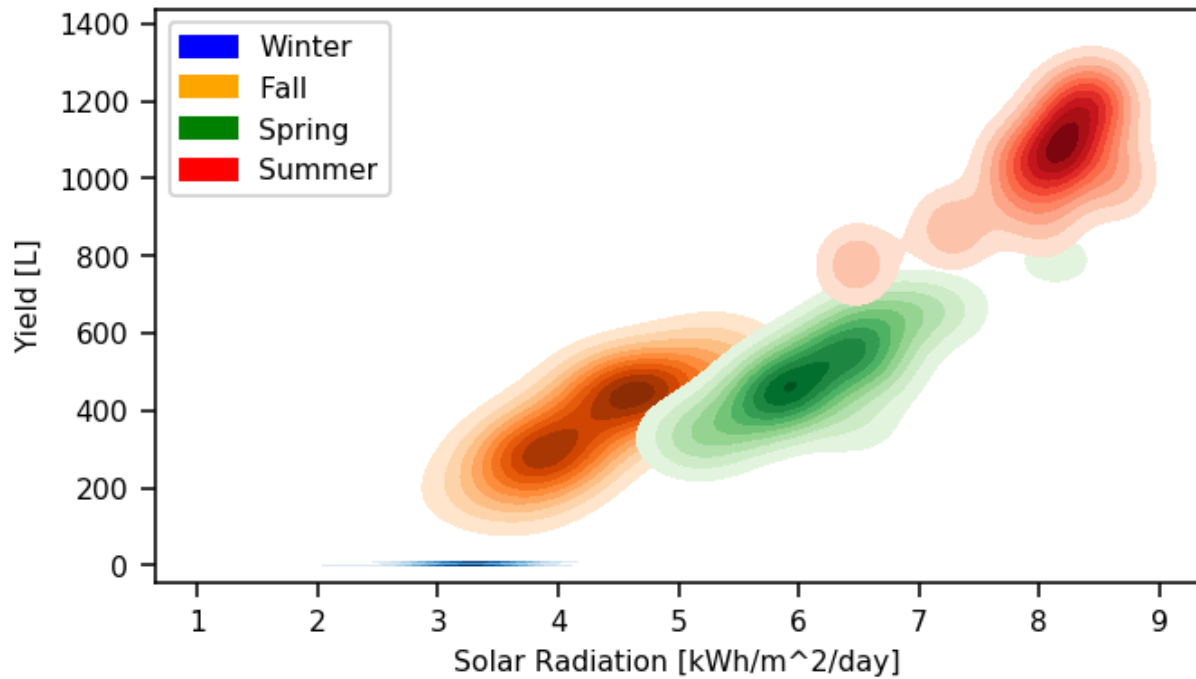


Figure 4.29: Density plot for DHW yield measurements considering fixed ambient temperatures (A) throughout the year.

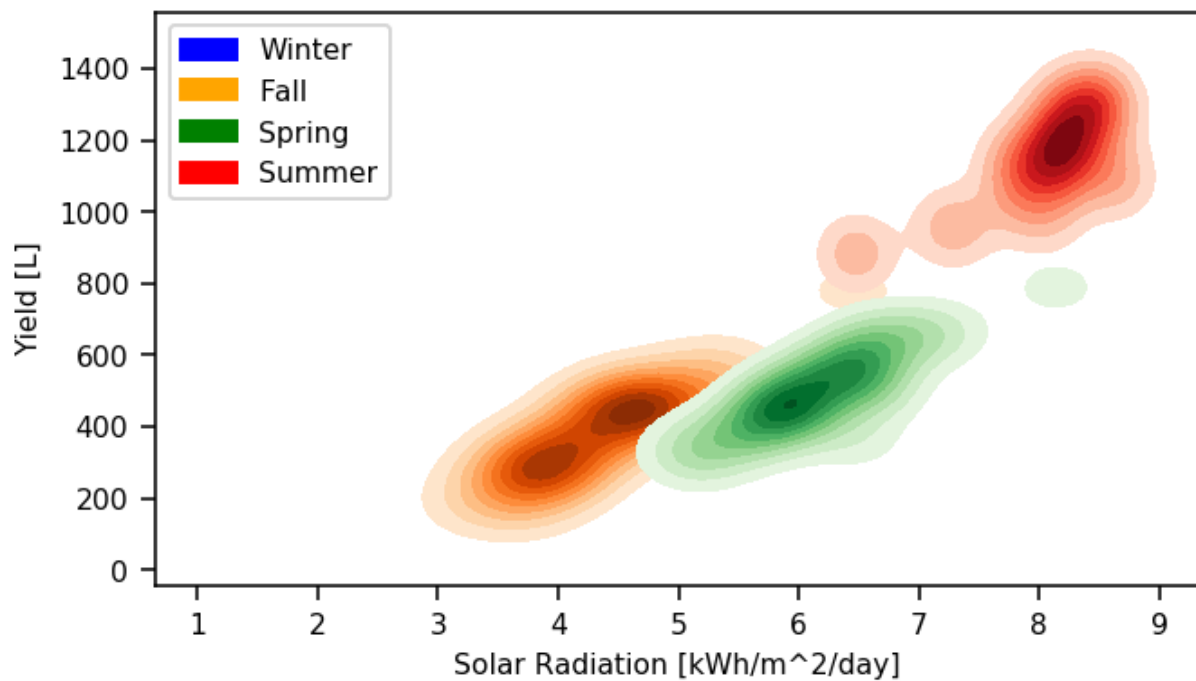


Figure 4.30: Density plot for DHW yield measurements considering fixed ambient temperatures (B) throughout the year.

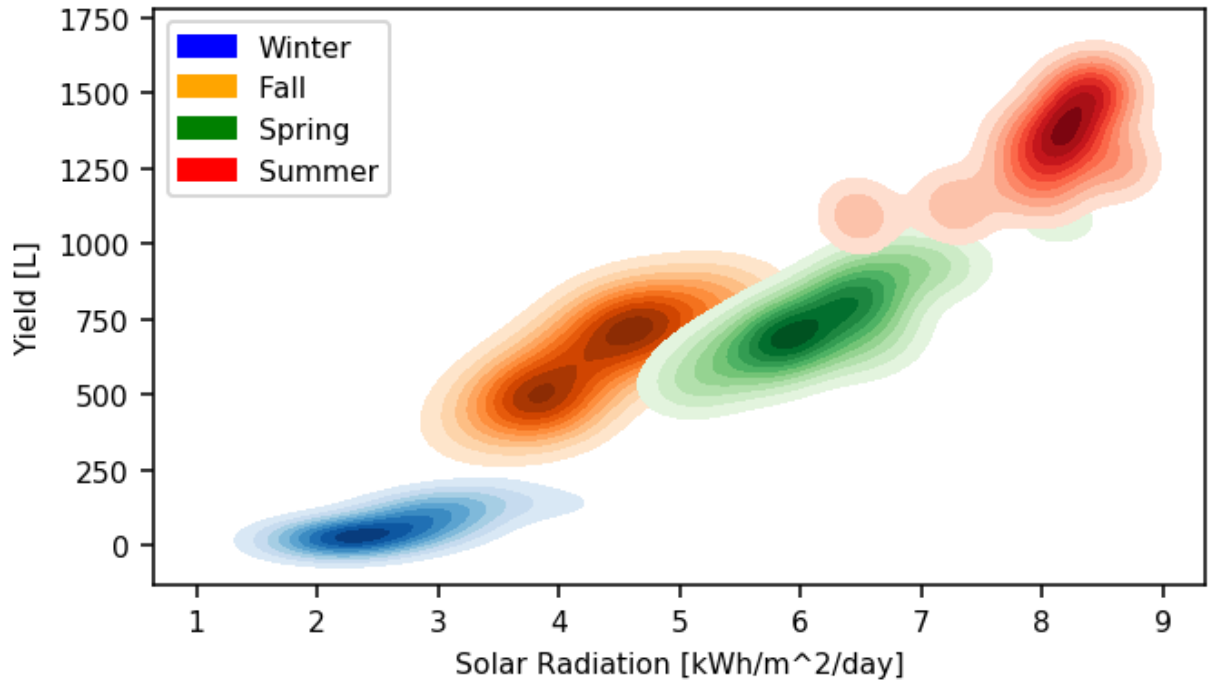


Figure 4.31: Density plot for DHW yield measurements considering fixed ambient temperatures (C) throughout the year.

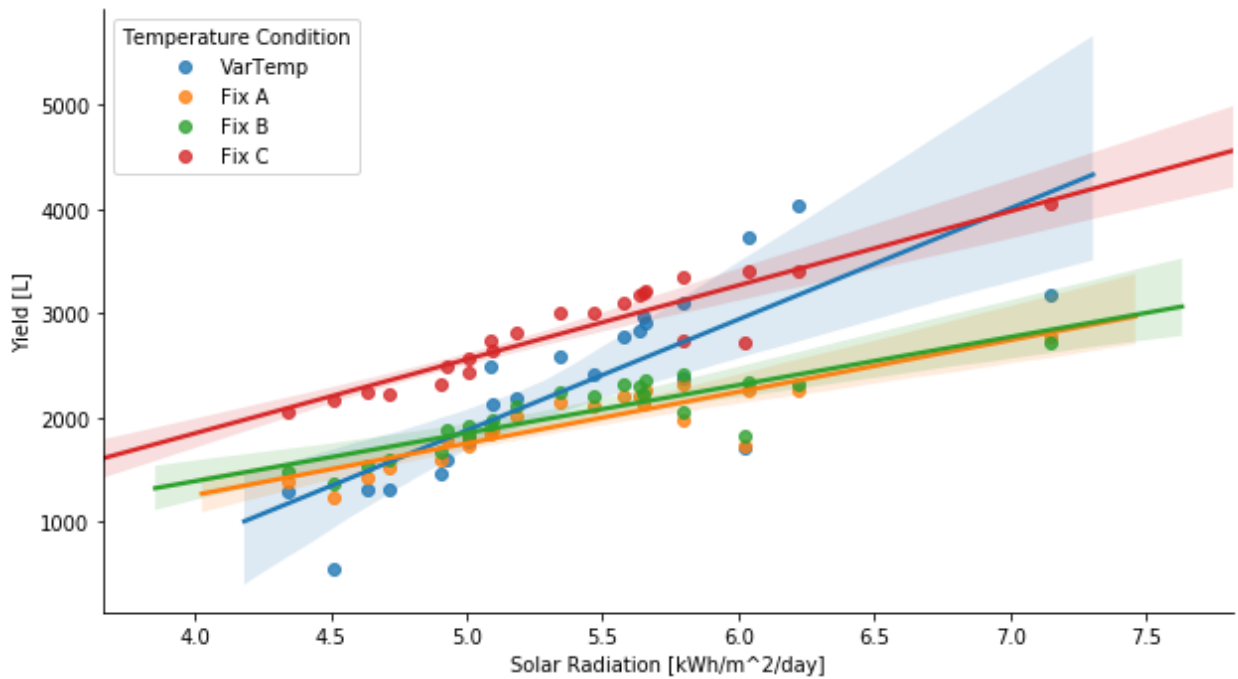


Figure 4.32: Scatter plots for yearly average daily solar radiation and accumulated DHW yield, with linear regression curves.

Table 4.7: Linear Regression parameters for accumulated DHW yield scatter plot.

Ambient Temperature Condition	m	n	$R^2$
Variable	1060.10	-3612.00	0.4844
Fixed A	495.701	-729.028	0.7691
Fixed B	461.968	-461.101	0.7279
Fixed C	711.148	-998.376	0.8504

due to ambient temperatures variations throughout the day, as for the FAT (A,B and C) conditions, the device DHW yield have much more reduced range of values for the same radiation levels, among different locations. With no temperature variations at all throughout the day, the device has a more predictable DWH yield and, therefore, a more accurate correlation between meteorological data and the device DHW yield. Also, for higher ambient temperatures throughout the year (FAT C), the amount of DHW generated is greater than for lower ambient temperature conditions (FAT A and B), even in Winter. Therefore enable the generation of DHW during Winter, the ambient temperature has to be at least 18 [°C] and is recommendable to have the device exposed the the highest ambient temperature possible with the least variations throughout the day.

For FAT (A and B) conditions, the overall DHW yield of the device is lower than for VAT conditions, for locations with yearly average daily solar radiation levels over  $\approx 5$  [kWh/m<sup>2</sup>/day] (Fig. 4.32). This could be due that the average temperature the device is exposed to in FAT conditions throughout the day, while the PV system and THP are working, is lower than if it were to be installed outside (VAT conditions). On the other hand, for higher ambient temperatures throughout the year (FAT C conditions), the amount of DHW generated is greater than for VAT conditions for the majority of the simulated locations. Therefore, the linear correlation for lower FAT conditions (A or B), can be utilized as a minimum expected DHW yield estimator for the device, in locations with yearly average daily solar radiation levels over 5 [kWh/m<sup>2</sup>/day] and the linear correlation for higher FAT conditions (C) can be utilized as a maximum expected DHW yield estimator for the device.

### 4.4.3 Overall assessments

Given that the simulated device heats and stores hot water for DHW purposes, a higher hot water outlet temperature would lead to a lower consumption of the resource, thus improving the amount of water it can deliver at comfortable temperatures by mixing the resource with local cold tap water. Also, the influence of ambient temperature in the performance of the device is possibly due to having a THP as a heat source. It could be expected that at higher average ambient temperatures, with the same power input from the PV system, the maximum temperatures reached inside the thermal storage tank would be greater, thus improving the performance measurement values for the device by being able to have a higher amount of energy stored and a higher yield of water at comfortable temperatures.

In the case of Winter season simulations, FAT conditions simulations shows that if the device is installed at an enclosed area with constant ambient temperatures, the performance

of this device could be hindered if ambient temperatures are low enough. On the other hand, enclosed areas generally have less pronounced temperature variations, so the device would have a more predictable DHW yield. Therefore, it could be recommended to have the device installed in an enclosed area, as long as average temperatures are at least 18 [°C].

The maximum temperatures reached inside the thermal storage tank are not high enough to prevent *legionella* growth [5]. Although, given that at these temperatures the tank is almost fully depleted from hot water for each use, under the established draw profiles, enough water is replaced to prevent bacteria accumulation. If temperatures were to be higher, the tank contents would not be replaced entirely with a single shower, but temperatures would be high enough to impair *legionella* proliferation.

It is important to notice that all the results for the simulated device are obtained considering the draw profiles and PV system mentioned in Section 3.4 and results would most probably be greatly different for any other draw profile and PV system. A higher demand for DHW could result in lower comfort levels for all the locations. Being that said, the amount of DHW the device is capable of producing is a non-negligible amount and could potentially reduce the fossil fuel consumption of its users.

# Chapter 5

## Conclusions

This thesis work has a broad range of procedures that had led to the actual results of the investigation. First of all, a fully functional test rig for water thermal storage devices, able to acquire data from water discharges, has been successfully conceived, designed, built and programmed, and is actually available for further device experimentation. The experimental results from the test rig show that the needed data to enable further analysis in this Thesis work has been acquired and stored adequately, proving that the test rig has accomplished its design purpose.

The numerical simulations for the PV system were successful and provided part of the input data for the device simulation. The overall performance of simulated PV systems can be improved by modifying the PV panels orientation, depending on the location; further analysis has to be made. Also, personal protection equipment is recommended for handling the PV panel of the system, as its cells can reach scalding temperatures during daytime hours.

A valid numerical model for the studied stratified thermal storage tank has been successfully implemented, having the same general behaviour of the experimentally studied device and achieving the same performances, except for the amount of energy accumulated. This last performance measurement, although has a 30% relative error in comparison to the experimental results, can be overlooked as it does not affect the DWH yield results for the numerical model and does not hinder the simulation for the considered locations.

A linear correlation between the device expected DHW yield and a location's meteorological condition is found for the draw profile and PV system specified in Section 3.4. For a yearly average of daily solar radiation of over 5 [kWh/m<sup>2</sup>/day], the seasonal and yearly linear regressions for fixed ambient temperature conditions can be used to determine the device minimum DHW yield, using the location daily solar radiation average values. The same can be said about the expected shower comfort of the device, a correlation for estimating a minimum value for this performance measurement is found and is valid for locations with yearly averages of daily solar radiation higher than 5 [kWh/m<sup>2</sup>/day].

The validated numerical model is greatly affected by ambient temperatures due to having a THP as a heat source. Being that said, this numerical model is able to determine

the prototype DHW yield under specified hot water draw demand profiles and a location meteorological conditions. To determine the device potential energy savings for a location, specified draw profiles and associated PV system, a simulation using the validated numerical model has to be run.

The temperatures reached inside the thermal storage tank are not high enough to prevent *legionella* growth, but water circulation is high enough to prevent bacteria accumulation. Risk of legionellosis infections are low to null.

It can be inferred that scaling up the dimensions of the device (thermal storage and THP) and the PV system can result in higher DHW yields for any location. If temperatures inside the scaled thermal storage do not reach a minimum of 60 [ $^{\circ}C$ ], an automatic purge system would need to be installed additionally to prevent *legionella* accumulation.

It is recommendable to install the device in an enclosed area for it will have a more predictable and potentially beneficial behaviour, as long as ambient temperatures are greater or equal to 18 [ $^{\circ}C$ ].

The main objective of this Thesis work is accomplished, as the yield of a Solar Domestic Hot Water Generator is determined for different meteorological conditions, a specified draw profile and associated PV system, via the validation of a numerical model and obtained linear correlations between the device DHW yield and a location meteorological conditions, more specifically the location yearly average daily solar radiation.

Regarding the device overall performance and potential benefits, this new technology is able to provide with non-negligible amounts of DHW throughout the year, benefiting the users by reducing the amount of fossil fuels utilized for DHW purposes.

Regarding the device's potential, this device is able to provide with a considerable amount of Domestic Hot Water during Summer, Fall and Spring. The utilization of the device may vary from the simulated water draw profiles, considering that they can be installed as an auxiliary source of DHW, providing the solar generated resource when available.



# Bibliography

- [1] Ministerio de Vivienda y Urbanismo, “*Encuesta de Caracterización Socio-Económica*”. Chile, 2015.
- [2] Instituto Nacional de Economía, “*VII Encuesta de Presupeusto Familiares*”. Chile, 2013
- [3] M. Roach, I. Cohen, “*Lumos: Pay-as-you-Go solar in Nigeria with MTN*”, GSMA. October, 2016
- [4] International Energy Agency, World Energy Outlook, 2015. <http://www.worldenergyoutlook.org/weo2015/>
- [5] Dennis PJ, Green D, Jones BP (1984). A note on the temperature tolerance of *Legionella*. *Journal of Applied Bacteriology*, 56:349–350.
- [6] V. Badescu, “*Verification of some very simple clear and cloudy sky models to evaluate global solar irradiance*”, *Solar Energy*, vol. 61, pp. 251-264, Oct 1997.
- [7] T. Stoffel, D. Renne, D. Myers, S. Wilcox, M. Sengupta, R. George, and C. Turchi, “*Concentrating Solar Power: Best Practices Handbook for the Collection and Use of Solar Resource Data (CSP)*”, NREL/TP-550-47465, 2010.
- [8] R. G. Allen, Environmental, and E. Water Resources institute . Task Committee on Standardization of Reference, “*The ASCE standardized reference evapotranspiration equation*”. Reston, Va.: American Society of Civil Engineers, 2005.
- [9] J. W. Spencer, “Fourier series representation of the sun,” *Search*, vol. 2, p. 172, 1971.
- [10] NREL. (February 2000). *SOLPOS: Solar Position and Intensity*. Available: <http://rredc.nrel.gov/solar/codesandalgorithms/solpos/>
- [11] NREL. (February 2000). *SOLPOS Online Calculator*. Available:<http://www.nrel.gov/midc/solpos/solpos.html>

- [12] I. Reda and A. Andreas. (2003). “*Solar Position Algorithm for Solar Radiation Applications*”. NREL Report No. TP-560-34302. <http://www.nrel.gov/docs/fy08osti/34302.pdf>
- [13] I. Reda and A. Andreas, “*Solar position algorithm for solar radiation applications*”, Solar Energy, vol. 76, pp. 577-589, 2004.
- [14] Perez, R., Ineichen, P., Seals, R., Michalsky, J., Stewart, R., 1990. “*Modeling daylight availability and irradiance components from direct and global irradiance*”. Solar Energy 44 (5), 271-289.
- [15] Loutzenhiser P.G. et. al. “*Empirical validation of models to compute solar irradiance on inclined surfaces for building energy simulation*” 2007, Solar Energy vol. 81. pp. 254-267.
- [16] ASTM E 1036, “*Testing Electrical Performance of Non-concentrator Photovoltaic Modules and Arrays Using Reference Cells*”, American Society of Testing and Materials.
- [17] R. Downs, et al, “*PVUSA Procurement, Acceptance, and Rating Practices for Photovoltaic Power Plants*”, Pacific Gas and Electric Company R&D Report #95-30910000.1, Sept. 1995.
- [18] William F. Holmgren, Clifford W. Hansen, Mark A. Mikofski. “*pvlib python: a python package for modeling solar energy systems.*” Journal of Open Source Software, 3(29), 884, (2018).
- [19] B. Marion, M. Anderberg, R. George, P. Gray-Hann, D. Heimiller. “*PVWATTS Version 2 - Enhances spatial resolution for calculation grid-connected PV performance*”. National renewable Energy Laboratory. Oct. 2001
- [20] D. King, J. Kratochvil, and W. Boyson, “*Measuring Solar Spectral and Angle-of-Incidence Effects on PV Modules and Solar Irradiance Sensors*”, 26th IEEE PV Specialists Conference, 1997, pp. 1113-1116.
- [21] A. H. Fanney, et al., “*Short-Term Characterization of Building Integrated Photovoltaic Modules*”, Proceedings of Solar Forum 2002, Reno, NV, June 15-19, 2002.
- [22] D. King, W. Boyson, and J. Kratochvil, “*Analysis of Factors Influencing the Annual Energy Production of Photovoltaic Systems*”, 29th IEEE PV Specialists Conference, 2002.
- [23] Thomson, W. “*On a mechanical theory of thermo-electric currents*”. Proceedings of the Royal Society of Edinburgh. (1851), 3 (42): 91–98.
- [24] Seebeck, J. “*Magnetische Polarisation der Metalle und Erze durch Temperatur-Differenz*” [Magnetic polarization of metals and ores by tem-

- perature differences]. Abhandlungen der Königlichen Akademie der Wissenschaften zu Berlin (in German):(1822) 265–373.
- [25] Peltier, J.C. “*Nouvelles expériences sur la calorificité des courants électrique*” [New experiments on the heat effects of electric currents]. *Annales de Chimie et de Physique* (in French). (1834) 56: 371–386.
- [26] Jekel, C.F., Venter, G., Venter, M.P. et al, “*Similarity measures for identifying material parameters from hysteresis loops using inverse analysis*”. *International Journal of Material Forming* (2019) 12: 355.
- [27] Luo, Q., Tang, G., Liu, Z., Wang, J. “*A novel water heater integrating thermoelectric heat pump with separating thermosiphon*”. *Applied Thermal Engineering* (2005) 25: 2193-2203.
- [28] Cai, Y., Zhang, D., Liu, D., Zhao, F., Wang, H. “*Air Source Thermoelectric Heat Pump for Simultaneous Cold Air Delivery and Hot Water Supply: Full Modeling and Performance Evaluation*”, *Renewable Energy* (2018)
- [29] Shen, L., Pu, X., Sun, Y., Chen, J. “*A study on thermoelectric technology application in net zero energy buildings*”. *Energy* (2016) 113: 9–24.
- [30] Head K., Clarke M., Bailey M., Livinski A., et al. Report of the systematic review on the effect of indoor heat on health, WHO Housing and Health Guidelines.